# Dirac materials and the response to elastic lattice deformation

by

Tianyu Liu

M.Sc., The University of British Columbia, 2015
B.Sc., University of Science and Technology of China, 2013

A THESIS SUBMITTED IN PARTIAL FULFILLMENT OF
THE REQUIREMENTS FOR THE DEGREE OF

DOCTOR OF PHILOSOPHY

in

The Faculty of Graduate and Postdoctoral Studies

(Physics)

THE UNIVERSITY OF BRITISH COLUMBIA

(Vancouver)

July 2019

The following individuals certify that they have read, and recommend to the Faculty of Graduate and Postdoctoral Studies for acceptance, a dissertation entitled:

Dirac materials and the response to elastic lattice deformation

submitted by Tianyu Liu in partial fulfillment of the requirements for the degree of Doctor of Philosophy
in Physics

## Examining Committee:

Marcel Franz
Research Supervisor

Fei Zhou
Supervisory Committee Member

Joshua Folk
Supervisory Committee Member

Joanna Karczmarek
University Examiner

Roman Krems
University Examiner

## Additional Supervisory Committee Members:

Ariel Zhitnitsky
Supervisory Committee Member

# Abstract

Dirac materials have formed a thriving and prosperous direction in modern condensed matter physics. Their bulk bands can linearly attach at discrete points or along curves, leading to arc or drumhead surface states. The candidate Dirac materials are exemplified by Dirac/Weyl semimetals, Dirac/Weyl superconductors, and Dirac/Weyl magnets. Owing to the relativistic band structure, these materials have unique responses to the applied elastic crystalline lattice deformation, which can induce pseudo-magnetic and pseudo-electric fields near the band crossings and produce transport distinguished from that caused by ordinary magnetic and electric fields. In this dissertation, I will demonstrate the exotic transport due to the strain-induced gauge field in Weyl semimetals, Weyl superconductors, and Weyl ferromagnets. I will first elucidate that a simple bend deformation can induce a pseudo-magnetic field that can give rise to the Shubnikov-de Haas oscillation in Weyl semimetals. Then I will elaborate that strain can Landau quantize charge neutral Bogoliubov quasiparticles as well and result in thermal conductivity quantum oscillation in Weyl superconductors. Lastly, I will consider the strain-induced gauge field beyond the fermionic paradigm and explain various quantum anomalies of magnons in Weyl ferromagnets.

# Lay Summary

The first decades of $20^{\text{th}}$ century have witnessed the birth of quantum mechanics, while the first decades of $21^{\text{st}}$ century see its great impacts to our life through a variety of quantum materials. A deep understanding on the physics of quantum materials will undoubtedly help us make better use of them to benefit our life. Motivated by this goal, this dissertation systematically investigates a special type of quantum materials – Dirac materials – with particular attention paid to their response to elastic deformation. By analytical derivation and numerical simulation, I elucidate that the response of Dirac materials to static and dynamic elastic deformation highly mimics that to electromagnetic fields. The currents driven by electromagnetic fields can then be alternatively created by properly deforming Dirac materials. This unique feature makes Dirac materials stand out from other quantum materials and renders Dirac materials useful for the future application in quantum technologies.

# Preface

This dissertation summarizes several projects I did during my doctorate, focusing on the transport properties of Dirac materials in the presence of strain-induced gauge field. I am responsible for most of the analytical derivations and numerical simulations under supervision of Prof. Marcel Franz and in consultation with Prof. Satoshi Fujimoto – my supervisor during my visit to Osaka University. Dr. Dmitry Pikulin and Dr. Zheng Shi also share some workload with me. The contribution of each researcher is detailed as below.

- Chapter 2 and Appendix A are published in the paper Physical Review B **95**, 041201(R) (2017), coauthored by Tianyu Liu, Dmitry Pikulin, and Marcel Franz. The initial idea of the project is brought up by Prof. Franz. I am in charge of all numerical simulation presented in Figs. 2.3-2.6 and Fig. A.1 and a portion of analytical calculation. Prof. Franz plotted Figs. 2.1-2.3, 2.5. Dr. Pikulin plotted Fig. 2.6(b). The other figures are plotted by me and further edited by Dr. Pikulin. Some text in Chapter 2 and Appendix A is directly adapted from the paper, where Prof. Franz and Dr. Pikulin share the credit for preparing the manuscript.

- Chapter 3 and Appendix B are published in the paper Physical Review B **96**, 224518 (2017), coauthored by Tianyu Liu, Marcel Franz, and Satoshi Fujimoto. The initial idea is formulated by myself in consultation with Prof. Franz and Prof. Fujimoto. I did all the analytical and numerical calculations presented in Chapter 3 and Appendix B. Some text in Chapter 3 and Appendix B is directly adapted from the paper, where Prof. Franz, Prof. Fujimoto, and I contributed equally to the preparation of the manuscript.

- Chapter 4 and Appendices C – E are published Physical Review B **99**, 214413 (2019), coauthored by Tianyu Liu and Zheng Shi. The initial idea of the project is formulated by myself in consultation with Prof. Franz. I did all of the analytical and numerical calculations presented in Chapter 4 and Appendices C – E except for Figs. 4.8 and D.2, which

are produced by Dr. Shi. Some text in Chapter 4 and Appendices C – E is directly adapted from the manuscript, which is prepared by Dr. Shi and myself. Prof. Franz has read the paper and made some minor changes.

The reuse of the three published papers is approved by the American Physical Society (APS) under Licenses **RNP/19/JUN/015910-015912**.

# Table of Contents

# List of Tables

# List of Figures

# List of Abbreviations

| | |
|---|---|
| AFM | Atomic force microscope |
| DSC | Dirac superconductor |
| DSM | Dirac semimetal |
| NI | Normal insulator |
| QO | Quantum oscillation |
| SC | Superconductor |
| SdH | Shubnikov - de Haas |
| STM | Scanning tunneling microsocpe |
| TI | Topological insulator |
| WSC | Weyl superconductor |
| WSM | Weyl semimetal |

# Acknowledgements

During my program in UBC, many people offered me help on my academic and daily life. It may not be possible for me to thank them one by one here. But their help will be appreciated and cherished forever.

My heartfelt gratefulness first goes to my supervisor Prof. Marcel Franz, who is an exceptional and considerate supervisor, supporting me both academically and financially throughout my graduate education and research career. Prof. Franz offers me maximal flexibility and always encourages me to pursue projects I am interested in and to conduct research independently but always provides timely help. He puts my personal development on high priority and always recommends me useful workshops and conferences but always allows me to attend those I find interesting myself. His deep insights, extensive knowledge, and outstanding professionalism greatly influence me as a physicist more than anyone else. I feel honorable and fortunate to work with him during my early research career.

Secondly, I would like to thank my supervisory committee – Prof. Fei Zhou, Prof. Ariel Zhitnitsky, and Prof. Joshua Folk. They help me to understand the physics in my dissertation from various points of view. Prof. Zhou helps me clarify the physics in magnon systems. Prof. Zhitnisky facilitates my understanding in the strain-induced gauge field. Prof. Folk guides me in experimental implementation of some of my proposals on observing pseudo-electromagnetic transport. Their challenging questions push me to think harder and deeper. Without them, the dissertation would never be as consolidate as it is now.

A part of my research was done during my visit to Osaka University where I held a funding awarded by "Junior Research Program (JREP)" under Topo-Q network offered by the "Topological Materials Science (TMS)" project. I owe particular thanks to Prof. Yoshiteru Maeno (Kyoto University) who brings about this opportunity and guides me through the application. I am also very grateful to Prof. Norio Kawakami (Kyoto University) – the TMS project leader for the financial supports during my time in Japan. My particular gratefulness goes to Prof. Satoshi Fujimoto, my supervisor in Osaka University. His rigorous scholarship and extraordinary patience in

conducting research impressed and benefited me a lot.

I offer my enduring gratitude to my collaborators – Dr. Dmitry Pikulin (Microsoft Station Q) and Dr. Zheng Shi (Freie Universität Berlin) for their prominent contribution to the work presented in Chapter. 2 and Chapter. 4, respectively. I am indebted to Dr. Ying Su (Hong Kong University of Science and Technology), Prof. Tobias Meng (Technische Universität Dresden), Prof. Atsushi Tsuruta (Osaka University), Prof. Takeshi Mizushima (Osaka University), Taiki Matsushita (Osaka University), Prof. Masatoshi Sato (Kyoto University), Prof. Danshita Ippei (Kyoto University), Prof. Yong Baek Kim (University of Toronto), Prof. Akira Furusaki (RIKEN) and my fellow graduate students in UBC and Osaka University for their insightful and illuminating discussions.

My special gratefulness and appreciation goes to Prof. Philip C. E. Stamp who is an awesome mentor and friend to me. I have greatly benefited from his extensive knowledge in quantum field theory and perhaps learned even more from his attitude towards life, which influences me profoundly and helps shape my character.

Lastly, I would like to thank my family. My parents offered me unconditional love and support throughout my doctorate. Their encouragement help me come through the most difficult and depressed times during the program. I am also thankful to my wife Margaret for her consistent care and her optimistic attitude that always cheers me up.

*To My Family*

# Chapter 1

# Introduction

In 1928, Paul Dirac invented the celebrated 4-component spinor (bispinor) wave equation named after him [1], making an important contribution to the reconciliation of special relativity and quantum mechanics[1], 23 years after Albert Einstein's *Annus mirabilis* paper [3] and 2 years after Erwin Schrödinger's milestone equation [4]. The most important consequence of Dirac equation is the prediction of the existence of anti-matter, which is later justified by the discovery of positron [5] – the antiparticle of electron. In the relativistic limit, the elementary fermionic particles (quarks and leptons) and their antiparticles obey Dirac equation, constituting the so-called "Dirac fermions."

Shortly after Dirac's groundbreaking work, German mathematician Hermann Weyl proposed a way that decouples Dirac equation into a pair of wave equations for 2-component spinors[2], provided that the mass term in Dirac equation is vanishing [7]. The 2-component spinor wave function represents a massless relativistic fermion with definite chirality (handedness). This fermion is referred to as the "Weyl fermion." Since Wolfgang Pauli's famous letter addressed to "Dear radioactive ladies and gentlemen" [8], neutrinos are once thought of as Weyl fermions [9–11]. However, the discovery of neutrinos in 1956 [12] prompts the examination of the consequence of small but nonzero neutrino mass. Now, through the oscillation experiment [13, 14], we know that a neutrino does have mass and cannot be a Weyl fermion.

The complexity of generating relativistic Dirac fermions in accelerators and the hopeless search of elementary particles as Weyl fermions cast shadow on experimental studies of the interplay between Dirac/Weyl fermions and gauge fields (e.g., the electromagnetic field) in the context of particle physics.

[1] Another contribution worthy to be mentioned is the Klein-Gordon equation, in which the probability density unfortunately cannot be well defined due to the lack of positive definiteness [2]. But this drawback motivates the search for new relativistic quantum theories and eventually paves the way to Dirac equation.

[2] The other way of decoupling Dirac equation is proposed by Ettore Majorana in 1937 [6]. In Majorana's representation, the 2-component spinor wave function characterizes a chargeless fermion that is its own antiparticle. This fermion is referred to as the "Majorana fermion."

Fortunately, such difficulty can be overcome in the context of condensed matter physics, where physics is encoded by the collective behavior of all the particles comprising a condensed matter system. The collective behavior itself is characterized by a quasiparticle, which is the quantum mechanical superposition of all the component particles. Although the component particles are generally massive, the resulting quasiparticles established from them can have zero effective mass, thus mimic the massless relativistic Dirac and Weyl fermions.

In the context of condensed matter physics, the materials that host quasiparticles obeying Dirac and Weyl equations constitute the so-called "Dirac matter," characterized by linear energy band crossings in the bulk. It is exemplified by graphene [15, 16], Dirac/Weyl semimetals [17] and superconductors [18, 19], Weyl ferromagnets and anti-ferromagnets [20–27], and various photonic [28–31]/acoustic [32]/mechanical [33] meta-materials[3]. The easiness of being obtained and the convenience of being manipulated make Dirac matter ideal experimental venue to investigate the relativistic theories of Dirac and Weyl fermions, especially their interplay with gauge fields. Remarkably, the advantage of studying Dirac and Weyl physics with Dirac matter over elementary particles is that the Dirac/Weyl quasiparticles can exhibit either fermionic or bosonic statistics, which extends the scope of the original Dirac/Weyl theory.

My dissertation is devoted to study Dirac and Weyl quasiparticles in Dirac matter from a theoretical point of view, paying close attention to their interplay with a specific type of gauge field that is induced by elastic strain. And the present chapter aims at briefly reviewing the research accomplishments and progress on gauge fields in Dirac matter. In Section 1.1, we briefly introduce several Dirac materials. In Section 1.2, we derive the common spectra of Dirac-Landau levels of Dirac materials in the presence of gauge fields incorporated through the minimal substitution. In Section 1.3, we demonstrate that elastic strain can induce a gauge field incorporated to graphene through the minimal substitution, thus resulting in Landau quantization. In Section 1.4, we post our central motivation – extending the idea of strain-induced elastic gauge field beyond graphene to other Dirac materials.

[3]Though the quasiparticles constituting Dirac matter are quite diversified (electrons, Bogoliubov quasiparticles, magnons, photons, phonons, etc.), the Majorana particle may not be a legitimate candidate for Dirac matter. This is because the Majorana particles in topological superconductors are either confined to boundaries or vortices [34]. The resulting in-gap Majorana bands characterize bound states rather than bulk states. In fact, the bulk physics of topological superconductors are characterized by gapped Bogoliubov quasiparticle bands, which do not encode Dirac physics.

This will be elaborated gradually in Chapter 2-4 for Weyl semimetals, Weyl superconductors, and Weyl ferromagnets, respectively.

## 1.1 Dirac materials

### 1.1.1 Graphene

The simplest and best understood Dirac material is the single layer graphite – graphene [15, 16]. Though graphene has be theorized for decades, it is first successfully exfoliated from graphite in 2004 [35], 440 years after the invention of the graphite pencil. Graphene has many unusual properties, such as large thermal conductivity, low electric resistivity, and ultra high electron mobility, making it valuable for the future application as electronic devices.

The unusual properties of graphene reflect its Dirac nature. Graphene is composed of carbon atoms connected with 3 nearest neighbors (Fig. 1.1(a)) through $\sigma$ bonds formed by the "head to head" overlap of the $sp^2$ hybridized orbitals (Fig. 1.1(b)). The 3 $\sigma$ bonds of a carbon atom are identical; thus are mutually 120° apart, resulting in a honeycomb lattice spreading in the $x$-$y$ plane. The $2p_z$ orbitals perpendicular to the honeycomb sheet (Fig. 1.1(c)) do not engage in hybridization. Their "side by side" overlap leads to $\pi$ bonds connecting a carbon atom with its neighbors (nearest, second nearest, etc.). Since a carbon atom has 4 valence electrons and 3 of them are $\sigma$ electrons occupying the $sp^2$ hybridized orbitals, the $2p_z$ orbital is thus half filled. It is this $\pi$ electron on the $2p_z$ orbital that can hop to the neighboring sites, giving rise to energy bands. The conduction band and valence touches linearly at corners of the hexagonal Brillouin zone, producing massless quasiparticles. The linearity is measured by Fermi velocity $v_F \approx 10^6$m/s [36]. Consequently, the fast drifting massless quasiparticles highly emulate Dirac fermions.

The discovery of graphene has profound impacts on the subsequent research on Dirac materials. The Dirac/Weyl semimetals can be viewed as 3D graphene. The superconducting and bosonic Dirac materials are the generalized Dirac/Weyl semimetals whose component particles are replaced by Bogoliubov quasiparticles and various bosonic excitations.

### 1.1.2 Dirac and Weyl semimetals

Dirac and Weyl semimetals [17, 37–39] can be understood as 3 dimensional generalization of graphene, because they both exhibit linearly dispersing cone structure formed by energy band crossing as illustrated schematically

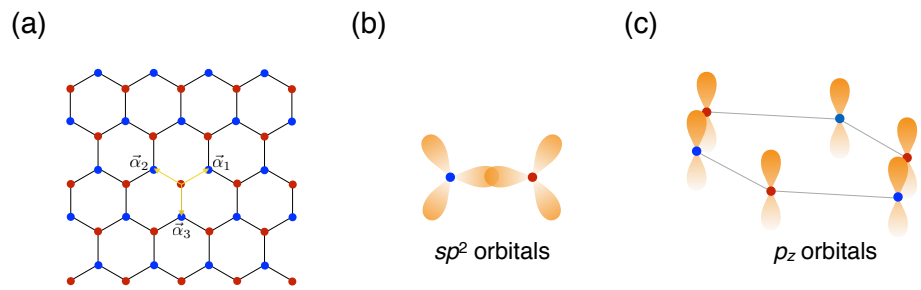


Figure 1.1: Graphene lattice and chemical bonds. (a) Graphene is a single layer of carbon atoms arranged on a honeycomb lattice. (b) Each carbon atom is connected with 3 adjacent carbon atoms by the $\sigma$ bonds due to the head-to-head overlap of the $sp^2$ hybridized orbitals. (c) The electrons on each lattice site can hop to neighboring sites along the $\pi$ bonds due to the side-by-side overlap of the unhybridized $2p_z$ orbitals.

in Fig. 1.2. One major difference between the two types of semimetals is the degeneracy of band crossings. A Dirac semimetal exhibits four-fold band crossing referred to as the Dirac point (Fig. 1.2(a)), while a Weyl semimetal possesses two-fold band crossing known as the Weyl point (Fig. 1.2(b)). In the view of band crossing degeneracy, a Weyl semimetal is like half a Dirac semimetal.

The difference in band crossing degeneracy may be further clarified by symmetry considerations. In the presence of inversion symmetry $\mathcal{P}$, a quantum state $|\boldsymbol{k}, \boldsymbol{s}\rangle$ of momentum $\boldsymbol{k}$ and spin $\boldsymbol{s}$ is mapped to $|-\boldsymbol{k}, \boldsymbol{s}\rangle$, while in the presence of time reversal symmetry $\mathcal{T}$, the same state is mapped to $|-\boldsymbol{k}, -\boldsymbol{s}\rangle$. Since a Dirac semimetal has both $\mathcal{P}$ and $\mathcal{T}$, the Dirac cone at momentum $\boldsymbol{k}$ has its $\mathcal{P}$ partner (of same spin) and $\mathcal{T}$ partner (of opposite spin) both located at momentum $-\boldsymbol{k}$, giving rise to a doubly degenerate band structure, which accounts for the four-fold degeneracy of Dirac points. On the other hand, a Weyl semimetal does not simultaneously have $\mathcal{P}$ and $\mathcal{T}$. The lacking of aforementioned symmetry protection lifts the two-fold degeneracy of energy bands. Therefore, the Weyl points formed from the resulting non-degenerate bands are only two-fold degenerate.

It is worth noting that $\mathcal{P}$ and $\mathcal{T}$ only determine the fold of degeneracy of the Dirac point. The robostness of Dirac points must rely on other crystalline symmetries. For example, Dirac semimetal $Cd_3As_2$ [40–45] is protected by four-fold rotational symmetry and Dirac semimetal $NaBi_3$ [46–48] is pro-

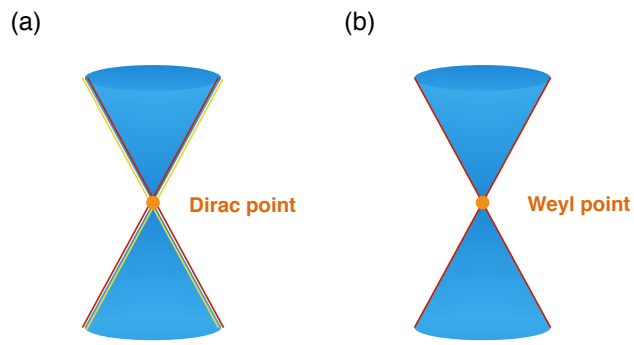


Figure 1.2: Schematic band crossings of Dirac and Weyl semimetals. (a) In Dirac semimetals, the doubly degenerate conduction and valence bands touch linearly forming cone-like band structure. The vertex of a cone represents a four-fold Dirac point. (b) In Weyl semimetals, the non-degenerate conduction and valence bands also touch linearly forming cone-like band structure. The vertex of a cone represents a two-fold Weyl point.

tected by three-fold rotational symmetry. Besides these two intrinsic Dirac semimetals, more candidate materials can be obtained by fine tuning the parameters of topological insulators to induce phase transition towards trivial insulators or vice versa. This physics has been examined in $Bi_{2-x}In_xSe_3$ [49, 50], which is a Dirac semimetal existing intermediately between topological insulator $Bi_2Se_3$ and trivial insulator $In_2Se_3$.

Weyl semimetals have been proposed and observed in $\mathcal{P}$ breaking systems such as the TaAs family of materials [51–53] and $\mathcal{T}$ breaking systems (all-in-all-out pyrochlore iridates [37], $HgCr_2Se_4$ [54], TI-NI multilayer [38]). The two types of Weyl semimetals may be differentiated by examining the number of Weyl points. For a Weyl semimetal with inversion symmetry $\mathcal{P}$ broken, the time reversal symmetry $\mathcal{T}$ requires a Weyl cone at $\boldsymbol{k}$ with chirality $\chi$ to be paired with another Weyl cone at $-\boldsymbol{k}$ with same chirality $\chi$. But the no-go theorem [55] requires the total chirality to be vanishing, indicating that there must be two more Weyl cones of chirality $-\chi$ located at $\pm\boldsymbol{k}'$. Therefore, $\mathcal{P}$ breaking Weyl semimetals must have at least four Weyl cones. On the other hand, for a Weyl semimetal with time reversal symmetry $\mathcal{T}$ broken, the inversion symmetry $\mathcal{P}$ requires a Weyl cone at $\boldsymbol{k}$ with chirality $\chi$ to be paired with another Weyl cone at $-\boldsymbol{k}$ with chirality $-\chi$, satisfying the no-go theorem automatically. Therefore, $\mathcal{T}$ breaking Weyl semimetals can have just two Weyl cones.

The band crossings in Weyl semimetals rely on the translational symmetry under which the Weyl cone chirality can be well defined. The Weyl points are protected topologically by their chirality [17], which works as either the source or the drain of Berry flux (Fig. 1.3(a)). Any 2D subsystem between the Weyl points encloses a nontrivial Berry flux thus resembles a Chern insulator. The edge states of all the 2D subsystems constitute the surface state of the Weyl semimetal (Fig. 1.3(b)). When tuning the Fermi energy $E_F$ to the Weyl points, the surface state traverses the $E_F$ iso-energy surface, leaving an arc state connecting the Weyl points, as illustrated in Fig. 1.3(b). The discrete "Fermi arc" surface state is a fingerprint of Weyl semimetals.

Dirac and Weyl semimetals exhibit many exotic properties due to their unusual electronic structure. These include the chiral anomaly [56–58], the chiral magnetic effect[4] [62, 63, 65–67], the anomaly-induced negative magnetoresistance [51, 63, 65, 66, 68–70], Majorana flat bands [71], and Fermi arc quantum oscillations [72, 73]. These properties may make Dirac and Weyl semimetals valuable in the future application to novel electronic devices.

### 1.1.3 Dirac and Weyl superconductors

Dirac and Weyl superconductors [18, 19] are the superconducting analogs of Dirac and Weyl semimetals. The only difference is that the Dirac and Weyl cones are formed by the touching of 3D Bogoliubov quasiparticle energy bands. Due to the similarity to Dirac and Weyl semimetals, the Dirac and Weyl superconductors inherit unusual properties from their semi-metallic counterparts, such as the arc-like Fermi surface [19].

Currently, there are about 20 nodal superconductors [74] having the potential to be Dirac and Weyl superconductors. Among those, the most

[4] A more generalized chiral magnetic effect is first derived in the context of high energy physics [59, 60], where both chiral fermions and their antiparticles are considered. In the presence of an applied magnetic field $\boldsymbol{B}$, a parallel axial current emerges $\boldsymbol{J}_5 \sim \mu\boldsymbol{B}$, provided that there is a concentration imbalance between particles and antiparticles (i.e., chemical potential $\mu \neq 0$). The interpretation of $\mu$ is subtle. In neutrino systems, particles are always left-handed (LH) while antiparticles are always right-handed (RH) [61]. Therefore $\mu$ is analogous to the chiral chemical potential $\mu_5$ in Weyl semimetals [62, 63]. In quark systems, the particles/antiparticles can be either left-handed or right-handed [64]. Then axial current can occur even within a single chiral species (RH or LH), if a nonzero chemical potential ($\mu_R \neq 0$ or $\mu_L \neq 0$) exists. And the total axial current is contributed by both quarks and antiquarks, making it slightly different from the chiral magnetic current [62, 63] in Weyl semimetals, where only electrons are responsible for the transport. For this reason, the axial current generated by the applied magnetic field and quark-antiquark imbalance is sometimes referred to as the "chiral separation effect" [64].

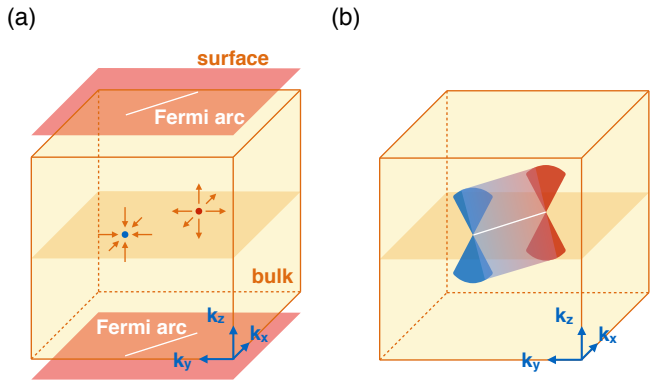


Figure 1.3: Schematic band structure plot for Weyl semimetals. (a) A pair of Weyl points in momentum space, one being the source of the Berry flux while the other acting as the drain. They are connected by Fermi arc states on the open boundaries. (b) Weyl cones and surface states in momentum space. The surface states cutting through two Weyl cones can be understood as a combination of chiral edge states of 2D subsystems between two Weyl points. When tuning Fermi energy to the Weyl points, the Fermi surface becomes an arc connecting the two Weyl points.

promising candidate materials may be $Cu_xBi_2Se_3$ [19, 75] and $Nb_xBi_2Se_3$ [76]. Recent nuclear magnetic resonance experiments [77] and specific heat experiments [78] suggest $Cu_xBi_2Se_3$ to be a Dirac superconductor. However, symmetry and energetic considerations [79, 80] suggest $Cu_xBi_2Se_3$ to have a small but non-vanishing gap. According to Ref. [76], the low temperature penetration depth of $Nb_xBi_2Se_3$ exhibits quadratic temperature dependence, which is a characteristic feature of linearly dispersing point nodes in three dimensions. This is consistent with $Nb_xBi_2Se_3$ being a Weyl superconductor.

### 1.1.4 Weyl magnets

Weyl magnets are a special type of spin crystals existing in various ferromagnetic and antiferromagnetic ordered systems such as pyrochlore magnets [20–23], double perovskites [24], and multilayer magnets [25–27]. They exhibit energy bands touching linearly at discrete points in the momentum-energy space, akin to Weyl semimetals. However, unlike the Weyl semimetals whose energy bands result from Bloch waves, the energy bands of Weyl magnets associate with spin waves [81], whose quantum is a magnon [82].

A magnon is a bosonic quasiparticle carrying spin, dipole moment, and heat. Though charge neutral, it can be controlled by either an electric field or a magnetic field through the Aharonov-Casher effect [83] or the Zeeman effect. Therefore, magnons can mimic electrons in many ways, enabling Weyl magnets to reproduce many properties of Weyl semimetals, such as the chiral anomaly [20, 25], the spin Hall effect [26], and the thermal Hall effect [84]. Superior over Weyl semimetals, Weyl magnets carry magnon currents, which are inherently free of energy dissipation due to Ohmic losses. This advantage may make Weyl magnets potentially useful to process and transport information.

### 1.1.5 Other Dirac materials

In Section 1.1.4, we have seen that substituting the spin wave for the Bloch wave produces a new Dirac material – Weyl magnets. Such generalization from Weyl semimetals to Weyl magnets reveals a standard way of searching for new Dirac materials – finding other substitutes for the Bloch wave. The first example is the electromagnetic wave carried by photonic meta-materials. By fine tuning the permittivity and the permeability of photonic meta-materials, the energy bands can touch linearly, resulting in "photonic Dirac semimetals" [28] and "photonic Weyl semimetals" [29–31]. Another example is the sound wave harbored by acoustic meta-materials. According to Ref. [32], a multilayer acoustic crystal composed of precisely designed hollow hexagonal unit cells can exhibit Weyl type energy band crossing for audible sound waves. Moreover, even the classical mechanical wave in coupled mechanical oscillators can produce linearly crossed energy bands, giving a so-called "mechanical graphene" [33].

## 1.2 Dirac-Landau levels

In Section 1.1, we have seen various Dirac materials comprised of fermionic and bosonic particles. In this section, we will quantitatively understand their physics in the framework of band theory. We will pay particular attention to the band structure of such materials in the presence of gauge fields.

The physics of Dirac materials is encoded in the Dirac Hamiltonians. The simplest Dirac Hamiltonian is

$$H = v_x p_x \sigma^x + v_y p_y \sigma^y + v_z p_z \sigma^z, \tag{1.1}$$

which is a $2 \times 2$ matrix defined on a Hilbert space spanned by some degrees

of freedom. $v_i$ and $\sigma^i$ are the $i$-th component of velocity vector[5] and Pauli matrices. For example, graphene has $v_z = 0$ and is defined on the Hilbert space spanned by sublattice degrees of freedom. More generically, Dirac Hamiltonian is $4 \times 4$ due to other degrees of freedom. Explicitly, it reads

$$H = v_x p_x \alpha^x + v_y p_y \alpha^y + v_z p_z \alpha^z + m\beta, \tag{1.2}$$

where $\boldsymbol{\alpha}$ and $\beta$ are $4 \times 4$ Dirac matrices and $m$ is the mass of the particle. Hamiltonian Eq. 1.2 applies to Dirac semimetal $Cd_3As_2$ defined on spin-orbit basis [85]. For simplicity, we will only consider Dirac materials characterized by Eq. 1.1, whose eigenvalue

$$E(\boldsymbol{p}) = \pm\sqrt{v_x^2 p_x^2 + v_y^2 p_y^2 + v_z^2 p_z^2}, \tag{1.3}$$

exhibits linearly dispersing Dirac cone structure in the momenta-energy space. When a gauge field $\mathcal{A}$ is applied to Dirac materials, the translational invariance in certain direction will generally be broken, which can gap out the Dirac cone Eq. 1.3. In the rest of this section, we will discuss the band structure of Dirac Hamiltonian Eq. 1.1 in the presence of gauge fields.

We consider a gauge field $\mathcal{A}$ that can be incorporated into Eq. 1.1 through the standard Peierls substitution $\boldsymbol{p} \to \boldsymbol{p} - q\mathcal{A}$. In electronic systems, $\mathcal{A}$ is the magnetic vector potential due to the Aharonov-Bohm effect [86]. In magnonic systems, $\mathcal{A} \sim \boldsymbol{E} \times \boldsymbol{\mu}$ with $\boldsymbol{E}$ being the external electric field applied to magnons of moment $\boldsymbol{\mu}$ due to the Aharonov-Casher effect [83]. Without loss of generality, we choose $\mathcal{A} = (-\Omega y, 0, 0)$, whose curl $\nabla \times \mathcal{A} = \Omega\hat{z}$ is a uniform field. Under the gauge field, the Dirac Hamiltonian can be written as

$$H = v_x\Big(-i\hbar\frac{\partial}{\partial x} + q\Omega y\Big)\sigma^x + v_y\Big(-i\hbar\frac{\partial}{\partial y}\Big)\sigma^y + v_z\Big(-i\hbar\frac{\partial}{\partial z}\Big)\sigma^z. \tag{1.4}$$

[5] Generically, the momentum $p_i$ can couple to Pauli matrices $\sigma^{j\neq i}$ as well, making velocity a tensor, under which the generalized Dirac Hamiltonian reads $H = \sum_{ij} p_i v_{ij} \sigma^j$. The hermicity of the generalized Dirac Hamiltonian requires the entries of the velocity tensor to be real. This implies that the singular value decomposition of velocity tensor exists and reads $v_{ij} = \sum_{mn} L_{im} \tilde{v}_{mn} R_{nj}$, where $L_{im}$ and $R_{nj}$ are $3 \times 3$ orthogonal matrices and $\tilde{v}_{mn} = \tilde{v}_n \delta_{mn}$ is a diagonal matrix with Kronecker delta $\delta_{mn}$ being the $3 \times 3$ unity matrix. The singular value decomposition allows us to rewrite the generalized Dirac Hamiltonian as $H = \sum_{ijmn} p_i L_{im} \tilde{v}_{mn} R_{nj} \sigma^j = \sum_{mn} \tilde{p}_m \tilde{v}_{mn} \tilde{\sigma}^n = \sum_n \tilde{v}_n \tilde{p}_n \tilde{\sigma}^n$, where $\tilde{p}_m = \sum_i p_i L_{im}$ and $\tilde{\sigma}^n = \sum_j R_{nj} \sigma^j$ are orthogonally transformed momenta and Pauli matrices. Using the properties of orthogonal matrices, it is straightforward to prove that the orthogonality of momenta and the commutation/anti-commutation relations of Pauli matrices are all preserved. Therefore, the generalized Dirac Hamiltonian can always be simplified to the standard Dirac Hamiltonian Eq. 1.1 where the velocity is a vector. Without loss of generality, Dirac materials with vector velocity will be our central concern in the rest of this dissertation.

To solve for the eigenvalues of Eq. 1.4, we first find the eigenvalues of

$$H^2 = \Big( -\hbar^2 v_x^2 \frac{\partial^2}{\partial x^2} - \hbar^2 v_y^2 \frac{\partial^2}{\partial y^2} - \hbar^2 v_z^2 \frac{\partial^2}{\partial z^2} \Big) - 2i\hbar q\Omega y v_x^2 \frac{\partial}{\partial x} + q^2\Omega^2 y^2 v_x^2 - \hbar q\Omega v_x v_y \sigma^z. \quad (1.5)$$

Because $[H^2, \sigma^z] = 0$, the eigenstate wave function of $H^2$ can be written as

$$\phi_s(x, y, z) = e^{\frac{i}{\hbar}(p_x x + p_z z)} f_s(y)\chi_s, \quad (1.6)$$

where $\chi_+ = (1, 0)^T$ and $\chi_- = (0, 1)^T$ are the up/down spinor and function $f_s(y)$ satisfies

$$\hbar^2 v_y^2 \frac{\partial^2 f_s}{\partial y^2} - v_x^2 (p_x + q\Omega y)^2 f_s + (-v_z^2 p_z^2 + s\hbar q\Omega v_x v_y) f_s = E^2 f_s, \quad (1.7)$$

where $E$ is the eigenvalue of the Dirac Hamiltonian Eq. 1.4. We define a new variable $\xi$ satisfying

$$\xi^2 = \frac{v_x q\Omega}{\hbar v_y} \Big( y + \frac{p_x}{q\Omega} \Big) \mathrm{sgn}(q\Omega v_x v_y). \quad (1.8)$$

Therefore, Eq. 1.7 can be written as a differential equation with respect to $\xi$ as

$$\frac{d^2 f_s}{d\xi^2} - \xi^2 f_s + a_s f_s = 0, \quad (1.9)$$

where

$$a_s = \frac{E^2 - v_z^2 p_z^2}{\hbar |v_x v_y q\Omega|} + s \cdot \mathrm{sgn}(q\Omega v_x v_y).$$

By assuming $f_s(\xi) = e^{-\frac{1}{2}\xi^2} u_s(\xi)$, Eq. 1.9 is reduced to

$$\frac{d^2 u_s}{d\xi^2} - 2\xi u_s + (a_s - 1) u_s = 0. \quad (1.10)$$

The solution to Eq. 1.10 is Hermite polynomial $u_s = H_n(\xi)$ when the following condition is satisfied

$$a_s = \frac{E^2 - v_z^2 p_z^2}{\hbar |v_x v_y q\Omega|} + s \cdot \mathrm{sgn}(q\Omega v_x v_y) = 2n + 1 \qquad n = 0, 1, 2, \cdots. \quad (1.11)$$

Since $s = \pm 1$, we define integer $\nu$ such that

$$2\nu = 2n + 1 - s \cdot \mathrm{sgn}(q\Omega v_x v_y). \quad (1.12)$$

Therefore, the eigenvalue $E$ of the Dirac Hamiltonian Eq. 1.4 satisfies

$$E^2 = v_z^2 p_z^2 + 2\nu\hbar|q\Omega v_x v_y|. \tag{1.13}$$

According to Eq. 1.12, when $s \cdot \mathrm{sgn}(q\Omega v_x v_y) = -1$, $\nu = 1, 2, \cdots$. But when $s \cdot \mathrm{sgn}(q\Omega v_x v_y) = 1$, $\nu = 0, 1, 2, \cdots$. Since there are two occasions that $\nu$ can be positive integers, the associated eigenvalues can then be determined as

$$E_\nu = \pm\sqrt{v_z^2 p_z^2 + 2\nu\hbar|q\Omega v_x v_y|} \qquad \nu = 1, 2, \cdots. \tag{1.14}$$

These are the famously known Dirac-Landau levels. It is worth to note that the dispersion of the zeroth Landau level is not $\pm v_z p_z$, because there is only one occasion ($s = \mathrm{sgn}(q\Omega v_x v_y)$) making $\nu = 0$. When $s = \mathrm{sgn}(q\Omega v_x v_y) = \pm 1$, according to Eq. 1.6, the eigenstate wave function is

$$\phi_\pm \sim e^{\frac{i}{\hbar}(p_x x + p_z z)} e^{-\frac{1}{2}\frac{v_x q\Omega}{\hbar v_y}(y + \frac{p_x}{q\Omega})^2 \mathrm{sgn}(q\Omega v_x v_y)} \chi_\pm. \tag{1.15}$$

The zeroth Landau level dispersion can be determined by using $H\phi_\pm = E_0\phi_\pm$. This leads to a chiral state

$$E_0 = \mathrm{sgn}(q\Omega v_x v_y) v_z p_z. \tag{1.16}$$

In summary, Eqs. 1.14 and 1.16 comprise the complete spectrum of Eq. 1.4. The higher ($\nu \geq 1$) Dirac-Landau levels always come in pairs with opposite energies. On the other hand, the zeroth Landau levels is chiral. In Chapters 2-4, we will see Dirac-Landau levels occur in various Dirac materials and profoundly influence the charge, heat, and spin transports in those materials.

## 1.3 Strain-induced Landau levels in Graphene

In Section 1.2, we have seen that if a gauge field is incorporated to Dirac matter by Peierls substitution, the resulting energy bands exhibit Dirac-Landau levels. We already know that the magnetic field leads to Landau quantization. In this section, following Refs. [87, 88], by using graphene as an example, we will review that properly designed elastic strain behaves like a pseudo-magnetic field that also gives rise to Landau quantization.

Our starting point is the nearest neighbor tight binding Hamiltonian on a honeycomb lattice

$$H = \sum_{\boldsymbol{r},i} t b^\dagger_{\boldsymbol{r}+\boldsymbol{\alpha}_i} a_{\boldsymbol{r}} + h.c., \tag{1.17}$$

where the $i$-th nearest neighbor is connected by $\boldsymbol{\alpha}_i$ illustrated in Fig. 1.1(a) and $t$ is the overlap integral of the $\pi$ bond connecting to the $i$-th nearest neighbor. Apply Fourier transform

$$\begin{pmatrix} a_{\boldsymbol{r}} \\ b_{\boldsymbol{r}} \end{pmatrix} = \frac{1}{\sqrt{N}} \sum_{\boldsymbol{k}} e^{i\boldsymbol{k}\cdot\boldsymbol{r}} \begin{pmatrix} a_{\boldsymbol{k}} \\ b_{\boldsymbol{k}} \end{pmatrix}, \tag{1.18}$$

where $N$ is the number of unit cells. In the sublattice basis $\Phi_{\boldsymbol{k}} = (a_{\boldsymbol{k}}, b_{\boldsymbol{k}})^T$, the tight binding Hamiltonian can be written as

$$H = \sum_{\boldsymbol{k}} \Phi^\dagger_{\boldsymbol{k}} \mathcal{H}_{\boldsymbol{k}} \Phi_{\boldsymbol{k}}, \tag{1.19}$$

where

$$\mathcal{H}_{\boldsymbol{k}} = \sum_i t\cos(\boldsymbol{k}\cdot\boldsymbol{\alpha}_i)\sigma^x - \sum_i t\sin(\boldsymbol{k}\cdot\boldsymbol{\alpha}_i)\sigma^y. \tag{1.20}$$

The first quantized Hamiltonian (Eq. 1.20) is gapless at the corners of Brillouin zone $\boldsymbol{K}_\eta = \eta(4\pi/3\sqrt{3}a, 0)$. In the vicinity of $\boldsymbol{K}_\eta$, $\mathcal{H}_{\boldsymbol{k}}$ can be expanded as

$$\mathcal{H}_{\boldsymbol{K}_\eta+\boldsymbol{q}} \approx \mathcal{H}_{\boldsymbol{K}_\eta} + \boldsymbol{q}\cdot\nabla_{\boldsymbol{k}}\mathcal{H}_{\boldsymbol{k}} = -\frac{3}{2}ta\eta q_x\sigma^x + \frac{3}{2}taq_y\sigma^y = h^\eta_{\boldsymbol{q}}, \tag{1.21}$$

which is a 2D Dirac Hamiltonian same as Eq. 1.1 if the velocity parameters in Eq. 1.1 are set as

$$(v_x, v_y, v_z) = \frac{1}{\hbar}\Big(-\frac{3}{2}ta\eta, \frac{3}{2}ta, 0\Big).$$

When the honeycomb lattice of graphene is deformed by external strain, the $2p_z$ orbital on each lattice site $\boldsymbol{R}$ will be translated to a new position $\boldsymbol{R}+\boldsymbol{u}(\boldsymbol{R})$, where $\boldsymbol{u}(\boldsymbol{R})$ is the displacement field. Then the overlap $t$ between the $2p_z$ orbital originally located at $\boldsymbol{R}$ and the adjacent $2p_z$ orbital originally located at $\boldsymbol{R}' = \boldsymbol{R} + \boldsymbol{\alpha}_i$ will be changed to

$$\begin{aligned} t(\boldsymbol{R}' + \boldsymbol{u}(\boldsymbol{R}') - \boldsymbol{R} - \boldsymbol{u}(\boldsymbol{R})) &\approx t(\boldsymbol{R}' - \boldsymbol{R}) + \nabla t\cdot(\boldsymbol{u}(\boldsymbol{R}') - \boldsymbol{u}(\boldsymbol{R})) \\ &\approx t(\boldsymbol{R}' - \boldsymbol{R}) + \nabla t\cdot(\boldsymbol{R}' - \boldsymbol{R})\cdot\nabla\boldsymbol{u}. \end{aligned} \tag{1.22}$$

We may estimate $\nabla t = -\beta t\frac{\boldsymbol{\alpha}_i}{a^2} \approx -t\frac{\boldsymbol{\alpha}_i}{a^2}$, where we have taken the Grüneisen parameter $\beta \approx 1$. Then we conclude that the overall effect of the elastic strain can be considered by doing the following overlap integral substitution

$$t \to t\Big(1 - \frac{1}{a^2}\boldsymbol{\alpha}_i\cdot\boldsymbol{\alpha}_i\cdot\nabla\boldsymbol{u}\Big). \tag{1.23}$$

It is worth noting that $\boldsymbol{\alpha}_i \cdot \boldsymbol{\alpha}_i \cdot \nabla \boldsymbol{u} = \alpha_i^\mu \alpha_i^\nu \partial_\mu u_\nu = \alpha_i^\mu \alpha_i^\nu u_{\mu\nu}$ where $u_{\mu\nu} = \frac{1}{2}(\partial_\mu u_\nu + \partial_\nu u_\mu)$ is the symmetrized strain tensor. Plug Eq. 1.23 to Eq. 1.17 and assume constant strain tensor, following the Fourier transform, we find that the first quantized Hamiltonian $\mathcal{H}_{\boldsymbol{k}}$ (Eq. 1.20) needs to be modified by an extra term

$$\begin{aligned}\delta\mathcal{H}_{\boldsymbol{k}} = &-t\Big(\frac{3}{4}u_{xx} + \frac{1}{4}u_{yy} + \frac{\sqrt{3}}{2}u_{xy}\Big)\cos(\boldsymbol{k}\cdot\boldsymbol{\alpha}_1)\sigma^x \\ &+ t\Big(\frac{3}{4}u_{xx} + \frac{1}{4}u_{yy} + \frac{\sqrt{3}}{2}u_{xy}\Big)\sin(\boldsymbol{k}\cdot\boldsymbol{\alpha}_1)\sigma^y \\ &- t\Big(\frac{3}{4}u_{xx} + \frac{1}{4}u_{yy} - \frac{\sqrt{3}}{2}u_{xy}\Big)\cos(\boldsymbol{k}\cdot\boldsymbol{\alpha}_2)\sigma^x \\ &+ t\Big(\frac{3}{4}u_{xx} + \frac{1}{4}u_{yy} - \frac{\sqrt{3}}{2}u_{xy}\Big)\sin(\boldsymbol{k}\cdot\boldsymbol{\alpha}_2)\sigma^y \\ &- tu_{yy}\cos(\boldsymbol{k}\cdot\boldsymbol{\alpha}_3)\sigma^x + tu_{yy}\sin(\boldsymbol{k}\cdot\boldsymbol{\alpha}_3)\sigma^y. \end{aligned} \tag{1.24}$$

The physics in the vicinity of $\boldsymbol{K}_\eta$ is then characterized by

$$h_{\boldsymbol{q}} + \delta\mathcal{H}_{\boldsymbol{K}_\eta} = -\frac{3}{2}ta\eta\Big(q_x + \eta\frac{u_{yy} - u_{xx}}{2a}\Big)\sigma^x + \frac{3}{2}ta\Big(q_y + \eta\frac{u_{xy}}{a}\Big)\sigma^y. \tag{1.25}$$

It is obvious to see that the strain-induced extra Hamiltonian $\delta\mathcal{H}_{\boldsymbol{k}}$ is incorporated into the 2D Dirac Hamiltonian $h_{\boldsymbol{q}}$ through Peierls substitution $\boldsymbol{q} \to \boldsymbol{q} + \frac{e}{\hbar}\mathcal{A}$, where the emergent vector potential is

$$\mathcal{A} = \frac{\eta\hbar}{2ea}(u_{yy} - u_{xx}, 2u_{xy}). \tag{1.26}$$

Though we assumed constant strain tensor $u_{\mu\nu}$ when deriving $\mathcal{A}$, we argue that even when $u_{\mu\nu}$ is spatially varying, the strain effect can be treated as an emergent vector potential expressed in Eq. 1.26, as long as it varies slowly on the lattice scale. By fine tuning the displacement field as in Ref. [87], we can get a uniform strain-induced emergent gauge field $\mathcal{B} = \nabla \times \mathcal{A}$. Therefore, according to our analysis in Section 1.2, the resulting band structure will be flat Landau levels

$$E_n = \sqrt{2n\hbar e|\mathcal{B}||v_x v_y|} = \Big|\frac{3ta}{2}\Big|\sqrt{2n\frac{e|\mathcal{B}|}{\hbar}} \qquad n = 0, 1, 2, \cdots. \tag{1.27}$$

From the point of view of band structure, the strain-induced gauge field $\mathcal{B}$ highly mimics the ordinary magnetic field. Therefore, many magnetic transport properties associated with Landau levels can be in principle reproduced

by proper strains. For this reason $\mathcal{B}$ is often referred to as a "pseudo-magnetic field." However, it is worth noting that the emergent vector potential $\mathcal{A}$ and the pseudo-magnetic field $\mathcal{B}$ only exist near Dirac points and couple to different Dirac points oppositely. Therefore, the strain-induced Landau levels only exist in the vicinity of Dirac points and are fundamentally different from the ordinary Landau levels due to an ordinary magnetic field.

## 1.4 Motivation

In Section 1.3, we have seen that strain couples to low-energy 2D Dirac fermions in graphene as an emergent $U(1)$ gauge field. And according to the analysis in Section 1.2, this strain-induced elastic gauge field leads to Landau quantization in graphene. This discovery has profound influence on the study of graphene, because it is the first instance that the presence of Landau levels does not depend on applying magnetic fields.

Since the proposal [87] and experimental implementation [89] of strain-induced Landau levels in graphene, the idea of strain-induced gauge fields and Landau quantization has be broadened to other systems such as "photonic graphene" [90] and "magnonic graphene" [91]. Since there are lots of other members in the family of Dirac matter, we hypothesize that strain will also produce Landau quantization to these materials and can affect their individual transport drastically. Motivated to justify this hypothesis, the present dissertation is organized as follows.

In Chapter 2, we show that a circular bend lattice deformation gives rise to Dirac-Landau levels in Weyl semimetal thin films. Though there have been several proposals of generating Landau levels in Weyl semimetals with strain [92–97], their experimental implementation and transport measurement are not as feasible as ours. Due to the simplicity of the strain design, our induced elastic gauge field can be tuned continuously, allowing us to perform dynamic measurement of quantum oscillations, which are difficult to measure in other existing proposals. In the chapter, we demonstrate that the scanning strain-induced pseudo-magnetic field results in Shubnikov-de Haas (SdH) oscillation. This is the first instance that quantum oscillations occur without applying magnetic field.

In Chapter 3, we show that the same bend deformation can also Landau quantize linearly dispersing Bogoliubov quasiparticles in Weyl superconductors. This sheds new light on observing Landau quantization based transport in the presence of superconductivity. Particularly, the strain-induced Landau levels allow superconducting regime quantum oscillations. On the other

hand, QOs have only been previously observed in normal [98–103] and vortex state [104–106] superconductors. We elucidate that the strain-induced Landau levels give rise to quasiparticle Wiedemann-Franz law and thermal conductivity quantum oscillations when the strain-induced gauge field is continuously tuned.

In Chapter 4, we show that a twist deformation can Landau quantize relativistic magnons in Weyl ferromagnets. It thus resembles an inhomogeneous electric field. We further show that a time-dependent uniaxial deformation can drive magnons along the energy bands. Therefore, such deformation is analogous to an inhomogeneous magnetic field. The combination of the strain-induced elastic gauge field and the electromagnetic field produces various magnon quantum anomalies in Weyl ferromagnets. These anomalies are characterized by the non-conservation of chirality or bulk thermal energy. The anomalous spin and heat transport due to these anomalies is also derived. Its unique field dependence may play a key role in detecting magnon quantum anomalies experimentally.

Chapter 5 concludes the whole dissertation, envisages a few worthwhile directions on the thermal transport in the presence of strain-induced gauge fields, and discusses the possibility of reproducing Landau quantization in other Dirac materials.

# Chapter 2

# Zero-field quantum oscillations in Weyl semimetals

Dirac and Weyl semimetals [17, 37–39] are known to exhibit a variety of exotic behaviors owing to their unusual electronic structure comprised of linearly dispersing electron bands at low energies. These include the pronounced negative magnetoresistance [51, 62, 63, 65, 66, 68–70] attributed to the phenomenon of the chiral anomaly [56–58], theoretically predicted nonlocal transport [107, 108], Majorana flat bands [71], as well as an unusual type of quantum oscillations (QOs) that involve both bulk and topologically protected surface states [72, 73].

Materials with linearly dispersing electrons respond in peculiar ways to the externally imposed elastic strain. In graphene, for instance, the effect of curvature is famously analogous to a pseudo-magnetic field [87, 88] that can be quite large and is known to generate pronounced Landau levels observed in the tunneling spectroscopy [89]. Recent theoretical work [92–95, 109] showed that similar effects can be anticipated in three-dimensional Dirac and Weyl semimetals, although the estimated field strengths in the geometries that have been considered are rather small (below 1 T in Ref. [94]). Ordinary quantum oscillations, periodic in $1/B$, have already been observed in Dirac semimetals $Cd_3As_2$ and $Na_3Bi$ [40, 73, 110, 111] but the magnetic field required is $B \gtrsim 2$T. This, then, would seem to rule out the observation of strain-induced QOs in the geometries considered previously.

In this chapter, by considering a new geometry – circular bend, we establish a completely new mechanism for QOs in Weyl semimetals with strain-induced pseudo-magnetic fields but in the complete absence of ordinary magnetic fields. The chapter is organized as follows. In Section 2.1, we discuss a 2-band toy model of Weyl semimetals. Such model is referred to as $\frac{1}{2}$-$Cd_3As_2$ because it characterizes one of the spin sectors of Dirac semimetal $Cd_3As_2$. In Section 2.2, we derive the pseudo-magnetic field induced by a circular bend deformation and show that it can be as large as 15T, which should be sufficient for the observation of QOs without ordinary magnetic fields. In Section 2.3, we show that the pseudo-magnetic field gives rise to Landau

levels, the necessary QO ingredient. In Section 2.4, we derive the longitudinal electric conductivity and demonstrate that it exhibits Shubnikov-de Haas oscillations [112] both below and above Lifshitz transition in zero ordinary magnetic field as long as the external strain is continuously tuned. Section 2.5 concludes the chapter and discusses the promising venue for realizing the strain-induced QOs.

## 2.1 Model of Weyl semimetals

In order to implement quantum oscillations with purely strain-induced pseudo-magnetic fields, the minimal model we require is a 2-band Dirac model of Weyl semimetals. In this section, we will introduce a toy model that can characterize Weyl semimetals.

Our starting point is Dirac semimetal $Cd_3As_2$ [40–45] which may be the best characterized representative of this class of materials. Our results are directly applicable also to $Na_3Bi$ [46–48] whose low-energy description is identical, and are easily extended to other Dirac and Weyl semimetals [52, 53, 85, 113–115]. We start from the tight-binding model formulated in Refs. [41, 46] which describes the low-energy physics of $Cd_3As_2$ by including the band inversion of its atomic Cd-5$s$ and As-4$p$ levels near the $\Gamma$ point. In the basis of the spin-orbit coupled states $|P_{\frac{3}{2}}, \frac{3}{2}\rangle$, $|S_{\frac{1}{2}}, \frac{1}{2}\rangle$, $|S_{\frac{1}{2}}, -\frac{1}{2}\rangle$, and $|P_{\frac{3}{2}}, -\frac{3}{2}\rangle$ the model is defined by a $4 \times 4$ matrix Hamiltonian

$$H_{\boldsymbol{k}} = \epsilon_{\boldsymbol{k}} + \begin{pmatrix} \mathcal{H}_{\boldsymbol{k}} & 0 \\ 0 & -\mathcal{H}_{\boldsymbol{k}} \end{pmatrix}, \tag{2.1}$$

on a simple rectangular lattice with lattice constants $a_{x,y,z}$, where

$$\mathcal{H}_{\boldsymbol{k}} = m_{\boldsymbol{k}}\tau^z + \Lambda(\tau^x \sin k_x a_x + \tau^y \sin k_y a_y). \tag{2.2}$$

$\tau^{x,y,z}$ are Pauli matrices in the orbital space and $m_{\boldsymbol{k}} = t_0 + t_1 \cos k_z a_z + t_2(\cos k_x a_x + \cos k_y a_y)$. The upper diagonal block $\mathcal{H}_{\boldsymbol{k}}$ realizes a toy model of a Weyl semimetal that we will use for our analytical and numerical calculations throughout the present chapter. It exhibits a pair of Weyl points, shown in Fig. 2.1(a), which are located at crystal momenta $\boldsymbol{K}_\eta = (0, 0, \eta Q)$ with $Q$ given by $\cos(aQ) = -(t_0 + 2t_2)/t_1$, where we have assumed cubic lattice geometry $a_x = a_y = a_z = a$. In the vicinity of such Weyl points, $\mathcal{H}_{\boldsymbol{K}_\eta + \boldsymbol{q}}$ realizes the standard Dirac Hamiltonian

$$\mathcal{H}_{\boldsymbol{K}_\eta + \boldsymbol{q}} = \mathcal{H}_{\boldsymbol{K}_\eta} + \boldsymbol{q} \cdot \nabla_{\boldsymbol{k}} \mathcal{H}_{\boldsymbol{k}}|_{\boldsymbol{K}_\eta} = \sum_i \hbar v_i^\eta q_i \tau^i = h_{\boldsymbol{q}}^\eta, \tag{2.3}$$

where the velocity is given by

$$(v_x^\eta, v_y^\eta, v_z^\eta) = \frac{a}{\hbar}(\Lambda, \Lambda, -\eta t_1 \sin Qa). \tag{2.4}$$

The chirality associated with each Weyl point is then determined by

$$\chi_\eta = \mathrm{sgn}(v_x^\eta v_y^\eta v_z^\eta) = -\eta \mathrm{sgn}(t_1), \tag{2.5}$$

indicating that the two Weyl points work as source and drain of Berry flux, respectively. The non-trivial topology encoded by $\mathcal{H}_{\boldsymbol{k}}$ can be unveiled by examining the electronic structure of $\mathcal{H}_{\boldsymbol{k}}$ regularized on a thin film as illustrated in Fig. 2.2(a). The energy bands of the Weyl semimetal thin film exhibit Weyl cones and arc states terminated at the Weyl points as shown in Fig. 2.3(a). To understand the appearance of such arc states, we calculate the Chern number of $\mathcal{H}_{\boldsymbol{k}}$ with momentum $k_z$ fixed and it reads

$$C_{k_z} = \frac{1}{2}[\mathrm{sgn}(t_0 + t_1 \cos k_z a + 2t_2) + \mathrm{sgn}(t_2)]. \tag{2.6}$$

For the parameters used in Fig. 2.3(a), we obtain

$$C_{k_z} = \begin{cases} 1 & |k_z| < Q \\ 0 & Q < |k_z| < \pi \end{cases}. \tag{2.7}$$

Therefore, each of the 2D slices of $\mathcal{H}_{\boldsymbol{k}}$ with topological $k_z$ realizes a Chern insulator with chiral edge states. The combination of these edge states leads to the surface states of the Weyl semimetal thin film.

The lower diagonal block $-\mathcal{H}_{\boldsymbol{k}}$ in Eq. 2.1 describes the spin-down sector of $Cd_3As_2$ and has identical spectrum. For our purpose, this term will not be considered in this chapter. But we will add it back in Appendix A to show that our theory for zero-field quantum oscillations in Weyl semimetals can be easily transplanted to Dirac semimetals. The diagonal term $\epsilon_{\boldsymbol{k}} = r_0 + r_1 \cos k_z a_z + r_2(\cos k_x a_x + \cos k_y a_y)$ in Eq. 2.1 encodes the particle-hole asymmetry in $Cd_3As_2$. It shifts the energy bands but does not affect the band topology. Therefore, we will neglect this term and add it back in Appendix A as well.

## 2.2 Strain-induced pseudo-magnetic field

In this section, we first derive the theory of the respondence of Weyl semimetals to a generic lattice deformation due to external strain. Then we apply

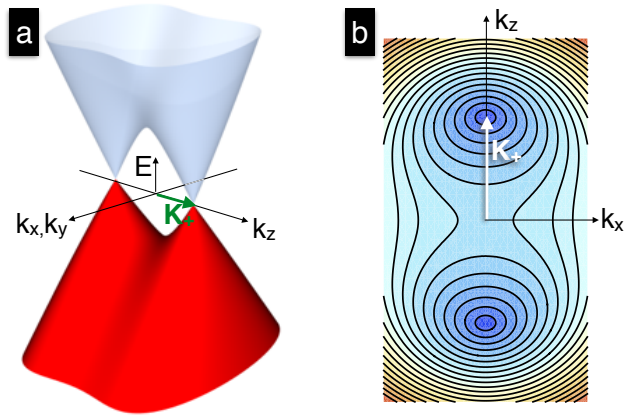


Figure 2.1: Schematic depiction of the low-energy electron excitation spectrum in Weyl semimetals. a) A pair of Weyl cones appear on $k_z$ axis. b) Contours of constant energy for $k_y = 0$.

the theory to a specific type of lattice deformation – circular bend and give the expression for the induced pseudo-magnetic field.

Following Refs. [92–94, 109], the most important effect of elastic strain can be included in the lattice model Eq. 2.2 by modifying the electron tunneling amplitude along the $z$ direction according to

$$t_1\tau^z \to t_1(1-u_{33})\tau^z + i\Lambda\sum_{j\neq 3} u_{3j}\tau^j, \tag{2.8}$$

where $u_{ij} = \frac{1}{2}(\partial_i u_j + \partial_j u_i)$ is the strain tensor and $\boldsymbol{u} = (u_1, u_2, u_3)$ represents the displacement of the atoms. The hopping integral substitution Eq. 2.8 produces a correction to the unstrained lattice Hamiltonian (Eq. 2.2), making the full Hamiltonian

$$\tilde{\mathcal{H}}_{\boldsymbol{k}} = \mathcal{H}_{\boldsymbol{k}} + \delta\mathcal{H}_{\boldsymbol{k}}, \tag{2.9}$$

where the correction is

$$\delta\mathcal{H}_{\boldsymbol{k}} = \Lambda u_{31}\sin k_z a\tau^x + \Lambda u_{32}\sin k_z a\tau^y - t_1 u_{33}\cos k_z a\tau^z. \tag{2.10}$$

In the vicinity of Weyl points, the low-energy theory for the strained Hamiltonian is

$$\mathcal{H}_{\boldsymbol{K}_\eta+q} + \delta\mathcal{H}_{\boldsymbol{K}_\eta+q} \approx h^\eta_{\boldsymbol{q}} + \delta\mathcal{H}_{\boldsymbol{K}_\eta} = \sum_i \hbar v^\eta_i\Big(q_i + \frac{e}{\hbar}\mathcal{A}_i\Big)\tau^i, \tag{2.11}$$

where the strain-induced gauge potential is

$$\mathcal{A} = \frac{\eta\hbar}{ea}(u_{31}\sin Qa, u_{32}\sin Qa, u_{33}\cot Qa). \tag{2.12}$$

We see that elements $u_{j3}$ of the strain tensor act on the low-energy Weyl fermions as components of a chiral gauge field, i.e., the strain-induced gauge potential $\mathcal{A}$, which oppositely couples to Weyl cones with different chirality $\chi_\eta$. On the other hand, ordinary electromagnetic vector potential couples through the same Peierls substitution $\boldsymbol{q} \to \boldsymbol{q} + \frac{e}{\hbar}\boldsymbol{A}$, but the vector potential $\boldsymbol{A}$ is independent of $\chi_\eta$. Ref. [94] noted that application of a torsional strain to a nanowire made of $Cd_3As_2$ (grown along the [001] crystallographic direction) results in a uniform pseudo-magnetic field $\boldsymbol{b} = \nabla \times \mathcal{A}$ pointed along the axis of the wire. The strength of this pseudo-magnetic field was estimated as $b \lesssim 0.3$T which would be insufficient to observe QOs. Our key observation here is that a different type of distortion – circular bend, illustrated in Fig. 2.2(a), can produce a much larger field $b$.

One reason why the torsion-induced $b$-field is relatively small lies in the fact that it originates from the $\mathcal{A}_x$ and $\mathcal{A}_y$ components of the vector potential. According to Eq. 2.12, these are suppressed relative to the strain components by a factor of $\sin aQ$. This is a small number in most Dirac and Weyl semimetals because the distance $2Q$ between the Weyl points is typically a small fraction of the Brillouin zone size $2\pi/a$. Specifically, we have $aQ \simeq 0.132$ in $Cd_3As_2$ [41]. Note on the other hand that the $\mathcal{A}_z$ component of the chiral gauge potential comes with a factor $\cot aQ \simeq 1/aQ$ and is therefore enhanced. A lattice distortion that produces nonzero strain tensor element $u_{33}$ will therefore be much more efficient in generating large $b$ than $u_{13}$ or $u_{23}$. Specifically, for the same amount of strain the field strength is enhanced by a factor of $\cot aQ/\sin aQ \simeq 1/(aQ)^2 \simeq 57$ for $Cd_3As_2$.

To implement this type of strain we consider a thin film (or a nanowire) grown such that vector $\boldsymbol{K}_\eta$ lies along the $z$ direction as defined in Fig. 2.2(a). More generally we require that $\boldsymbol{K}_\eta$ has a nonzero projection onto the surface of the film or on the long direction for the nanowire. $Cd_3As_2$ films [110], microribbons [116] and nanowires [117, 118] satisfy this requirement. Bending the film as shown in Fig. 2.2(b) creates a displacement field $\boldsymbol{u} = (0, 0, 2\alpha xz/d)$, where $d$ is the film thickness and $\alpha$ controls the magnitude of the bend. (If $R$ is the radius of the circular section formed by the bent film then $\alpha = 2d/R$. $\alpha$ can also be interpreted as the maximum fractional displacement $\alpha = u_{\max}/a$ that occurs at the surface of the film.) This distortion gives $u_{33} = 2\alpha x/d$ which, through Eq. 2.12, yields a pseudo-magnetic

field

$$\boldsymbol{b} = \nabla \times \mathcal{A} = -\hat{y}\frac{2\alpha}{d}\frac{\eta\hbar}{ea}\cot Qa. \tag{2.13}$$

Noting that $\Phi_0 = h/e = 4.12 \times 10^5 \mathrm{T\mathring{A}}^2$, we may estimate the magnitude of the pseudo-magnetic field for a $d = 100$nm film as

$$b \simeq \alpha \times 246\mathrm{T}. \tag{2.14}$$

The maximum pseudo-magnetic field that can be achieved will depend on the maximum strain that the material can sustain. Ref. [117] characterized the $Cd_3As_2$ nanowires as "greatly flexible" and their Fig. 1(a) shows some wires bent with a radius $R$ as small as several microns. This implies that $\alpha$ of several percent can likely be achieved. From Eq. 2.13 we thus estimate that field magnitude $b \simeq 10 - 15$T can be reached, providing a substantial window for the observation of the strain-induced QOs.

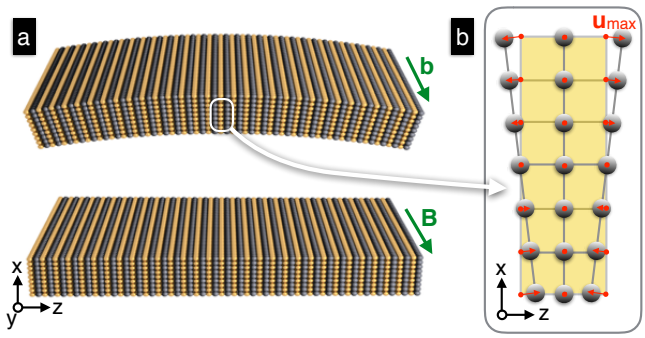


Figure 2.2: Proposed setup for strain-induced quantum oscillation observation in Weyl semimetals. a) Bent film is analogous, in terms of its low-energy properties, to an unstrained film subjected to magnetic field $B$. b) Detail of the atomic displacements in the bent film. Displacements have been exaggerated for clarity.

## 2.3 Band structure of Weyl semimetals

In Section 2.2, we argued that the strain-induced pseudo-magnetic field in a bent Weyl semimetal thin film can be sufficiently large for the observation of quantum oscillations. Since the necessary ingredient of quantum oscillation is Landau levels, in the present section, we will numerically examine the

presence of strain-induced pseudo-Landau levels, paying close attention to its similarity to the Dirac-Landau levels due to the ordinary magnetic field.

We first consider an unstrained Weyl semimetal thin film whose geometry is outlined in Fig. 2.2 with periodic boundary conditions along $y$ and $z$, open boundary condition along $x$. Fig. 2.3(a) summarizes the numerically calculated electronic structure and density of states (DOS) of such thin film in the absence of external magnetic field. The band structure shows bulk Weyl nodes close to $k_z a = \pm 0.2$ and a pair of linearly dispersing surface states corresponding to Fermi arcs. The DOS exhibits the quadratic behavior $D(E) \sim E^2$ at low energies with some deviations apparent for $|E| \gtrsim 12$meV. The numerical results can be understood by analytically deriving the effective low-energy theory band structure

$$E^a_{\boldsymbol{q}} = \pm\hbar\sqrt{(v^\eta_x q_x)^2 + (v^\eta_y q_y)^2 + (v^\eta_z q_z)^2}, \tag{2.15}$$

and the associated DOS

$$D_a(E) = V\int \frac{d^3\boldsymbol{q}}{(2\pi)^3}\delta(E - E^a_{\boldsymbol{q}}) = \frac{L_x L_y L_z E^2}{2\pi^2\hbar^3|v^\eta_x v^\eta_y v^\eta_z|}. \tag{2.16}$$

And the deviation of $D(E)$ of numerical results from the analytical results at higher energies is due to the departure of the lattice model from the perfectly linear Weyl dispersion. At $E_{\text{Lif}} \simeq 20$meV, Lifshitz transition occurs where two small Fermi surfaces associated with each Weyl point merge into a single large Fermi surface as illustrated in Fig. 2.1(b).

In Fig. 2.3(b), magnetic field $\boldsymbol{B} = \hat{y}B$ is seen to reorganize the linearly dispersing bulk bands into flat Landau levels. In the continuum approximation given by Eq. 2.11, according to Eq. 1.14, the bulk spectrum of such Dirac-Landau levels reads

$$E^b_{\boldsymbol{q}} = \pm\hbar\sqrt{(v^\eta_y q_y)^2 + 2n\left|\frac{eB}{\hbar}v^\eta_x v^\eta_z\right|} \quad n = 1, 2, \cdots, \tag{2.17}$$

whose DOS is given by

$$D_b(E) = V\int \frac{d^3\boldsymbol{q}}{(2\pi)^3}\delta(E - E^b_{\boldsymbol{q}}) = \frac{L_x L_z}{2\pi l_B^2}\frac{L_y}{\pi\hbar|v^\eta_y|}\sum_n \sqrt{\frac{E^2}{E^2 - 2n|\frac{eB}{\hbar}v^\eta_x v^\eta_z|}}, \tag{2.18}$$

where the magnetic length is $l_B = \sqrt{\hbar/e|B|}$. Such DOS shows a series of spikes at the onset of each new Landau level and is in a good agreement with the DOS calculated from the lattice model by using the tetrahedron method (see Appendix F for details). Deviations occur above $\sim 12$meV because the

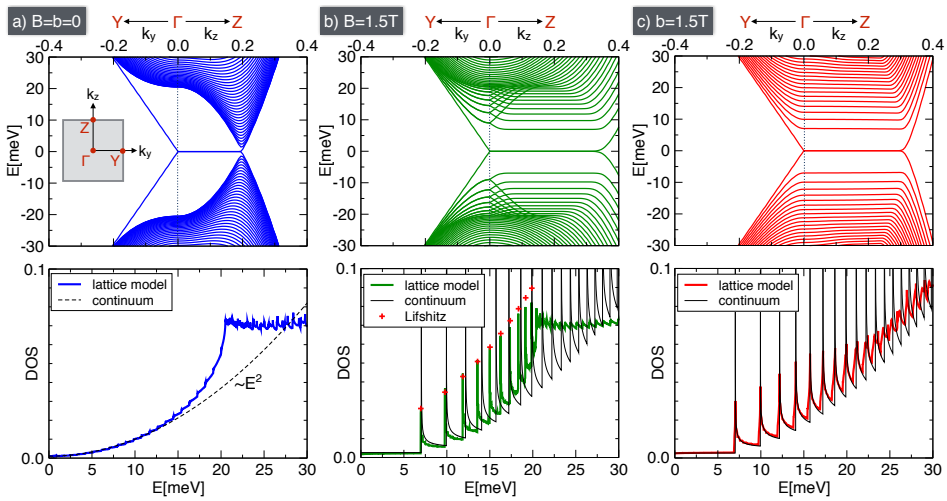


Figure 2.3: Band structure and DOS for lattice Hamiltonian Eq. 2.2. In all panels, films of thickness 500 lattice points are studied with parameters $t_0 = -2.522$eV, $t_1 = 1.042$eV, $t_2 = 0.75$eV, and $\Lambda = 0.148$eV. (a) Band structure and DOS for zero field and zero strain. The inset shows the first Brillouin zone. The dashed parabolic curve is the expected DOS (Eq. 2.16) for ideal Weyl dispersion (Eq. 2.15). (b) Band structure and normalized DOS for $B = 1.5$T. The solid black curve comprised of spikes at Landau levels is the expected DOS (Eq. 2.18) calculated from Dirac-Landau levels (Eq. 2.17). Red crosses indicate the peak positions expected on the basis of the Lifshitz-Onsager quantization condition. (c) Band structure and DOS for $b = 1.5$T. The solid black curve comprised of spikes at pseudo-Landau levels is the expected DOS (Eq. 2.20) calculated from pseudo-Landau levels (Eq. 2.19).

energy dispersion of the lattice model is no longer perfectly linear at higher energies. The peak positions $E_n$ agree perfectly with the Lifshitz-Onsager quantization condition [112], which takes into account these deviations. It requires that $S(E_n) = 2\pi n(eB/\hbar)$, where $S(E)$ is the extremal cross-sectional area of a surface of constant energy $E$ in the plane perpendicular to $\boldsymbol{B}$ and $n = 1, 2, \cdots$.

In Fig. 2.3(c), we find that the pseudo-magnetic field $\boldsymbol{b}$ induced by strain using Eq. 2.8 with $u_{33} = 2\alpha x/d$, also generates flat Landau levels and DOS comprised of spikes at each Landau level. Analytically, the low-energy spectrum and DOS can be directly written down by comparing to Eq. 2.17 and

Eq. 2.18 as

$$E^c_{\boldsymbol{q}} = \pm\hbar\sqrt{(v^\eta_y q_y)^2 + 2n\left|\frac{eb}{\hbar}v^\eta_x v^\eta_z\right|} \quad n = 1, 2, \cdots, \tag{2.19}$$

and

$$D_c(E) = V\int\frac{d^3\boldsymbol{q}}{(2\pi)^3}\delta(E - E^c_{\boldsymbol{q}}) = \frac{L_x L_z}{2\pi l_b^2}\frac{L_y}{\pi\hbar|v^\eta_y|}\sum_n\sqrt{\frac{E^2}{E^2 - 2n|\frac{eb}{\hbar}v^\eta_x v^\eta_z|}}, \tag{2.20}$$

where $l_b = \sqrt{|\hbar/eb|}$ is the magnetic length of the pseudo-magnetic field. It is worth noting that Eq. 2.20 agrees with the numerically calculated DOS perfectly for all energies up to $E_{\mathrm{Lif}}$, unlike Eq. 2.18 which begins to deviate from the numerics at $\sim$ 12meV. We attribute this interesting result to the fact that strain couples as the chiral vector potential *only* to Weyl fermions. If we write the full Hamiltonian as $h(\boldsymbol{p}) = h_W(\boldsymbol{p}) + \delta h(\boldsymbol{p})$ where $h_W$ is strictly linear in momentum $\boldsymbol{p}$ and $\delta h$ is the correction resulting from the lattice effects, then strain causes $\boldsymbol{p} \to \boldsymbol{p} + e\mathcal{A}$ only in $h_W$ but does not to the leading order affect $\delta h$. On the other hand, the vector potential $\boldsymbol{A}$ of magnetic field $\boldsymbol{B}$ affects $h_W$ and $\delta h$ in the same way.

Before we leave this section, we further test the equivalence of the strain-induced pseudo-magnetic field $\boldsymbol{b}$ and the ordinary magnetic field $\boldsymbol{B}$. We propose to apply external magnetic field of fixed strength and then slowly turn on strain (or vice versa, whichever is more convenient in a particular experimental design). We find this will result in splitting of the first peak in DOS as illustrated in Fig. 2.4. This happens because the two Weyl cones will feel different effective magnetic fields. Due to the chiral nature of the gauge field Eq. 2.12, the strain-induced pseudo-magnetic field takes opposite values at different Weyl cones (Eq. 2.13), while the ordinary magnetic field is uniform in the crystal. Consequently, the two Weyl cones feel effective magnetic field $B+b$ and $B-b$, respectively, which results in two independent sequences of peaks in DOS. Observation of the splitting would prove the identical nature of the gauge and external magnetic fields in each of the Weyl cones.

## 2.4 Longitudinal electric conductivity

In Section 2.3, we have confirmed that the necessary QO ingredient – Landau levels occur in the presence of strain. In Section 2.2, we have demonstrated that the strain-induced pseudo-magnetic field has a substantial win-

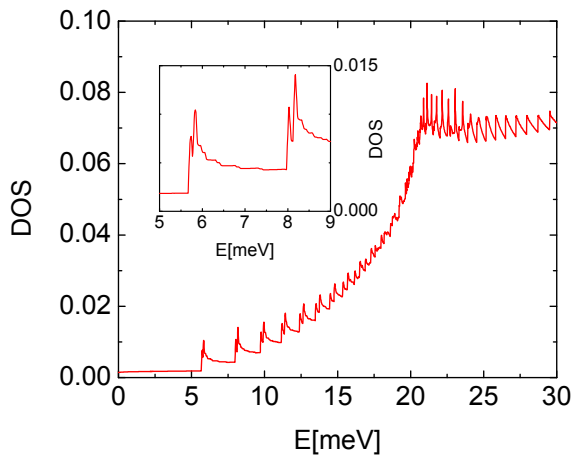


Figure 2.4: Normalized density of states for both fields present, $B = 1$T and $b = 0.0184$T. Each of the DOS peaks due to ordinary magnetic field splits due to torsion thus proving the equivalence of the external and gauge fields. Inset gives closer view of the first two peaks.

dow. These findings make the observation of QOs possible with strain-induced pseudo-magnetic field only. Specifically, when continuously tuning the strain-induced pseudo-magnetic field $\boldsymbol{b}$, nearly all observables (e.g., electric conductivity, thermal conductivity, magnetization) exhibit oscillating behaviors periodic in $1/b$ because these observables are dominated by the DOS at Fermi surface, which is periodic in $1/b$ as elucidated in Eq. 2.20. From the experimental point of view, the longitudinal electric conductivity QO may be the easiest to measure. Therefore, in the present section, we will derive the longitudinal electric conductivity $\sigma_{yy}$ as a function of pseudo-magnetic field and show it indeed exhibits the Shubnikov-de Haas (SdH) oscillation.

We use Boltzmann equation approach [81] to calculate the longitudinal electric conductivity. Without loss of generality, we will assume positive chemical potential $\mu > 0$. The conductivity of the $n$-th band reads

$$\sigma_n(\mu) = e^2 \frac{L_x L_z}{2\pi l_b^2} L_y \int \frac{dk_y}{2\pi} \tau_n(E_n^2(k_y))(v_n(k_y))^2 \left( -\frac{\partial f(E-\mu)}{\partial E} \right)_{E_n(k_y)}, \tag{2.21}$$

where $f(\epsilon)$ is the Fermi function and $\tau_n(E_n^2(k_y))$ is the relaxation time. The

velocity can be derived from Eq. 2.19 as

$$v_n(k_y) = \frac{1}{\hbar}\frac{\partial E_n}{\partial k_y} = v_y^\eta \frac{k_y}{\sqrt{k_y^2 + 2n\left|\frac{eb}{\hbar}\frac{v_x^\eta v_z^\eta}{(v_y^\eta)^2}\right|}}. \tag{2.22}$$

We assume zero temperature, angle-independent relaxation time, and substitute the dispersion relation Eq. 2.19 to obtain

$$\sigma_n(\mu) = \frac{e^2\tau_n v_y^\eta}{\pi\hbar}\frac{L_x L_z}{2\pi l_b^2}L_y\sqrt{\frac{\mu^2 - 2n|\frac{eb}{\hbar}\hbar^2 v_x^\eta v_z^\eta|}{\mu^2}} \quad n = 1, 2, \cdots, n_{\max}, \tag{2.23}$$

where $n_{\max} = [\mu^2/2|\frac{eb}{\hbar}\hbar^2 v_x^\eta v_z^\eta|]$[6]. Physically, this indicates only those Dirac-Landau levels that traverse chemical potential contribute to the conductivity. The total longitudinal electric conductivity is then

$$\sigma_{yy}(\mu) = \frac{e^2 v_y^\eta}{\pi\hbar}\frac{L_x L_z}{2\pi l_b^2}L_y\sum_{n=0}^{n_{\max}}\tau_n(\mu)\sqrt{\frac{\mu^2 - 2n|\frac{eb}{\hbar}\hbar^2 v_x^\eta v_z^\eta|}{\mu^2}}. \tag{2.24}$$

Finally, we estimate the relaxation time in the lowest order Born approximation [119]

$$\frac{1}{\tau} = \frac{2\pi}{\hbar}D(\mu)n_{\text{imp}}C, \tag{2.25}$$

where $D(\mu)$ is the density of states at the Fermi level and $n_{\text{imp}}$ is the impurity concentration. Constant $C$ depends on the details of scattering from impurities. Thus the final formula we use for the conductivity computation in Fig. 2.4 is

$$\begin{aligned}\sigma_{yy}(\mu) &= \frac{e^2 v_y^\eta}{\pi\hbar}\frac{L_x L_z}{2\pi l_b^2}L_y\frac{1}{\frac{2\pi}{\hbar}n_{\text{imp}}C}\frac{1}{D(\mu)}\sum_{n=0}^{n_{\max}}\sqrt{\frac{\mu^2 - 2n|\frac{eb}{\hbar}\hbar^2 v_x^\eta v_z^\eta|}{\mu^2}} \\ &= \sigma_{yy}(0)\sum_{n=0}^{n_{\max}}\sqrt{\frac{\mu^2 - 2n|\frac{eb}{\hbar}\hbar^2 v_x^\eta v_z^\eta|}{\mu^2}}\Bigg/\sum_{n=0}^{n_{\max}}\sqrt{\frac{\mu^2}{\mu^2 - 2n|\frac{eb}{\hbar}\hbar^2 v_x^\eta v_z^\eta|}},\end{aligned} \tag{2.26}$$

where we have used Eq. 2.20 and we have defined zero strain electric conductivity as

$$\sigma_{yy}(0) = \frac{e^2(v_y^\eta)^2}{\frac{2\pi}{\hbar}n_{\text{imp}}C}. \tag{2.27}$$

[6] The notation $[x]$ means an integer that is no greater than $x$.

It is easy to see that when continuously tuning the external strain, the induced pseudo-magnetic field scans, and the Landau levels successively fall off the chemical potential $\mu$. Every time a new Landau level hits the chemical potential, we have condition $\mu^2 = 2n|\frac{eb}{\hbar}\hbar^2 v_x^\eta v_z^\eta|$, $\sigma_{yy}(\mu)$ hits a valley while the corresponding DOS $D_c(\mu)$ hits a peak, according to Eq. 2.26 and Eq. 2.20, respectively. Both of them exhibit quantum oscillation periodic in $1/b$. The same is true for the ordinary magnetic field as long as $\boldsymbol{b}$ is replaced by $\boldsymbol{B}$.

Numerically, we can use Eq. 2.26 to calculate the longitudinal electric conductivity but input the actual numerically calculated velocities and energies into it. In order to obtain satisfying resolution, we apply the tetrahedron method (see Appendix F for details) when calculating DOS and longitudinal electric conductivity. As illustrated in Fig. 2.5, both DOS and longitudinal electric conductivity show oscillations periodic in $1/B$ and $1/b$, at chemical potential $\mu = 10$meV. The latter realizes zero-field QOs, which is the key result of the present chapter. The period of the strain-induced QO $0.329\mathrm{T}^{-1}$ in Fig. 2.5 is in a good agreement with the period $0.324\mathrm{T}^{-1}$ expected on the basis of the Lifshitz-Onsager theory and the period $0.336\mathrm{T}^{-1}$ obtained from Eq. 2.19. Small irregularities that appear at low fields can be attributed to the finite size effects as the Landau level spacing becomes comparable to the sub-band spacing, e.g., Fig. 2.3(a). We further verify that similar oscillations occur at other energies below the Lifshitz transition $E_{\mathrm{Lif}} \sim 20$meV.

Above the Lifshitz transition, at chemical potential $\mu = 28$meV, we see the QOs still happen for the strain-induced pseudo-magnetic field in Fig. 2.6(a). However, the period of such QOs is different from that of the QOs due to the ordinary magnetic field by a factor of 2 approximately. The physics behind this can be clarified by considering the extremal cross-sectional area of Fermi surface. For the ordinary magnetic field $\boldsymbol{B}$, above the Lifshitz transition, the two Weyl cones merge into a larger Fermi surface so that the effective area of Fermi surface is approximately doubled as illustrated by the green contour in Fig. 2.6(b). On the other hand, strain couples only to the linear part of the Hamiltonian as a gauge field, therefore only the oscillations around each of the Weyl points are possible as illustrated by the red contours in Fig. 2.6(b), on which the electron in the pseudo-magnetic field travels clockwise around one of the Weyl points and counterclockwise around the other. The precise nature of the corresponding quasi-classical trajectories above the Lifshitz transition is therefore an interesting open question which we leave for further study. We speculate that it includes tunneling between the opposite points of the Fermi surface as depicted in Fig. 2.6(b). Such trajectories would define an extremal area

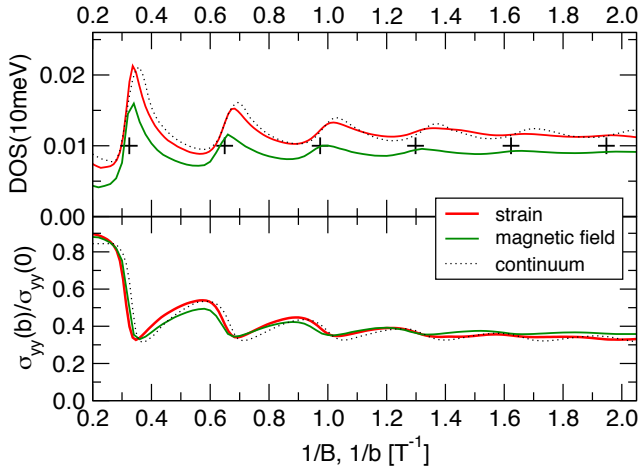


Figure 2.5: Strain-induced quantum oscillations. Top panel shows oscillations in DOS at $\mu = 10$meV as a function of inverse strain strength expressed as $1/b$. For comparison ordinary magnetic oscillations are displayed, as well as the result of the bulk continuum theory Eq. 2.18. Crosses indicate peak positions expected based on the Lifshitz-Onsager theory. Bottom panel shows SdH oscillations in conductivity $\sigma_{yy}$ assuming chemical potential $\mu = 10$meV. To simulate the effect of disorder all data are broadened by convolving in energy with a Lorentzian with width $\delta = 0.25$meV. The same geometry and parameters are used as in Fig. 2.3.

consistent with our numerical results.

To better simulate QOs for realistic Weyl semimetals, the curves (Eq. 2.20 and Eq. 2.26) shown in Fig. 2.5 and Fig. 2.6(a) have been convolved in energy with a Lorentzian of width $\delta = 0.25$meV, which corresponds to Landau level broadening due to scattering from phonons and impurities at finite temperature. Such broadening may be derived by the Born approximation [120] and exhibits $\sqrt{B}$ dependence for Weyl semimetals [121]. Experimentally, for Dirac semimetal $Cd_3As_2$ to which our simulation is closely relevant, the broadening can be obtained by phenomenologically fitting to experimental data such as the zero magnetic field optical conductivity [122] and SdH oscillations [123]. Specifically, the former suggests a 15meV broadening at T=10K while the later exhibits a broadening within 0.02∼20meV at T=2.5K. From the width of differential conductance peaks in STM measurements [44, 124], the Landau level broadening of several milli-electronvolts can be approximated. For the sake of transparency, we have chosen a $B$-independent value

$\delta = 0.25$meV for the Lorentzian width, which should be experimentally available in sufficiently clean sample of $Cd_3As_2$ at low temperature.

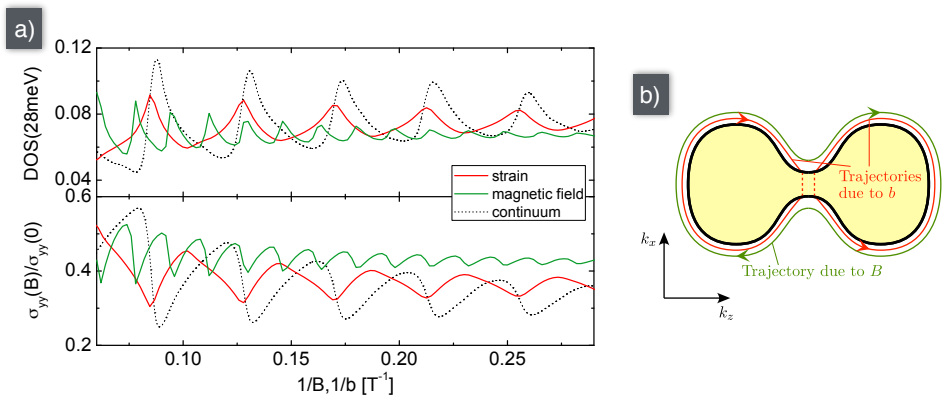


Figure 2.6: Quantum oscillations above Lifshitz transition. (a) QOs above the Lifshitz transition due to ordinary magnetic field and due to strain-induced pseudo-magnetic field. Period difference by approximately a factor of 2 is seen. The low-energy analytic theory does not apply anymore, as expected. (b) Corresponding hypothesized quasi-classical trajectories of electrons in the Brillouin zone. Green for $B_y$ field and red for $b_y$ field.

## 2.5 Summary

In this chapter, we have seen that quantum oscillations occur in the absence of magnetic fields as long as a circular bend deformation is applied and tuned continuously. Our argument is numerically supported by studying a 2-band toy model of Weyl semimetal – $\frac{1}{2}$-$Cd_3As_2$, which can be understood as one of the spin sectors of real Dirac semimetal $Cd_3As_2$. As discussed in Section 2.1, the other spin sector contributes to the band structure identically and $\epsilon_{\boldsymbol{k}}$ only shifts bands trivially; we thus argue that the full $Cd_3As_2$ Hamiltonian Eq. 2.1 also exhibits strain-induced Dirac-Landau levels (Appendix A). Since all the numerical simulation presented in this chapter is conducted using the parameters of $Cd_3As_2$, we argue that Dirac semimetal $Cd_3As_2$ may be an ideal candidate material to implement strain-induced QOs. Moreover, experimental studies [42–45] indicate that the linear dispersion in $Cd_3As_2$ extends over a much wider range of energies than theoretically anticipated [41] with Lifshitz transition occurring near 200 meV. All these findings render

$Cd_3As_2$ even more promising for the observation of zero-field QOs.

# Chapter 3

# Dirac-Landau levels in Weyl superconductors

Quantum oscillations [112] furnish an essential experimental tool for measuring the Fermi surface of metals. They also help to understand electronic structures of the recently discovered topological insulators [125–129] and topological Dirac and Weyl semimetals [40, 73, 111, 130]. However, probing superconductors by the quantum oscillation technique has been thought impossible because such measurements require strong magnetic fields which are either expelled from the SC due to the Meissner effect or render the material normal. Type-II superconductors allow the field to penetrate but form the Abrikosov vortex state, whose quasiparticle eigenstates are known to be Bloch waves rather than Landau levels [131–133].

Quantum oscillations in resistivity [98–100], Hall coefficient [101], thermal conductivity [102], and torque [103] have already been observed in underdoped cuprates when magnetic field suppresses superconductivity. Quantum oscillations with $1/\sqrt{B}$ periodicity have also been predicted to appear in vortex lattice [105] and vortex liquid states [104] in cuprates and are observed in 2H-$NbSe_2$ [106]. However, reports on conventional quantum oscillations periodic in $1/B$ in the superconducting state are lacking presumably due to the reasons listed above.

Inspired by the work presented in Chapter 2, we hypothesize that such difficulty can be overcome by using the strain-induced pseudo-magnetic field whose quantum oscillations rely on continuously tuned lattice deformation rather than scanning magnetic field [134]. It has been proved that the strain-induced pseudo-magnetic field is not subject to Meissner effect or vortex states [135]. Such unique feature makes the pseudo-magnetic field compatible with superconductivity. Therefore, pseudo-magnetic field quantum oscillations periodic in $1/b$ are in principle available in the superconducting regime. Since pseudo-magnetic field is a common feature of Dirac materials such as graphene [87–89] and Dirac/Weyl semimetals [92–97, 134], the best candidate materials to exhibit pseudo-magnetic field may be the 2D $d$-wave superconductors and the 3D Dirac/Weyl superconductors [18, 19]. The

$d$-wave superconductors have been verified to host strain-induced pseudo-magnetic fields [136, 137]. Whether similar effect could be obtained in the Dirac/Weyl superconductors remains as an open question and is the central concern of the present chapter.

In this chapter, through a combination of analytical calculations and numerical simulations, we demonstrate that quantum oscillations indeed occur in Weyl superconductors under certain types of elastic deformations at zero magnetic field. Remarkably, these quantum oscillations arise due to the formation of Landau levels comprised of *charge neutral* Bogoliubov quasiparticles deep in the superconducting state. The chapter is organized as follows. In Section 3.1, we formulate a model of a Weyl superconductor and discuss its spectrum and phase diagram. In Section 3.2, we incorporate strain to our Hamiltonian and show that to the leading order it produces a pseudo-magnetic field in the low-energy sector. In Section 3.3, we derive the band structure of a Weyl superconductor away from the neutrality point and show that this is necessary to obtain a non-zero Fermi surface. In Section 3.4, we show that the strain-induced pseudo-magnetic field can give rise to quantum oscillations in density of states (DOS) and longitudinal thermal conductivity. Section 3.5 concludes the chapter by discussing the experimental feasibility in candidate materials and outlines various potentially interesting directions.

## 3.1 Model of Weyl superconductors

To implement strain-induced quantum oscillation, we first require a Weyl superconductor. We thus employ the multilayer model invented by Meng and Balents [18] as illustrated in Fig. 3.1. The model comprises alternating topological insulator (TI) and $s$-wave superconductor (SC) layers stacked along the $z$ direction. For the TI layers, for simplicity, only the surface states are considered. In the following we modify the Meng-Balents model slightly by adding anisotropy to the Zeeman mass term, which will allow us regularize the Hamiltonian on the tight binding lattice without adding extra Weyl points near the corners of the Brillouin zone.

The Hamiltonian of such a TI-SC multilayer system reads

$$H = H_{\mathrm{TI}} + H_{\mathrm{SC}} + H_{t_d} + H_{t_s}, \tag{3.1}$$

where

$$H_{\mathrm{TI}} = \sum_{\boldsymbol{k}_\perp, z} \psi^\dagger_{\boldsymbol{k}_\perp z}[\hbar v_F \sigma^z (\hat{z} \times \boldsymbol{s}) \cdot \boldsymbol{k}_\perp + (m - m' a^2 k_\perp^2) s^z] \psi_{\boldsymbol{k}_\perp z},$$

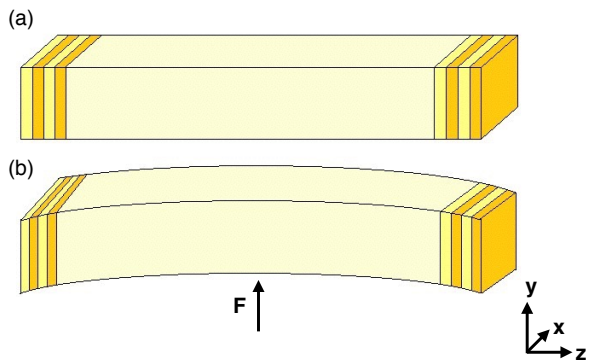


Figure 3.1: Schematic plot for (a) undeformed and (b) bent TI-SC multilayer Weyl superconductor. The alternating TI and SC layers are omitted in the bulk but explicitly drawn at ends to illustrate that there are integer number of unit cells comprised of one TI layer and one SC layer.

$$H_{\mathrm{SC}} = \sum_{\boldsymbol{k}_\perp, z} (\Delta c^\dagger_{\boldsymbol{k}_\perp z, 1\uparrow} c^\dagger_{-\boldsymbol{k}_\perp z, 1\downarrow} + \Delta c^\dagger_{\boldsymbol{k}_\perp z, 2\uparrow} c^\dagger_{-\boldsymbol{k}_\perp z, 2\downarrow}) + \mathrm{h.c.},$$

$$H_{t_d} = \sum_{\boldsymbol{k}_\perp, z} \left( \frac{1}{2} t_d \psi^\dagger_{\boldsymbol{k}_\perp z+1} \sigma^+ \psi_{\boldsymbol{k}_\perp z} + \frac{1}{2} t_d \psi^\dagger_{\boldsymbol{k}_\perp z-1} \sigma^- \psi_{\boldsymbol{k}_\perp z} \right),$$

$$H_{t_s} = \sum_{\boldsymbol{k}_\perp, z} \psi^\dagger_{\boldsymbol{k}_\perp z} t_s \sigma^x \psi_{\boldsymbol{k}_\perp z}.$$

The basis $\psi_{\boldsymbol{k}_\perp z} = (c_{\boldsymbol{k}_\perp z, 1\uparrow}, c_{\boldsymbol{k}_\perp z, 1\downarrow}, c_{\boldsymbol{k}_\perp z, 2\uparrow}, c_{\boldsymbol{k}_\perp z, 2\downarrow})^T$ is written in terms of annihilation operators $c_{\boldsymbol{k}_\perp z, \sigma s}$ for electrons located in the $z$-th unit cell with an in-plane momentum $\boldsymbol{k}_\perp = (k_x, k_y)$ and spin projection $s_z = \uparrow, \downarrow$. "Sublattice" labels $\sigma_z = 1, 2$ specify the TI-SC interface in the single unit cell. Pauli matrices $\boldsymbol{s}$ and $\boldsymbol{\sigma}$ act in spin and sublattice space, respectively. Physically, $H_{\mathrm{TI}}$, $H_{\mathrm{SC}}$, $H_{t_d}$, and $H_{t_s}$ can be interpreted as describing the Zeeman gapped topological insulator surface states, proximity-induced pairing, hopping between adjacent unit cells, and hopping within a single unit cell, respectively. The $m'$ term in $H_{\mathrm{TI}}$ represents the above mentioned modification of the Meng-Balents model (it is easy to check that it has no significant effect at small $k$ as long as $m'$ is chosen appropriately small).

As written Hamiltonian Eq. 3.1 is $\boldsymbol{k} \cdot \boldsymbol{p}$ in $x$-$y$ plane and tight-binding in $z$ direction. It will be useful to apply lattice regularization. We use a

simple cubic lattice with lattice constant $a$ and replace $k_{x,y} \to \frac{1}{a}\sin ak_{x,y}$ and $k_{x,y}^2 \to \frac{2}{a^2}(1-\cos ak_{x,y})$. After partial Fourier transform in the $z$ direction, the Hamiltonian can be written as

$$H = \frac{1}{2}\sum_{\boldsymbol{k}} \Psi_{\boldsymbol{k}}^\dagger \mathcal{H}_{\boldsymbol{k}} \Psi_{\boldsymbol{k}}, \tag{3.2}$$

with $\Psi_{\boldsymbol{k}} = (c_{\boldsymbol{k},1\uparrow}, c_{\boldsymbol{k},1\downarrow}, c_{\boldsymbol{k},2\uparrow}, c_{\boldsymbol{k},2\downarrow}, c^\dagger_{-\boldsymbol{k},1\uparrow}, c^\dagger_{-\boldsymbol{k},1\downarrow}, c^\dagger_{-\boldsymbol{k},2\uparrow}, c^\dagger_{-\boldsymbol{k},2\downarrow})^T$ and

$$\begin{aligned}\mathcal{H}_{\boldsymbol{k}} = (m - 4m' + 2m'\cos k_x a + 2m'\cos k_y a)s^z\tau^z + \\ t_d \sin k_z a \sigma^y \tau^z + (t_s + t_d \cos k_z a)\sigma^x\tau^z + \frac{\hbar v_F}{a}\sin k_y a s^x \sigma^z \\ - \frac{\hbar v_F}{a}\sin k_x a s^y \sigma^z \tau^z - \mathrm{Im}\Delta s^y \tau^x - \mathrm{Re}\Delta s^y \tau^y.\end{aligned} \tag{3.3}$$

The spectrum of $\mathcal{H}_{\boldsymbol{k}}$ reads

$$\begin{aligned}\epsilon_{\boldsymbol{k},\pm}^2 = \frac{\hbar^2 v_F^2}{a^2}(\sin^2 k_x a + \sin^2 k_y a) + \Big(m - 4m' + 2m'\cos k_x a \\ + 2m'\cos k_y a \pm \sqrt{t_s^2 + t_d^2 + 2t_s t_d \cos k_z a + |\Delta|^2}\Big)^2.\end{aligned} \tag{3.4}$$

We plot the spectrum in Fig. 3.2 for a system with $\bar{l}_y = 500$ layers and open boundary conditions along the $y$-direction and periodic boundary conditions in the other two dimensions. We set $\Delta = 1$ and measure all other parameters in terms of $\Delta$. We take $m = 10.26$, $m' = 2.53$, $\hbar v_F/a = 1$, $t_d = -4.79$, $t_s = 14.86$, and the lattice constant is set to be $a = 6$Å. These values will also be used in our numerical simulations unless other values are specified.

Without loss of generality, we have assumed $m, m' > 0$ in the following discussion. Thus, the sector $\epsilon_{\boldsymbol{k},+}$ is fully gapped while $\epsilon_{\boldsymbol{k},-}$ can be gapless when

$$\sqrt{(|t_s| - |t_d|)^2 + |\Delta|^2} < m < \sqrt{(|t_s| + |t_d|)^2 + |\Delta|^2}. \tag{3.5}$$

If Eq. 3.5 holds, non-degenerate quasiparticle bands exhibit a pair of nodes at $\boldsymbol{k}_W = (0, 0, \eta Q)$ with

$$Qa = \cos^{-1}\left(\frac{m^2 - t_s^2 - t_d^2 - |\Delta|^2}{2t_s t_d}\right), \tag{3.6}$$

and $\eta = \pm 1$. As expected, the system is a Weyl superconductor.

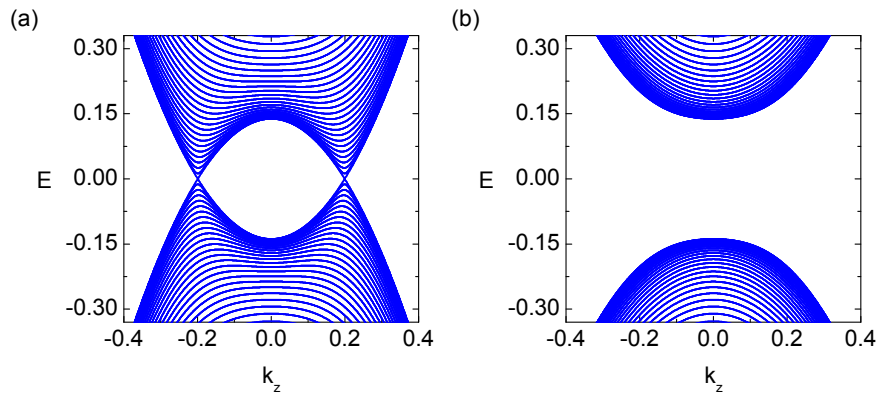


Figure 3.2: Band structure of a Weyl superconductor plotted (a) along $k_z$ axis with $k_x = 0$ and (b) along $k_x$ axis with $k_z = 0$. Periodic boundary conditions are applied in $x, z$ directions while the system is chosen to have $\bar{l}_y = 500$ layers in $y$ direction. The parameters are listed below Eq. 3.4.

To understand the low-energy physics better, we introduce $2\times2$ auxiliary matrices

$$D_{\boldsymbol{k},\pm} = \frac{\hbar v_F}{a}\sin k_y a\kappa^x - \frac{\hbar v_F}{a}\sin k_x a\kappa^y + (M_{k_z,\pm} - 4m' + 2m'\cos k_x a + 2m'\cos k_y a)\kappa^z, \quad (3.7)$$

where $\boldsymbol{\kappa}$ are Pauli matrices in transformed Nambu space and

$$M_{k_z,\pm} = m \pm \sqrt{t_s^2 + t_d^2 + 2t_s t_d \cos k_z a + |\Delta|^2}.$$

As $\epsilon_{\boldsymbol{k},\pm}$ is also the dispersion for $D_{\boldsymbol{k},\pm}$, the low-energy physics of Eq. 3.3 may be understood by studying $D_{\boldsymbol{k},-}$ because there always exists a unitary transformation $U$ that can block diagonalize $\mathcal{H}_{\boldsymbol{k}}$

$$U^{-1}\mathcal{H}_{\boldsymbol{k}}U = \mathrm{diag}(D_{\boldsymbol{k},-}, D_{\boldsymbol{k},-}, D_{\boldsymbol{k},+}, D_{\boldsymbol{k},+}).$$

For fixed $k_z$ value, we rewrite $D_{\boldsymbol{k},-}$ in a $\boldsymbol{k}\cdot\boldsymbol{p}$ fashion,

$$D^-_{\boldsymbol{k}\cdot\boldsymbol{p}} = \begin{pmatrix} -m'a^2(k_x^2+k_y^2) + \mu_{\mathrm{eff}} & i\hbar v_F(k_x - ik_y) \\ -i\hbar v_F(k_x + ik_y) & m'a^2(k_x^2+k_y^2) - \mu_{\mathrm{eff}} \end{pmatrix}. \quad (3.8)$$

We notice that $D^-_{\boldsymbol{k}\cdot\boldsymbol{p}}$ can be regarded as describing a $p_x + ip_y$ superconductor with an effective chemical potential $\mu_{\mathrm{eff}} = M_{k_z,-}$. It is characterized by

Chern number

$$C = \frac{1}{2}[\mathrm{sgn}(\mu_{\mathrm{eff}}) + \mathrm{sgn}(m')]. \tag{3.9}$$

If Eq. 3.5 holds, for those $k_z$'s that satisfy $\mu_{\mathrm{eff}} = M_{k_z,-} > 0$, this SC is in the weak pairing phase with Chern number $C = 1$. As a result, for each of such $k_z$'s, there exist counter propagating chiral Majorana states on a pair of boundaries open in the $y$-direction. Therefore, the edge states of Eq. (3.1) are Majorana-Fermi arcs as illustrated in Fig. 3.3(a).

To understand the phases of this model, consider a value of $m$ that satisfies Eq. 3.5 with fixed $\Delta$. Now increase it such that $m > \sqrt{(|t_s| + |t_d|)^2 + |\Delta|^2}$; according to Eq. 3.4, our Weyl superconductor will be gapped into a topologically superconducting phase, whose spectrum is shown in Fig. 3.3(b). It exhibits a surface mode because the Chern number is still $C = 1$ for all $k_z$. On the other hand, if $m$ is decreased to $m < \sqrt{(|t_s| - |t_d|)^2 + |\Delta|^2}$, the system enters a trivially superconducting phase with no edge modes, as shown in Fig. 3.3(c). If $m$ is fixed to a value obeying Eq. 3.5, but $|\Delta|$ is gradually increased, eventually, $m$ is overwhelmed by $\sqrt{(|t_s| - |t_d|)^2 + |\Delta|^2}$ and the system becomes a trivial superconductor, as indicated by Fig. 3.3(d).

Based on the above considerations, we plot the global phase diagram of our Weyl superconductor in $|\Delta| - m$ plane in Fig. 3.4. The phase boundaries are given by two hyperbolas,

$$m^2 - |\Delta|^2 = (|t_s| + |t_d|)^2, \tag{3.10}$$

$$m^2 - |\Delta|^2 = (|t_s| - |t_d|)^2. \tag{3.11}$$

Above the upper bound Eq. 3.10, the multilayer is a topological superconductor, which can be viewed as a stack of 2D $p_x + ip_y$ superconductors. These are known to possess counter propagating chiral Majorana edge modes on a pair of parallel boundaries. Since switching off the superconductivity will give a 3D quantum anomalous Hall (QAH) insulator [38], the multilayer topological superconductor structure may be referred to as "3D QAH superconductor." Below the lower bound Eq. 3.11, the multilayer is a trivial superconductor while between them it is a Weyl superconductor.

## 3.2 Strain-induced pseudo-magnetic field

In Section 3.1, we studied electronic structure and phase diagram of multilayer model of Weyl superconductor. In this section, we will understand how the electronic structure is changed under generic strain.

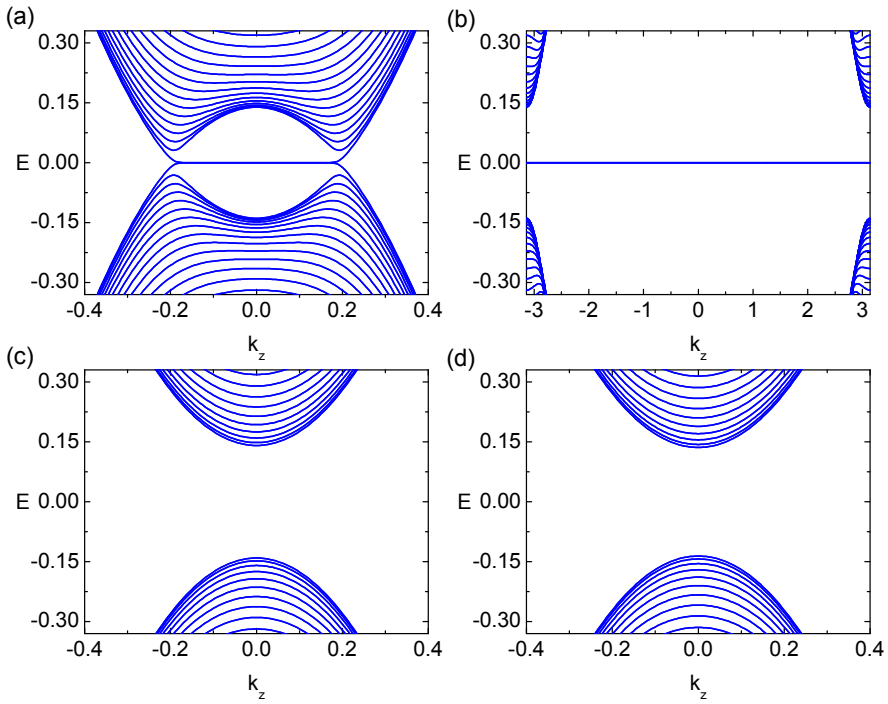


Figure 3.3: Band structure of a Weyl superconductor with open boundary conditions and $\bar{l}_y = 150$ layers along the $y$-direction. All panels are plotted along $k_z$-axis with $k_x = 0$ and with parameters as in Fig. 3.2. (a) Weyl superconductor phase for $(m, \Delta) = (10.26, 1)$. A Fermi arc connecting two Weyl points appears due to the chiral Majorana edge states of the effective $p_x + ip_y$ superconductors that emerge for fixed $k_z$ between the Weyl nodes. (b) Topological superconductor phase for $(m, \Delta) = (19.82, 1)$. The increase of $m$ will separate two Weyl points and extend Fermi arc. When two Weyl points meet at Brillouin zone boundary, they annihilate and open up a SC gap but leave behind the Fermi arc extended over the whole BZ. (c) Trivial superconductor phase for $(m, \Delta) = (9.98, 1)$. The decrease of $m$ makes two Weyl points meet at Brillouin zone center and annihilation and leads to the disappearance of the Fermi arc. (d) Trivial superconductor phase with $(m, \Delta) = (10.26, 2.56)$. The increase of $\Delta$ is equivalent to decrease of $m$ and Weyl points again annihilate at the BZ center.

When elastic strain distorts the lattice, the chemical bonds are stretched and compressed. Orbital orientations are also rotated, making the symmetry-

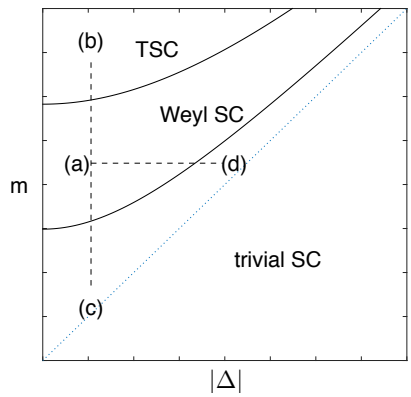


Figure 3.4: Phase diagram of the Weyl superconductor described by Hamiltonian Eq. 3.3 in terms of $(m, |\Delta|)$ with labels (a)-(d) correspond to spectra shown in Fig. 3.3(a)-(d). The two black curves mark the phase boundaries given in Eq. 3.10 and Eq. 3.11. The dotted line indicates the asymptote for the two phase boundaries.

prohibited hoppings now non-zero. For our purposes, the most important modification comes from the replacement of hopping amplitudes along $z$-direction [94, 109, 134]

$$\begin{aligned} t_d\sigma^{\pm} \to t_d(1-u_{33})\sigma^{\pm} - i\frac{\hbar v_F}{a}u_{31}s^y\sigma^z + i\frac{\hbar v_F}{a}u_{32}s^x\sigma^z \\ t_s \to t_s(1-u_{33}) \end{aligned}, \tag{3.12}$$

with the strain tensor $u_{ij} = \frac{1}{2}(\partial_i u_j + \partial_j u_i)$, where $u_j$ is the $j$-th component of the displacement vector $\boldsymbol{u}$. Under such hopping parameter substitution, the Hamiltonian in Eq. 3.3 is changed to

$$\tilde{\mathcal{H}}_{\boldsymbol{k}} = \mathcal{H}_{\boldsymbol{k}} + \delta\mathcal{H}_{\boldsymbol{k}}, \tag{3.13}$$

where the correction due to strain is

$$\begin{aligned} \delta\mathcal{H}_{\boldsymbol{k}} = -(t_s u_{33} + t_d u_{33}\cos k_z a)\sigma^x\tau^z - t_d u_{33}\sigma^y\tau^z \sin k_z a \\ - \frac{\hbar v_F}{a}u_{31}s^y\sigma^z\tau^z \sin k_z a + \frac{\hbar v_F}{a}u_{32}s^x\sigma^z \sin k_z a. \end{aligned} \tag{3.14}$$

To understand the effect of strain on the low-energy physics we consider $\tilde{\mathcal{H}}_{\boldsymbol{k}}$ in the vicinity of Weyl points $\boldsymbol{k}_W = (0, 0, \eta Q)$

$$\tilde{\mathcal{H}}_{\boldsymbol{k}_W+\boldsymbol{q}} = \mathcal{H}_{\boldsymbol{k}_W} + h_{\boldsymbol{q}} + \delta\mathcal{H}_{\boldsymbol{k}_W} + O(q^2) + O(q)Q(u_{ij}), \tag{3.15}$$

where the linearized Hamiltonian $h_{\boldsymbol{q}}$ reads

$$h_{\boldsymbol{q}} = \boldsymbol{q}\cdot\nabla_{\boldsymbol{k}}\mathcal{H}_{\boldsymbol{k}}|_{\boldsymbol{k}=\boldsymbol{k}_W} = -\hbar v_F q_x s^y\sigma^z\tau^z + \hbar v_F q_y s^x\sigma^z - \eta t_d q_z a\sin Qa\sigma^x\tau^z + t_d q_z a\cos Qa\sigma^y\tau^z. \quad (3.16)$$

And $\mathcal{H}_{\boldsymbol{k}_W}$ represents the Bloch Hamiltonian Eq. 3.3 at Weyl points. According to Eq. 3.4, $\mathcal{H}_{\boldsymbol{k}_W}$ has eigenvalues $\{2m, 2m, 0, 0, 0, 0, -2m, -2m\}$ and thus encodes both low-energy Weyl points and high-energy gapped sector. To extract the low-energy physics only, we assume real order parameter $\Delta\in\mathbb{R}$ and solve for the eigenstates of $\mathcal{H}_{\boldsymbol{k}_W}$ associated with Weyl points as

$$|\phi_1\rangle = \frac{1}{\sqrt{2}}\Big(\frac{z_1-iz_2}{m}, 0, -1, 0, 0, 0, 0, \frac{\Delta}{m}\Big)^T, \quad (3.17)$$

$$|\phi_2\rangle = \frac{1}{\sqrt{2}}\Big(-\frac{\Delta}{m}, 0, 0, 0, 0, 1, \frac{z_1+iz_2}{m}\Big)^T, \quad (3.18)$$

$$|\phi_3\rangle = \frac{1}{\sqrt{2}}\Big(0, \frac{-z_1+iz_2}{m}, 0, -1, 0, 0, \frac{\Delta}{m}, 0\Big)^T, \quad (3.19)$$

$$|\phi_4\rangle = \frac{1}{\sqrt{2}}\Big(0, -\frac{\Delta}{m}, 0, 0, 1, 0, \frac{-z_1-iz_2}{m}, 0\Big)^T. \quad (3.20)$$

where we have used following quantities

$$z_1 = t_s + t_d\cos k_z a, \quad (3.21)$$

$$z_2 = t_d\sin k_z a. \quad (3.22)$$

We then project $h_{\boldsymbol{q}}+\delta\mathcal{H}_{\boldsymbol{k}_W}$ onto the four-dimensional Hilbert space spanned by $|\phi_{i=1,2,3,4}\rangle$. We get

$$(h_{\boldsymbol{q}}+\delta\mathcal{H}_{\boldsymbol{k}_W})_\phi = \begin{pmatrix} -\frac{z_1\tilde{z}_1+z_2\tilde{z}_2}{m} & 0 & -i\tilde{x}-\tilde{y} & 0 \\ 0 & -\frac{z_1\tilde{z}_1+z_2\tilde{z}_2}{m} & 0 & i\tilde{x}+\tilde{y} \\ i\tilde{x}-\tilde{y} & 0 & \frac{z_1\tilde{z}_1+z_2\tilde{z}_2}{m} & 0 \\ 0 & -i\tilde{x}+\tilde{y} & 0 & \frac{z_1\tilde{z}_1+z_2\tilde{z}_2}{m} \end{pmatrix}, \quad (3.23)$$

where, to keep our derivation transparent, we further defined the following quantities

$$\tilde{x} = \frac{\hbar v_F}{a}(q_x a + \eta u_{31}\sin Qa), \quad (3.24)$$

$$\tilde{y} = \frac{\hbar v_F}{a}(q_y a + \eta u_{32}\sin Qa), \quad (3.25)$$

$$\tilde{z}_1 = -\eta t_d\sin Qa\Big(q_z a + \eta u_{33}\frac{t_s+t_d\cos Qa}{t_d\sin Qa}\Big), \quad (3.26)$$

$$\tilde{z}_2 = t_d\cos Qa(q_z a - \eta u_{33}\tan Qa). \quad (3.27)$$

The projected $4\times 4$ matrix Hamiltonian can be written in terms of standard Dirac matrices which we express as a tensor product of Pauli matrices $\alpha$ and $\beta$ as

$$\begin{aligned}(h_{\boldsymbol{q}}+\delta\mathcal{H}_{\boldsymbol{k}_W})_\phi = &\frac{\hbar v_F}{a}(q_x a+\eta u_{31}\sin Qa)\alpha^z\beta^y \\ &-\frac{\hbar v_F}{a}(q_y a+\eta u_{32}\sin Qa)\alpha^z\beta^x \\ &+\frac{\eta t_s t_d \sin aQ}{m}\left(q_z a+\eta u_{33}\frac{m^2-\Delta^2}{t_s t_d\sin aQ}\right)\beta^z. \end{aligned} \tag{3.28}$$

From here, one can read off the strain-induced gauge field

$$\mathcal{A}=\frac{\eta\hbar}{ea}\left(u_{31}\sin Qa, u_{32}\sin Qa, u_{33}\frac{m^2-\Delta^2}{t_s t_d\sin Qa}\right). \tag{3.29}$$

Clearly, the vector $\mathcal{A}$ can be understood as the gauge potential of a strain-induced chiral magnetic field. In most cases we expect $Qa \ll 1$. In this limit the $z$ component of $\mathcal{A}$ given in Eq. 3.29 scales as $1/aQ$ but $x(y)$ components scale as $aQ$. Thus only $\mathcal{A}_z \propto u_{33}$ will be considered in the following.

According to Fig. 3.1, we may characterize the bend deformation by an small angle $\theta = a/\rho$ where $\rho$ is the radius associated with the circular bend. The lattice constant of the outermost $y$ direction layer is then $a+\delta a$ with $\delta a = \frac{1}{2}\bar{l}_y a\theta$. Here $\bar{l}_y$ is the number of layers in $y$ direction. Thus

$$\rho=\frac{\bar{l}_y a}{2\delta a/a}=\frac{\bar{l}_y a}{\varepsilon}, \tag{3.30}$$

with $\varepsilon = 2\delta a/a$ being the bending parameter used in the numerics. Now if we consider a generic $y$ direction layer, its lattice constant will change by $\delta a(y) = (y-\bar{l}_y a/2)\theta$. Then for a point with coordinate $z$ on this layer, its $z$ direction displacement is $u_3 = \frac{z}{a}(y-\bar{l}_y a/2)\frac{2\delta a}{\bar{l}_y a}$. Thus,

$$u_{33}=\frac{\partial u_3}{\partial z}=(y-\bar{l}_y a/2)\frac{2\delta a}{a^2\bar{l}_y}=(y-\bar{l}_y a/2)\frac{\varepsilon}{\bar{l}_y a}. \tag{3.31}$$

Therefore, we expect a pseudo-magnetic field[7]

$$\boldsymbol{b}=\partial_y\mathcal{A}_z\hat{x}=\eta\frac{\hbar}{ea^2}\frac{m^2-|\Delta|^2}{t_s t_d\sin Qa}\frac{\varepsilon}{\bar{l}_y}\hat{x}. \tag{3.32}$$

[7]Unlike the applied external magnetic field $\boldsymbol{B}$, which can either be expelled from the superconductor bulk by the formation of surface currents (i.e., Meissner effect) or brought into the superconductor bulk by the formation of supercurrent vortices, the pseudo-magnetic field $\boldsymbol{b}$ couples to Weyl cones deep in the superconductor bulk and vanishes outside the superconductor. It may be interpreted as a modular field [138] that can neither propagate nor be screened.

According to Eq. 1.14, such pseudo-magnetic field will give rise to Dirac-Landau levels at energies

$$\tilde{\epsilon}_n(\boldsymbol{k}) = \pm\sqrt{\hbar^2 v_x^2 k_x^2 + 2n\left|\frac{eb}{\hbar}\hbar v_y \hbar v_z\right|}, \tag{3.33}$$

for all integers $n \neq 0$ and $\tilde{\epsilon}_0(k_x) = -\hbar v_F k_x$ as the zeroth Landau levels for both valleys. In view of Eq. 3.32, we get

$$\tilde{\epsilon}_n(\boldsymbol{k}) = \pm\sqrt{\hbar^2 v_x^2 k_x^2 + 2n\frac{\varepsilon}{\bar{l}_y}\frac{m^2 - |\Delta|^2}{m}\frac{\hbar v_y}{a}}. \tag{3.34}$$

We have numerically checked Eq. 3.34 by applying hopping substitutions Eq. 3.12 in the multilayer Hamiltonian Eq. 3.1 with $\bar{l}_y = 150$, as summarized in Fig. 3.5(b). Indeed we observe that the Dirac-Landau levels in Eq. 3.33 capture the features of the low-energy spectrum of the Weyl superconductor multilayer. For comparison we also plot the spectrum and DOS for the unstrained system and show the results in Fig. 3.5(a,c).

For the sake of completeness we in addition calculate the spectrum of our model Weyl superconductor in the presence of the magnetic field $\mathbf{B} \parallel \hat{z}$ and the Abrikosov vortex lattice. This is summarized in Appendix B. We find that all bands become completely flat Landau levels in the $x$-$y$ plane. The zeroth Landau level, which is associated with Weyl nodes before $\mathbf{B}$ is switched on, is still linearly dispersive along the $z$-direction in the vicinity of nodes. In contrast, it is well known that the magnetic field does not lead to flat Landau levels in $d_{x^2-y^2}$ superconductors. This is because the spatially varying supercurrent in the vortex lattice strongly scatters the Bogoliubov quasiparticles [131]. The difference between the $d_{x^2-y^2}$ and 3D Weyl superconductors has been recently elucidated in Ref. [139] with which our results are in accord. In short, the zeroth Landau level cannot be scattered by vortices due to the protection of Weyl node chirality, which is a topologically nontrivial and unique feature of the Weyl superconductor.

## 3.3 Weyl superconductors with chemical potential

In Section 3.2, we found that a bend deformation results in Dirac-Landau levels of Bogoliubov quasiparticles, which unlike those in Weyl semimetals, are charge neutral on average. Therefore, the Shubnikov-de Haas quantum oscillation discussed in Section 2.4 cannot be observed in Weyl superconductors. But Bogoliubov quasiparticles do carry heat, making thermal transport measurements, such as the thermal Hall effect, possible [140–142].

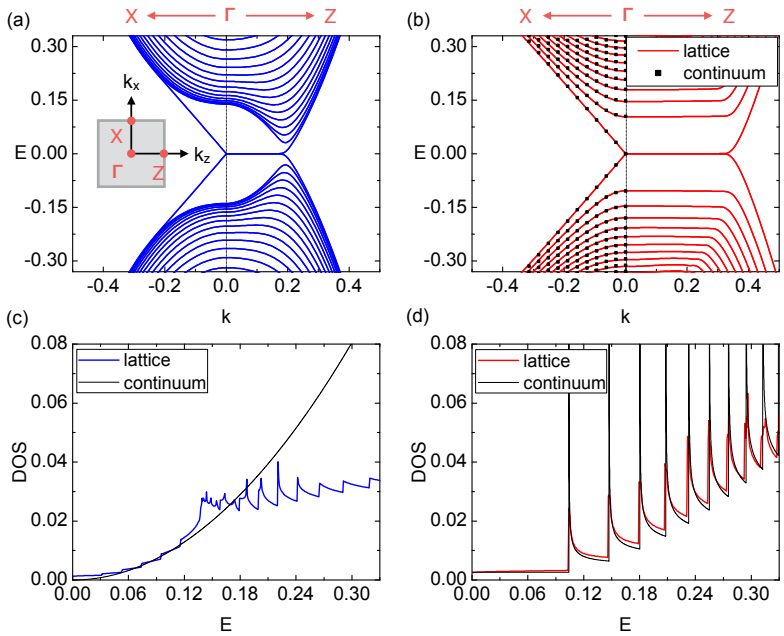


Figure 3.5: Energy spectra and DOS for our Weyl superconductor with open boundaries and $\bar{l}_y = 150$ along the $y$ direction and periodic along $x$ and $z$. (a) The spectrum of undeformed system; the flat band at zero energy is the Fermi arc. (b) The spectrum of a bent Weyl superconductor as shown in Fig. 3.1(b) with $\varepsilon = 8\%$ corresponding to a pseudo-magnetic field $b = 10.45$T. For both (a) and (b) the spectrum is plotted along $X$-$\Gamma$-$Z$ as shown in the inset. For comparison, energy levels of Eq. 3.34 are overlain as black dots. (c) DOS of the unstrained sample (blue curve) compared to the ideal $\sim E^2$ DOS expected for a massless Dirac fermion in continuum (black parabola). (d) DOS of the strained system (red curve) compared to DOS calculated for ideal Dirac-Landau levels with $b = 10.45$T.

Our concern will be calculating the thermal conductivity quantum oscillation of Weyl superconductors. However, in our analysis above, the chemical potential $\mu$ of TI layers was assumed to lie at the Weyl points ($\mu = 0$) and the Fermi surface is then comprised of two separate points carrying vanishing quasiparticle DOS. According to Lifshitz-Onsager relation [112], the associated quantum oscillation has infinite period thus cannot be observed. In this section, we will attack this difficulty by tuning $\mu$ away from Weyl points. We will show that this results in a finite size Fermi surface compatible to the

thermal conductivity quantum oscillation.

Away from Weyl points, we have nonzero chemical potential $\mu \neq 0$ and Eq. 3.3 will be modified by an extra term $\delta\mathcal{H}_{\boldsymbol{k}} = -\mu\tau^z$. The modified Hamiltonian is then

$$\mathcal{H}_{\boldsymbol{k}} - \mu\tau^z = H_0 + V, \tag{3.35}$$

where

$$H_0 = m_0 s^z\tau^z + z_1\sigma^x\tau^z + z_2\sigma^y\tau^z - \Delta s^y\tau^y, \tag{3.36}$$

$$V = -\mu\tau^z + y s^x\sigma^z - x s^y\sigma^z\tau^z. \tag{3.37}$$

Again, for simplicity we assume real $\Delta$ and define the following quantities

$$m_0 = m - 4m' + 2m'\cos k_x a + 2m'\cos k_y a, \tag{3.38}$$

$$x = \frac{\hbar v_F}{a}\sin k_x, \tag{3.39}$$

$$y = \frac{\hbar v_F}{a}\sin k_y. \tag{3.40}$$

Based on the parameter values we have chosen, $\Delta$ is of the same order as $z_2$, but is one order of magnitude smaller than $z_1$ and $m_0$. We set chemical potential $\mu$ to be an order of magnitude smaller than $\Delta$. Also note that in the vicinity of Weyl points, both $x$ and $y$ are sufficiently small. Therefore, we may treat $V$ as a perturbation to $H_0$, whose low-energy eigenvectors can be easily resolved as

$$|\phi_{D_1,1}\rangle = \frac{1}{\sqrt{2}}\Big(\frac{z_1 - iz_2}{\sqrt{z_1^2+z_2^2+\Delta^2}}, 0, -1, 0, 0, 0, 0, \frac{\Delta}{\sqrt{z_1^2+z_2^2+\Delta^2}}\Big)^T, \tag{3.41}$$

$$|\phi_{D_1,2}\rangle = \frac{1}{\sqrt{2}}\Big(\frac{-\Delta}{\sqrt{z_1^2+z_2^2+\Delta^2}}, 0, 0, 0, 0, 1, 0, \frac{z_1 + iz_2}{\sqrt{z_1^2+z_2^2+\Delta^2}}\Big)^T, \tag{3.42}$$

$$|\phi_{D_2,1}\rangle = \frac{1}{\sqrt{2}}\Big(0, \frac{-z_1 + iz_2}{\sqrt{z_1^2+z_2^2+\Delta^2}}, 0, -1, 0, 0, \frac{\Delta}{\sqrt{z_1^2+z_2^2+\Delta^2}}, 0\Big)^T, \tag{3.43}$$

$$|\phi_{D_2,2}\rangle = \frac{1}{\sqrt{2}}\Big(0, \frac{-\Delta}{\sqrt{z_1^2+z_2^2+\Delta^2}}, 0, 0, 1, 0, \frac{-z_1 - iz_2}{\sqrt{z_1^2+z_2^2+\Delta^2}}, 0\Big)^T. \tag{3.44}$$

These correspond to the degenerate subspace $D_1$ with eigenvalue

$$E^{(0)}_{D_1,1(2)} = m_0 - \sqrt{z_1^2+z_2^2+\Delta^2}, \tag{3.45}$$

and $D_2$ with eigenvalue

$$E^{(0)}_{D_2,1(2)} = \sqrt{z_1^2+z_2^2+\Delta^2} - m_0. \tag{3.46}$$

We then project the perturbation $V$ to the degenerate subspaces $D_1$ and $D_2$, respectively. In a compact form, it reads

$$V_{D_i} = \begin{pmatrix} \langle \phi_{D_i,1}|V|\phi_{D_i,1}\rangle & \langle \phi_{D_i,1}|V|\phi_{D_i,2}\rangle \\ \langle \phi_{D_i,2}|V|\phi_{D_i,1}\rangle & \langle \phi_{D_i,2}|V|\phi_{D_i,2}\rangle \end{pmatrix}, \tag{3.47}$$

where $i = 1, 2$. Individually, we can write $V_{D_i}$ in terms of the Pauli matrix $\boldsymbol{\nu}$

$$\begin{aligned} V_{D_1} &= d_x\nu^x + d_y\nu^y + d_z\nu^z, \\ V_{D_2} &= -d_x\nu^x - d_y\nu^y + d_z\nu^z, \end{aligned} \tag{3.48}$$

where

$$d_x = \frac{z_1\Delta}{z_1^2 + z_2^2 + \Delta^2}\mu, \tag{3.49}$$

$$d_y = -\frac{z_2\Delta}{z_1^2 + z_2^2 + \Delta^2}\mu, \tag{3.50}$$

$$d_z = -\frac{z_1^2 + z_2^2}{z_1^2 + z_2^2 + \Delta^2}\mu. \tag{3.51}$$

Matrices $V_{D_1}$ and $V_{D_2}$ can be diagonalized through unitary transformations

$$U_{D_i}^{-1} V_{D_i} U_{D_i} = \mathrm{diag}(d, -d) \qquad i = 1, 2, \tag{3.52}$$

where

$$d = \sqrt{\frac{z_1^2 + z_2^2}{z_1^2 + z_2^2 + \Delta^2}}\mu \approx \mu, \tag{3.53}$$

because for our purpose $\Delta^2 \ll z_1^2 + z_2^2$. The transformation matrices are

$$U_{D_1} = \begin{pmatrix} \sqrt{\frac{d+d_z}{2d}}\frac{d_x - id_y}{\sqrt{d_x^2+d_y^2}} & -\sqrt{\frac{d-d_z}{2d}} \\ \sqrt{\frac{d-d_z}{2d}} & \sqrt{\frac{d+d_z}{2d}}\frac{d_x + id_y}{\sqrt{d_x^2+d_y^2}} \end{pmatrix}, \tag{3.54}$$

$$U_{D_2} = \begin{pmatrix} \sqrt{\frac{d+d_z}{2d}}\frac{-d_x + id_y}{\sqrt{d_x^2+d_y^2}} & -\sqrt{\frac{d-d_z}{2d}} \\ \sqrt{\frac{d-d_z}{2d}} & \sqrt{\frac{d+d_z}{2d}}\frac{-d_x - id_y}{\sqrt{d_x^2+d_y^2}} \end{pmatrix}. \tag{3.55}$$

We can immediately write down the first order correction to energy

$$E^{(1)}_{D_1,1(2)} = E^{(1)}_{D_2,1(2)} = \pm d \approx \pm\mu. \tag{3.56}$$

Because the 2-fold degeneracy is lifted, the zeroth order eigenvectors are now uniquely determined

$$(|\tilde{\phi}_{D_1,1}\rangle, |\tilde{\phi}_{D_1,2}\rangle) = (|\phi_{D_1,1}\rangle, |\phi_{D_1,2}\rangle)U_{D_1}, \tag{3.57}$$

$$(|\tilde{\phi}_{D_2,1}\rangle, |\tilde{\phi}_{D_2,2}\rangle) = (|\phi_{D_2,1}\rangle, |\phi_{D_2,2}\rangle)U_{D_2}. \tag{3.58}$$

We may now calculate the second order correction to the energy

$$E^{(2)}_{D_1,1(2)} = \sum_{\alpha\in D_2} \frac{|\langle\tilde{\phi}_\alpha|V|\tilde{\phi}_{D_1,1(2)}\rangle|^2}{E_{D_1}-E_\alpha} = \frac{x^2+y^2}{2(m_0-\sqrt{z_1^2+z_2^2+\Delta^2})}, \tag{3.59}$$

$$E^{(2)}_{D_2,1(2)} = \sum_{\alpha\in D_1} \frac{|\langle\tilde{\phi}_\alpha|V|\tilde{\phi}_{D_2,1(2)}\rangle|^2}{E_{D_2}-E_\alpha} = -\frac{x^2+y^2}{2(m_0-\sqrt{z_1^2+z_2^2+\Delta^2})}, \tag{3.60}$$

where we ignore the contribution from high-energy sector, if any. This is because for high energies $E_\alpha = \pm(m_0+\sqrt{z_1^2+z_2^2+\Delta^2})$ the denominator in the second order correction is either $\pm 2m_0$ or $\pm 2\sqrt{z_1^2+z_2^2+\Delta^2}$, whose magnitude is much larger than that of $\pm 2(m_0-\sqrt{z_1^2+z_2^2+\Delta^2})$ and thus are less important. Combining all the corrections, we can estimate the quasiparticle energy at nozero $\mu$ as

$$E_{D_1,1(2)} \approx \sqrt{x^2+y^2+(m_0-\sqrt{z_1^2+z_2^2+\Delta^2})^2} \pm \mu, \tag{3.61}$$

$$E_{D_2,1(2)} \approx -\sqrt{x^2+y^2+(m_0-\sqrt{z_1^2+z_2^2+\Delta^2})^2} \pm \mu. \tag{3.62}$$

We observe that to the leading order the spectrum of Weyl superconductor multilayer is now biased. The original 2-fold degeneracy in Eq. 3.4 has been lifted. One copy of the spectrum moves up while the other copy moves down. As a result, the strain-induced pseudo-Landau levels will also be biased as

$$E_n(\boldsymbol{k}) = \pm\sqrt{\hbar^2 v_x^2 k_x^2 + 2n\left|\frac{eb}{\hbar}\hbar v_y \hbar v_z\right|} \pm \mu, \tag{3.63}$$

as illustrated in Fig. 3.6(b). The corresponding DOS at the chemical potential is

$$\begin{aligned} D(0) &= \frac{L_y L_z}{2\pi l_b^2}\sum_n L_x \sum_\pm \int \frac{dk_x}{2\pi}\delta(E_n(\boldsymbol{k})) \\ &= \frac{V}{2\pi l_b^2}\frac{1}{\pi\hbar v_x}\sum_n \sqrt{\frac{\mu^2}{\mu^2 - 2n|\frac{eb}{\hbar}\hbar v_y \hbar v_z|}}, \end{aligned} \tag{3.64}$$

where $l_b = \sqrt{\hbar/eb}$ is the magnetic length. It can be easily seen from Eq. 3.64 that when $\mu \neq 0$, the $D(0)$ exhibits oscillating behavior when pseudo-magnetic field $b$ scans. Therefore, the thermal conductivity will also oscillate because the number of heat carriers varies periodically with respect to $1/b$.

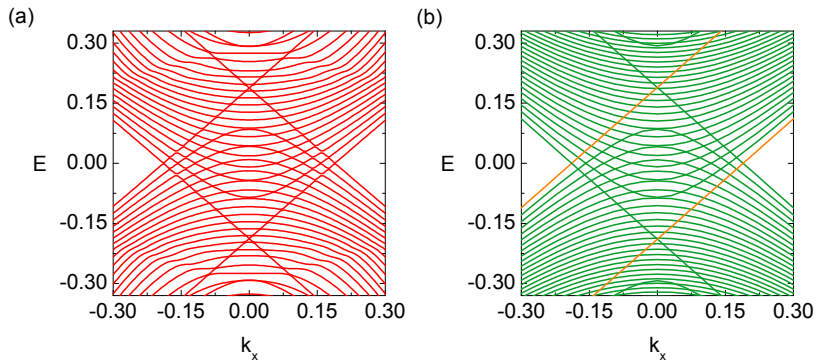


Figure 3.6: Energy spectrum of the Weyl superconductor with the chemical potential of the TI layers tuned away from the surface Dirac points to $\mu = 0.19$. (a) Quasiparticle spectrum calculated from the lattice model Eq. 3.13. It is worth noting that only the left moving chiral mode is due to the Landau quantization while the other is a surface mode. (b) Quasiparticle spectrum predicted by Eq. 3.63. To compare with the first panel, the chiral modes (orange lines) due to the surface states have been added manually.

## 3.4 Longitudinal thermal conductivity

In Section 3.3, we have justified that the needed nonzero Fermi surface for the observation of QOs can be obtained by tuning the chemical potential $\mu$ away from the Weyl points. In this section, we derive the quantum oscillation of longitudinal thermal conductivity $\kappa_{xx}$.

We compute the thermal conductivity using the Boltzmann equation approach [143–145] and it reads

$$\boldsymbol{\kappa} = \frac{1}{T}\sum_n \sum_{\boldsymbol{k}} E_n^2(\boldsymbol{k})\tau_n(E_n(\boldsymbol{k}))\boldsymbol{v}_n(\boldsymbol{k})\boldsymbol{v}_n(\boldsymbol{k})\left(-\frac{\partial f}{\partial E_n}\right), \tag{3.65}$$

where $E_n(\boldsymbol{k})$ is the quasiparticle energy given by Eq. 3.63, $\boldsymbol{v}_n(\boldsymbol{k}) = \frac{1}{\hbar}\nabla_{\boldsymbol{k}} E_n(\boldsymbol{k})$ is the associated velocity, $\tau_n(\boldsymbol{k})$ is the corresponding scattering time, and

$f(E_n) = (e^{E_n/k_BT} + 1)^{-1}$ is Fermi-Dirac distribution function. For our purposes, it is useful to rewrite the thermal conductivity (Eq. 3.65) in the low-$T$ limit. To achieve this, we first introduce the auxiliary tensor

$$\boldsymbol{\sigma}(\epsilon) = \sum_n \sum_{\boldsymbol{k}} \tau_n(E_n(\boldsymbol{k}))\delta(\epsilon - E_n(\boldsymbol{k}))\boldsymbol{v}_n(\boldsymbol{k})\boldsymbol{v}_n(\boldsymbol{k}), \tag{3.66}$$

which may be understood as a thermal analogue of the usual conductivity tensor. It is easy to see that

$$\boldsymbol{\kappa} = \frac{1}{T}\int_{-\infty}^{+\infty} d\epsilon \epsilon^2 \boldsymbol{\sigma}(\epsilon)\Big(-\frac{\partial f}{\partial \epsilon}\Big). \tag{3.67}$$

We further define an auxiliary function

$$K(\epsilon) = \epsilon^2 \boldsymbol{\sigma}(\epsilon), \tag{3.68}$$

through which the thermal conductivity can be written as

$$\boldsymbol{\kappa} = \frac{1}{T}\int_{-\infty}^{+\infty} d\epsilon \sum_{s=1}^{\infty} \frac{1}{s!}\frac{d^s K}{d\epsilon^s}\bigg|_0 \epsilon^s \Big(-\frac{\partial f}{\partial \epsilon}\Big). \tag{3.69}$$

Note that $\frac{\partial f}{\partial \epsilon}$ is an even function of $\epsilon$. Therefore, we only need to consider even $s$. The thermal conductivity is further simplified as

$$\boldsymbol{\kappa} = \frac{1}{T}\sum_{s=1}^{\infty}\int_{-\infty}^{+\infty} d\epsilon \frac{(k_BT)^{2s}}{(2s)!}\Big(\frac{\epsilon}{k_BT}\Big)^{2s}\Big(-\frac{\partial f}{\partial \epsilon}\Big)\frac{d^{2s}K}{d\epsilon^{2s}}\bigg|_0. \tag{3.70}$$

Define $x = \frac{\epsilon}{k_BT}$ and

$$\begin{aligned} a_s = \int_{-\infty}^{+\infty} dx \frac{x^{2s}}{(2s)!}\Big(-\frac{d}{dx}\frac{1}{e^x+1}\Big) &= \frac{2}{\Gamma(2s)}\int_0^{+\infty} dx \frac{x^{2s-1}}{e^x+1} \\ &= 2\eta(2s) = 2(1-2^{1-2s})\zeta(2s), \end{aligned} \tag{3.71}$$

where $\Gamma(s) = \int_0^{+\infty} dx \frac{x^{s-1}}{e^x}$, $\eta(s) = \int_0^{+\infty} dx \frac{x^{s-1}}{e^x+1}$, and $\zeta(s) = \int_0^{+\infty} dx \frac{x^{s-1}}{e^x-1}$ are Gamma function, Dirichlet eta function, and Riemann zeta function, respectively. The thermal conductivity now reads

$$\boldsymbol{\kappa} = \frac{1}{T}\sum_{s=1}^{\infty} 2(1-2^{1-2s})\zeta(2s)\frac{d^{2s}K}{d\epsilon^{2s}}\bigg|_0 (k_BT)^{2s}. \tag{3.72}$$

For low temperatures $k_BT \ll \mu$, we keep only the $s = 1$ term and use $\zeta(2) = \frac{\pi^2}{6}$ to get

$$\boldsymbol{\kappa} = \frac{1}{T}\frac{\pi^2 k_B^2 T^2}{3}\boldsymbol{\sigma}(0) = \frac{\pi^2 k_B^2 T}{3}\sum_n\sum_{\boldsymbol{k}}\tau_n(E_n(\boldsymbol{k}))\delta(E_n(\boldsymbol{k}))\boldsymbol{v}_n(\boldsymbol{k})\boldsymbol{v}_n(\boldsymbol{k}). \tag{3.73}$$

This relation can be regarded as the Wiedemann-Franz law for Bogoliubov quasiparticles. By comparing to Eq. 2.26, we obtain the longitudinal thermal conductivity

$$\kappa_{xx} = \frac{\pi^2 k_B^2 T}{3}\frac{v_x}{\pi\hbar}\frac{L_y L_z}{2\pi l_b^2}L_x\sum_n\tau_n(0)\sqrt{\frac{\mu^2 - 2n|\frac{eb}{\hbar}\hbar v_y \hbar v_z|}{\mu^2}}. \tag{3.74}$$

The scattering time can be determined by Fermi's golden rule

$$\frac{1}{\tau_n(E_n(\boldsymbol{k}))} = \frac{2\pi}{\hbar}\sum_{n'}\sum_{\boldsymbol{k}'}|\langle n'\boldsymbol{k}'|V(\boldsymbol{r})_{\text{imp}}\tau^z|n\boldsymbol{k}\rangle|^2\delta(E_n(\boldsymbol{k}) - E_{n'}(\boldsymbol{k}')), \tag{3.75}$$

where $|n\boldsymbol{k}\rangle$ is the eigenvector of chemical potential biased Weyl superconductor under strain, characterized by the Hamiltonian $H - \mu\tau^z$. As discussed in Section 3.3, when $\mu^2 \ll \Delta^2 \ll t_s^2 + t_d^2 + 2t_s t_d \cos k_z a$, we can use perturbative calculation to write down the Schrödinger equations for Weyl superconductor with TI layer chemical potential $\mu \neq 0$ and $\mu = 0$, respectively, as

$$(H - \mu\tau^z)|n\boldsymbol{k}^0\rangle \approx \tilde{\epsilon}_n(\boldsymbol{k})|n\boldsymbol{k}^0\rangle \pm \mu|n\boldsymbol{k}^0\rangle, \tag{3.76}$$

$$H|n\boldsymbol{k}^0\rangle = \tilde{\epsilon}_n(\boldsymbol{k})|n\boldsymbol{k}^0\rangle, \tag{3.77}$$

where $\tilde{\epsilon}_n(\boldsymbol{k})$ is determined by Eq. 3.34 and $|n\boldsymbol{k}^0\rangle$ is the exact eigenvector of $H$ and the zeroth order eigenvector of $H - \mu\tau^z$. If apply $\langle n'\boldsymbol{k}'^0|$ to Eq. 3.76 and Eq. 3.77 and subtract, we get

$$\langle n'\boldsymbol{k}'^0|\tau^z|n\boldsymbol{k}^0\rangle \approx \pm\langle n'\boldsymbol{k}'^0|n\boldsymbol{k}^0\rangle, \tag{3.78}$$

then we can approximate $\tau_n(E_n(\boldsymbol{k}))$ by

$$\frac{1}{\tau_n(E_n(\boldsymbol{k}))} \approx \frac{2\pi}{\hbar}\sum_{n'}\sum_{\boldsymbol{k}'}|\langle n'\boldsymbol{k}'^0|V(\boldsymbol{r})_{\text{imp}}|n\boldsymbol{k}^0\rangle|^2 \times \delta(E_n(\boldsymbol{k}) - E_{n'}(\boldsymbol{k}')). \tag{3.79}$$

The righthand side is the same as the scattering rate of a Weyl semimetal [134] with electronic structure characterized by $E_n(\boldsymbol{k})$. Therefore, the scattering rate in a Weyl superconductor should also be the same, which leads to

$$\tau_n^{-1}(0) = \frac{2\pi}{\hbar}n_{\text{imp}}C_{\text{imp}}D(0), \tag{3.80}$$

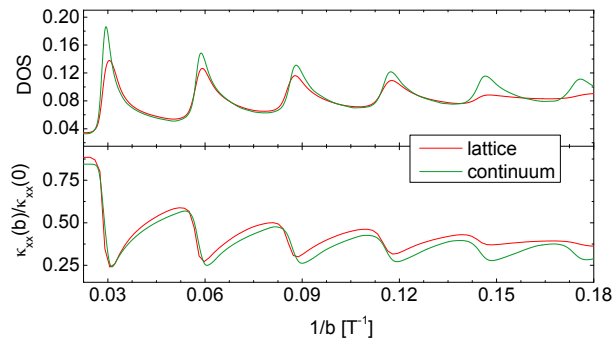


Figure 3.7: Strain-induced quantum oscillation in a Weyl superconductor. The upper panel shows oscillations in DOS as a function of inverse strain strength expressed as $1/b$ at zero-energy. The lower panel shows oscillations in the longitudinal quasiparticle thermal conductivity $\kappa_{xx}$. To simulate the effect of disorder, all data are broadened by convolving in energy with a Lorentzian with width $\delta_\epsilon = 1.67 \times 10^{-3}$.

where $n_{\text{imp}}$ and $C_{\text{imp}}$ denote the impurity concentration and the scattering potential strength, respectively. The longitudinal thermal conductivity then becomes

$$\kappa_{xx}(b) = \kappa_{xx}(0) \frac{\sum_n \sqrt{\frac{\mu^2 - 2n|\frac{eb}{\hbar}\hbar v_y \hbar v_z|}{\mu^2}}}{\sum_n \sqrt{\frac{\mu^2}{\mu^2 - 2n|\frac{eb}{\hbar}\hbar v_y \hbar v_z|}}}, \tag{3.81}$$

with the zero-field thermal conductivity

$$\kappa_{xx}(0) = \frac{\pi^2 k_B^2 T}{3} \frac{v_x^2}{\frac{2\pi}{\hbar} n_{\text{imp}} C_{\text{imp}}}. \tag{3.82}$$

Fig. 3.7 shows our results for DOS and $\kappa_{xx}(b)$ calculated from the approximate analytical formulas Eqs. 3.64 and 3.81, and based on the full lattice calculation using Eqs. 3.64 and 3.73 with the assistance of the tetrahedron method (Appendix F). They agree well and exhibit pronounced quantum oscillations periodic in $1/b$.

We note that due to Landau quantization, quantum oscillations in the $x$ direction are most pronounced, while in the other directions, quantum oscillations are expected to be weaker. Based on our results for the electronic structure in Fig. 3.5(b), the $z$ direction drift velocity of Bogoliubov quasiparticles is nonzero only at the edges of bands ($k_z a \sim 0.3$). In contrast,

the $x$ direction drift velocity is nonzero for almost all momenta. Therefore, $\kappa_{zz}$ should be small and its quantum oscillation is weaker than that in $\kappa_{xx}$. In y-direction, quasi-particle wave functions are Gaussian-localized with the characteristic decay length $\sqrt{\hbar v_y/ebv_z} \sim l_B$ and localization centers $2\pi\nu l_B^2/L_z$ with $\nu = 1, 2, \cdots, L_z/a$. The localization makes transport difficult unless the localization center is pumped across the system when $b$ varies. Therefore, we do not expect pronounced quantum oscillations along the $y$-direction.

It is also worth noting that quasiparticle thermal conductivity can be obscured in real materials by phonons because phonons also carry heat. For temperature $T \ll T_c$, the thermal conductivity of acoustic phonons follows Debye $T^3$ law $\kappa_{ph}^A \sim T^3$. The less dominant optical phonon thermal conductivity is $\kappa_{ph}^O \sim \frac{1}{T^2}\exp(-\frac{1}{T})$. At low temperatures both will be overwhelmed by quasiparticle contribution. At higher temperatures, the phonon contribution $\kappa_{ph} = \kappa_{ph}^A + \kappa_{ph}^O$ can dominate over the quasiparticle thermal conductivity but quantum oscillations should remain visible, because $\kappa_{ph}$ does not show quantum oscillations due to the bosonic nature of phonons.

## 3.5 Summary

In this chapter, we studied a minimal model for a Weyl superconductor with a single pair of Weyl points based on the Meng-Balents multilayer construction. A Majorana-Fermi arc appears and connects the two Weyl points if a pair of boundaries are open. This arc can be understood as being formed of two counter propagating chiral Majorana modes at the edge of an effective topological $p_x + ip_y$ SC that results from fixing one component of the momentum in the 3D Hamiltonian describing the original Weyl SC. The phase diagram shows that the Weyl SC phase appears intermediately between a fully gapped trivially superconducting phase and a topologically superconducting phase. These features elucidate similarities between Weyl superconductors and Weyl semimetals.

In the low-energy sector of the theory, we showed that elastic strain acts as a chiral gauge potential incorporated in the Weyl Hamiltonian through the standard minimal substitution. Therefore, strain can mimic the effect of real physical magnetic field in the Weyl superconductor. One important difference is that the strain-induced pseudo-magnetic field is not subject to the Meisner effect. Remarkably, this fact allows the pseudo-magnetic field to Landau quantize the spectrum of Bogoliubov quasiparticles instead of being expelled from the sample or creating Abrikosov vortices as would be the case

for physical magnetic field $B$.

Landau quantization generates pronounced quantum oscillations that can be observed by quasiparticle spectroscopy and by longitudinal thermal conductivity. These quantum oscillations occur deep in the superconducting state and are thus fundamentally different from various theoretical proposals and experimental results that pertain to mixed and normal states of superconductors.

To experimentally test our proposal, we require a Weyl superconductor. Such can be in principle artificially engineered through the Meng-Balents construction or can occur naturally in a suitable crystalline solid. Currently, there are roughly twenty different nodal superconductors known to science [74]. One of the most promising candidates may be $Cu_xBi_2Se_3$ [19, 75]. Nuclear magnetic resonance experiments [77] revealed broken spin rotational symmetry in $Cu_xBi_2Se_3$, suggesting the superconducting gap structure to be either $\Delta_{4x}$ where the nodes appear due to the protection of mirror symmetry or $\Delta_{4y}$ where small gaps (or nodes) are expected. Recent experimental results on the specific heat [78] of $Cu_xBi_2Se_3$ are consistent with nematic superconductivity and favor $\Delta_{4y}$ pairing structure. Unfortunately, the gap minima and nodes cannot be straightforwardly differentiated based on the reported specific heat data alone. However, symmetry and energetic considerations [79, 80] suggest gap minima in nematic superconductivity. Another promising candidate is $Nb_xBi_2Se_3$, whose low temperature penetration depth exhibits quadratic temperature dependence characteristic of linearly dispersing point nodes in three dimensions [76]. This is consistent with $Nb_xBi_2Se_3$ being a Weyl superconductor. Although it is too early to draw a firm conclusion regarding the pairing state of the candidate materials, the existing experimental data give hope that $Cu_xBi_2Se_3$ and $Nb_xBi_2Se_3$ could eventually be identified as 3D Dirac or Weyl superconductors.

The second requirement is that the candidate material should be sufficiently flexible to allow a few percent elastic deformation in order to generate a sufficiently strong pseudo-magnetic field. The candidate material should be prepared in a nanoscale thin film geometry in order to maximize its flexibility. To the best of our knowledge, detailed data on the mechanical properties of $Cu_xBi_2Se_3$ is lacking and further experimental work is needed to determine whether or not this could be a suitable material.

There are several future directions that might be interesting to pursue based on our current work. The first is to test other properties associated with pseudo-Landau levels. Recent work on the fractional Josephson effect in strained 2D graphene superconductor [146] motivates the interest in studying a similar effect in one dimension higher using strained Weyl superconductor.

The second lies in the study of the chiral anomaly, chiral magnetic effect, and gravitational anomaly with strain-induced gauge field.

# Chapter 4

# Magnon quantum anomalies in Weyl ferromagnets

A magnon is a bosonic collective excitation of electron spins on a crystal lattice, carrying spin, magnetic dipole moment, and heat [82]. It can be quantum-mechanically characterized by a quantized spin wave [147] and experimentally detected by neutron scattering [148]. Though charge neutral, a magnon can be manipulated by electric fields and magnetic fields through the Aharonov-Casher effect [83] and the Zeeman effect, respectively. Due to their unique reaction to electromagnetic (EM) fields, magnons stand out from other bosons (photons, phonons, polarons, etc.) but are akin to electrons. Consequently, magnons are proposed to mimic some electronic transport properties such as the chiral anomaly [20, 25], the magnon Josephson effect [149], the spin Hall effect [26], the Wiedemann-Franz law [150, 151], the thermal Hall effect [152–157], the spin Seebeck effect [158–162], the spin Peltier effect [163, 164], and the spin Nernst effect [165–168].

On the other hand, electronic transport does not necessarily require the participation of EM fields or temperature gradients. One example is that relativistic electrons can be manipulated by elastic strains. As we have seen in Chapter 2, a properly designed strain can induce Landau levels in the absence of magnetic field and gives rise to quantum oscillations. In Chapter 3, we have showed that strain can manipulate *charge neutral* relativistic Bogoliubov quasiparticles, resulting in the Wiedemann-Franz law and quantum oscillations. These discoveries shed new light on novel magnon transport with only electric (magnetic) fields or even in the complete absence of EM fields as long as a suitable strain is present. It has been reported that strain is able to Landau-quantize 2D Weyl magnons hosted by "magnon graphene" and leads to a non-quantized Hall viscosity [91]. Since 3D Weyl magnons have been predicted to exist in pyrochlore magnets [20–23], double perovskite magnets [24] and multilayer magnets [25–27], it is natural to ask how strain engages in the transport of 3D Weyl magnons harbored by these Weyl magnets.

In this chapter, we answer this question by a combination of analytical calculations and numerical simulations. We show that a static torsional

strain can induce a pseudo-electric field to Landau-quantize the 3D Weyl magnons, and a dynamic uniaxial strain can induce a pseudo-magnetic field to pump the magnons. We also demonstrate that these elastic strain-induced pseudo-EM fields result in novel magnon transport in the form of quantum anomalies. To support these findings, we organize the chapter as follows. In Section 4.1, we formulate the model of a multilayer Weyl ferromagnet and discuss its magnon band structure and topology. In Section 4.2, we study the magnon band structures of the Weyl ferromagnet under an electric field and under a static torsional strain-induced pseudo-electric field respectively. We also study the magnon dynamics due to either a magnetic field or a dynamic uniaxial strain-induced pseudo-magnetic field. In Section 4.3, we derive the magnon quantum anomalies and the associated anomalous spin and heat currents under different combinations of EM fields and pseudo-EM fields. In Section 4.4, we derive the field (gradient) dependence of the anomalous spin and heat currents in various magnon quantum anomalies, and establish a duality to the anomalous electric current in the chiral magnetic effect [62, 63] and the chiral torsional effect [93, 94] of Weyl semimetals. In Section 4.5, we discuss the proposals for experimentally measuring magnon quantum anomalies by atomic force microscopy (AFM) force sensing. Section 4.6 concludes the chapter, proposes several promising materials for the implementation of magnon quantum anomalies, and envisages a few worthwhile directions based on the current work.

## 4.1 Model of Weyl ferromagnets

We consider a multilayer Weyl ferromagnet model proposed in Ref. [25] but amend the model with an inter-layer next nearest neighbor interaction. It will be shown in Section 4.2.2 that such an interaction is necessary for the strain engineering for Landau quantization. The building block of this model is a honeycomb ferromagnet layer of spins of size $S$ (Fig. 4.1(a)), which has been experimentally realized in $CrI_3$ [169] and proposed in other compounds [170]. Multiple layers are then stacked in the $z$ direction (Fig. 4.1(b)). The in-plane nearest neighbors are labelled by $\boldsymbol{\alpha}_1 = \frac{\sqrt{3}}{2}a\hat{x} + \frac{1}{2}a\hat{y}$, $\boldsymbol{\alpha}_2 = -\frac{\sqrt{3}}{2}a\hat{x} + \frac{1}{2}a\hat{y}$, and $\boldsymbol{\alpha}_3 = -a\hat{y}$, where $a$ is the lattice constant of the honeycomb lattice; the in-plane next nearest neighbors are labelled by $\boldsymbol{\beta}_1 = \boldsymbol{\alpha}_3 - \boldsymbol{\alpha}_2$, $\boldsymbol{\beta}_2 = \boldsymbol{\alpha}_1 - \boldsymbol{\alpha}_3$, and $\boldsymbol{\beta}_3 = \boldsymbol{\alpha}_2 - \boldsymbol{\alpha}_1$. The inter-layer spacing (out-of-plane direction lattice constant) is denoted as $\delta_z$. We choose the unit cells of the honeycomb layer such that each contains an $A$ site and a $B$ site connected by vector $\boldsymbol{\alpha}_1$.

The Heisenberg Hamiltonian of the Weyl ferromagnet reads

$$H = H_0 + H_1 + H_2 + H_z + H_D + Z, \tag{4.1}$$

with its components listed explicitly below

$$H_0 = -\sum_{\boldsymbol{R}_\perp, z} \sum_{\mu=A,B} K_\mu S^z_\mu(\boldsymbol{R}_\perp, z) S^z_\mu(\boldsymbol{R}_\perp, z),$$

$$H_1 = -\sum_{\boldsymbol{R}_\perp, z} \sum_i J_1(\boldsymbol{\alpha}_i) \boldsymbol{S}_A(\boldsymbol{R}_\perp, z) \cdot \boldsymbol{S}_B(\boldsymbol{R}_\perp + \boldsymbol{\alpha}_i - \boldsymbol{\alpha}_1, z),$$

$$H_2 = -\sum_{\boldsymbol{R}_\perp, z} \sum_i \sum_{s=\pm 1} J_2(\boldsymbol{\alpha}_i + s\delta_z \hat{z}) \boldsymbol{S}_A(\boldsymbol{R}_\perp, z) \cdot \boldsymbol{S}_B(\boldsymbol{R}_\perp + \boldsymbol{\alpha}_i - \boldsymbol{\alpha}_1, z + s\delta_z)$$

$$H_z = -\sum_{\boldsymbol{R}_\perp, z} \sum_{\mu=A,B} J_\mu(\delta_z \hat{z}) \boldsymbol{S}_\mu(\boldsymbol{R}_\perp, z) \cdot \boldsymbol{S}_\mu(\boldsymbol{R}_\perp, z + \delta_z),$$

$$H_D = \sum_{\boldsymbol{R}_\perp, z} \sum_i \sum_{\mu=A,B} \boldsymbol{D}_\mu \cdot [\boldsymbol{S}_\mu(\boldsymbol{R}_\perp, z) \times \boldsymbol{S}_\mu(\boldsymbol{R}_\perp + \boldsymbol{\beta}_i, z)],$$

$$Z = -g\mu_B B_z \sum_{\boldsymbol{R}_\perp, z} \sum_{\mu=A,B} S^z_\mu(\boldsymbol{R}_\perp, z),$$

where $\boldsymbol{R}_\perp$ labels the unit cells of a honeycomb layer, and $z$ is the layer index. $H_0$ is an on-site interaction term with strength $K_{A(B)}$ on $A(B)$ sites; $H_1$ is the intra-layer nearest neighbor interaction with strength $J_1(\boldsymbol{\alpha}_i)$ between $A$ and $B$ sites connected by vector $\boldsymbol{\alpha}_i$; $H_2$ is the inter-layer next nearest neighbor interaction with strength $J_2(\boldsymbol{\alpha}_i \pm \boldsymbol{\delta}_z)$ between $A$ and $B$ sites connected by vector $\boldsymbol{\alpha}_i \pm \boldsymbol{\delta}_z$; $H_z$ is the inter-layer nearest neighbor interaction with strength $J_{A(B)}$ between same-sublattice sites spaced by $\delta_z$ in the stacking direction $z$; $H_D$ is the intra-layer next nearest neighbor Dzyaloshinskii-Moriya (DM) interaction [171, 172] between same-sublattice sites connected by $\boldsymbol{\beta}_i$; and the last term $Z$ is the Zeeman energy. For simplicity, we choose the interaction strength as $D_A = -D_B = D > 0$, $J_1(\boldsymbol{\alpha}_i) = J_1 > 0$, and $J_2(\boldsymbol{\alpha}_i \pm \delta_z \hat{z}) = J_2 > 0$. Moreover, since the Zeeman term only determines the spin polarization of the ground state, we henceforth set $B_z \to 0^+$. We further assume the inter-layer lattice constant $\delta_z = a$.

The Heisenberg Hamiltonian (Eq. 4.1) can be rewritten in terms of magnons through the Holstein-Primakoff transformation [147],

$$S_\mu^+(\boldsymbol{R}) = \sqrt{2S}\sqrt{1-\frac{\mu_{\boldsymbol{R}}^\dagger\mu_{\boldsymbol{R}}}{2S}}\mu_{\boldsymbol{R}},$$
$$S_\mu^-(\boldsymbol{R}) = \sqrt{2S}\mu_{\boldsymbol{R}}^\dagger\sqrt{1-\frac{\mu_{\boldsymbol{R}}^\dagger\mu_{\boldsymbol{R}}}{2S}},$$
$$S_\mu^z(\boldsymbol{R}) = S-\mu_{\boldsymbol{R}}^\dagger\mu_{\boldsymbol{R}},$$

where $\boldsymbol{R}=(\boldsymbol{R}_\perp, z)$ indicates the position of the unit cell, $\mu = A, B$ is the sublattice index, and $\mu_{\boldsymbol{R}}^\dagger/\mu_{\boldsymbol{R}}$ is the corresponding magnon creation/annihilation operator. In the single-particle limit, the Hamiltonian becomes

$$H = E_{\mathrm{FM}} + H_{\mathrm{M}}, \tag{4.2}$$

where the ferromagnetic ground state energy $E_{\mathrm{FM}} = -NS^2(K_A+K_B+J_A+J_B+3J_1+6J_2)$ and the tight binding magnon Hamiltonian is

$$\begin{aligned}
H_{\mathrm{M}} = {} & 2K_AS\sum_{\boldsymbol{R}_\perp,z} a_{\boldsymbol{R}_\perp,z}^\dagger a_{\boldsymbol{R}_\perp,z} + 2K_BS\sum_{\boldsymbol{R}_\perp,z} b_{\boldsymbol{R}_\perp,z}^\dagger b_{\boldsymbol{R}_\perp,z} \\
& + (3J_1+6J_2)S\sum_{\boldsymbol{R}_\perp,z}(a_{\boldsymbol{R}_\perp,z}^\dagger a_{\boldsymbol{R}_\perp,z} + b_{\boldsymbol{R}_\perp,z}^\dagger b_{\boldsymbol{R}_\perp,z}) \\
& + 2J_AS\sum_{\boldsymbol{R}_\perp,z} a_{\boldsymbol{R}_\perp,z}^\dagger a_{\boldsymbol{R}_\perp,z} + 2J_BS\sum_{\boldsymbol{R}_\perp,z} b_{\boldsymbol{R}_\perp,z}^\dagger b_{\boldsymbol{R}_\perp,z} \\
& + \Bigg\{ iDS\sum_{\boldsymbol{R}_\perp,z}\sum_i(-a_{\boldsymbol{R}_\perp,z}^\dagger a_{\boldsymbol{R}_\perp+\boldsymbol{\beta}_i,z} + b_{\boldsymbol{R}_\perp,z}^\dagger b_{\boldsymbol{R}_\perp+\boldsymbol{\beta}_i,z}) \\
& - J_AS\sum_{\boldsymbol{R}_\perp,z} a_{\boldsymbol{R}_\perp,z}^\dagger a_{\boldsymbol{R}_\perp,z+a} - J_BS\sum_{\boldsymbol{R}_\perp,z} b_{\boldsymbol{R}_\perp,z}^\dagger b_{\boldsymbol{R}_\perp,z+a} \\
& - J_1S\sum_{\boldsymbol{R}_\perp,z}\sum_i a_{\boldsymbol{R}_\perp,z}^\dagger b_{\boldsymbol{R}_\perp+\boldsymbol{\alpha}_i-\boldsymbol{\alpha}_1,z} \\
& - J_2S\sum_{\boldsymbol{R}_\perp,z}\sum_i\sum_{s=\pm1} a_{\boldsymbol{R}_\perp,z}^\dagger b_{\boldsymbol{R}_\perp+\boldsymbol{\alpha}_i-\boldsymbol{\alpha}_1,z+sa} + \mathrm{H.c.}\Bigg\}.
\end{aligned} \tag{4.3}$$

We then perform Fourier transform

$$a_{\boldsymbol{R}_\perp,z} = \frac{1}{\sqrt{N}}\sum_{\boldsymbol{k}} e^{i\boldsymbol{k}_\perp\cdot\boldsymbol{R}_\perp}e^{ik_zz}a_{\boldsymbol{k}}, \tag{4.4}$$

$$b_{\boldsymbol{R}_\perp,z} = \frac{1}{\sqrt{N}}\sum_{\boldsymbol{k}} e^{i\boldsymbol{k}_\perp\cdot(\boldsymbol{R}_\perp+\boldsymbol{\alpha}_1)}e^{ik_zz}b_{\boldsymbol{k}}, \tag{4.5}$$

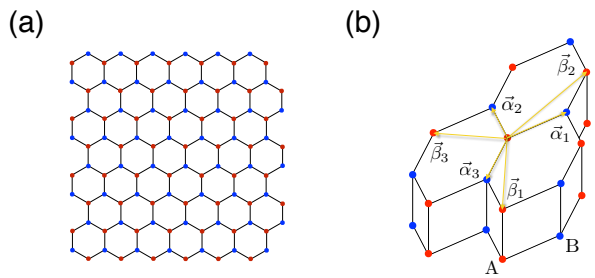


Figure 4.1: Schematic plot for the Weyl ferromagnet multilayer. (a) 2D honeycomb ferromagnet sheet. The Weyl ferromagnet multilayer is constructed by stacking many sheets in the $z$ direction. (b) Conventional crystal cells of the Weyl ferromagnet with in-plane nearest (second nearest) neighbors connected by $\boldsymbol{\alpha}_i$ ($\boldsymbol{\beta}_i$), $i = 1, 2, 3$.

where $\boldsymbol{k} = (\boldsymbol{k}_\perp, k_z)$ and $N$ is the number of unit cells in the Weyl ferromagnet multilayer. Then the tight-binding Hamiltonian can be written as

$$H_{\mathrm{M}} = \sum_{\boldsymbol{k}} \psi^\dagger_{\boldsymbol{k}} \mathcal{H}_{\boldsymbol{k}} \psi_{\boldsymbol{k}}, \tag{4.6}$$

where the sublattice basis is $\psi_{\boldsymbol{k}} = (a_{\boldsymbol{k}}, b_{\boldsymbol{k}})^T$ and the first-quantized Bloch Hamiltonian is

$$\begin{aligned}\mathcal{H}_{\boldsymbol{k}} = (-J_1 - 2J_2 \cos k_z a) S \sum_i \cos(\boldsymbol{k} \cdot \boldsymbol{\alpha}_i) \sigma^x \\ + (J_1 + 2J_2 \cos k_z a) S \sum_i \sin(\boldsymbol{k} \cdot \boldsymbol{\alpha}_i) \sigma^y \\ + [K_- + J_-(1 - \cos k_z a) + 2D \sum_i \sin(\boldsymbol{k} \cdot \boldsymbol{\beta}_i)] S \sigma^z \\ + [3J_1 + 6J_2 + K_+ + J_+(1 - \cos k_z a)] S \sigma^0,\end{aligned} \tag{4.7}$$

where $\boldsymbol{\sigma}$ and $\sigma^0$ are Pauli matrices and the identity matrix, respectively, and we have used the notations $K_\pm = K_A \pm K_B$ and $J_\pm = J_A \pm J_B$. It is easy to find that $\mathcal{H}_{\boldsymbol{k}}$ can only be gapless at the corners of the 2D hexagonal Brillouin zone of the honeycomb ferromagnet. For simplicity, we require $K_- + 3\sqrt{3}D > 0$ but $-2J_1 < K_- - 3\sqrt{3}D < 0$. In this case, there is only one pair of nodal points $\boldsymbol{k}^\eta_W = (-\frac{4\pi}{3\sqrt{3}a}, 0, \eta Q)$ with $\eta = \pm 1$ and

$$Q = \frac{1}{a} \cos^{-1}\left(\frac{K_- + J_- - 3\sqrt{3}D}{J_-}\right). \tag{4.8}$$

In the vicinity of these Weyl points, the Bloch Hamiltonian can be expanded to the lowest order as

$$\mathcal{H}_{\boldsymbol{k}_W^\eta+\boldsymbol{q}} = \mathcal{H}_{\boldsymbol{k}_W^\eta} + \hbar v_0^\eta q_z \sigma^0 + \sum_{i=x,y,z} \hbar v_i^\eta q_i \sigma^i, \tag{4.9}$$

with the corresponding velocity parameters defined as

$$\begin{aligned} v_x^\eta &= -\frac{3}{2\hbar}(J_1 + 2J_2 \cos Qa) Sa, \\ v_y^\eta &= -\frac{3}{2\hbar}(J_1 + 2J_2 \cos Qa) Sa, \\ v_z^\eta &= \frac{\eta}{\hbar} J_- Sa \sin Qa, \\ v_0^\eta &= \frac{\eta}{\hbar} J_+ Sa \sin Qa. \end{aligned}$$

Without loss of generality, we take $J_- > 0$. Then the Berry flux (in units of $\pi$) that flows into/out of the Weyl points is

$$\chi_\eta = \mathrm{sgn}(v_x v_y v_z) = \mathrm{sgn}(v_z) = \eta, \tag{4.10}$$

which is locked to the momentum space position of Weyl points. The topological nature of $\mathcal{H}_{\boldsymbol{k}}$ can be verified by evaluating the Chern number of a 2D slice with fixed $k_z$, which is

$$C_{k_z} = \frac{1}{2}\mathrm{sgn}\big[K_- + J_-(1 - \cos k_z a) - 3\sqrt{3}D\big] - \frac{1}{2}. \tag{4.11}$$

Based on the restrictions we impose on the parameters, we obtain

$$C_{k_z} = \begin{cases} -1 & |k_z| < Q \\ 0 & Q < |k_z| < \pi \end{cases}. \tag{4.12}$$

Therefore, we expect arc surface states, which are akin to Fermi arcs in an electronic Weyl semimetal, connecting magnon Weyl points at the topological crystal momenta $|k_z| < Q$. To confirm this, we numerically calculate the band structure (Fig. 4.2(a)-(d)) of a Weyl ferromagnet nanowire whose cross section containing 1800 lattice sites is schematically plotted in Fig. 4.3(b). The open boundary of the cross section consists of one pair of zigzag edges ($x$-direction) and one pair of armchair edges ($y$-direction). For simplicity and visual clarity, we set $J_+ = 0$ in Eq. 4.7 while taking care to preserve the positive-definiteness of the magnon energy/spin wave frequency; the $J_+$ term will be reinstated in Appendix D. As illustrated in Fig. 4.2(a), the Weyl

ferromagnet nanowire exhibits a pair of Weyl cones connected by a set of almost flat bands. When the boundaries are closed, these flat bands disappear in Fig. 4.2(b), indicating that the flat bands only reside on the surface of the nanowire. This can be further confirmed by evaluating the spectral functions: these flat states have a large spectral density at the surface (Fig. 4.2(c)) but disappear deep in the bulk (Fig. 4.2(d)).

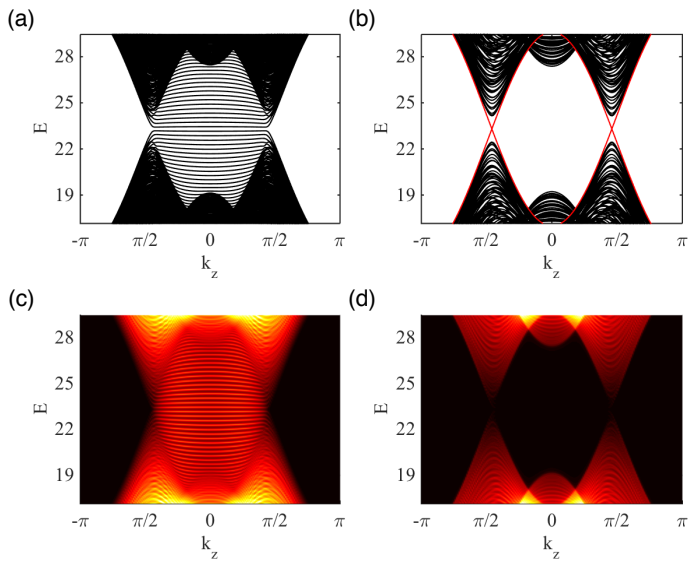


Figure 4.2: Magnon dispersion and spectral functions for the Weyl ferromagnet multilayer. For all panels, we set $DS = 1$ and measure energies in terms of $DS$ such that $J_1S = 4.56$, $J_2S = 1.14$, $J_-S = 7.22$, $K_+S = 2.77$ and $K_-S = -1.12$. (a) Magnon band structure for the nanowire with a pair of zigzag edges and a pair of armchair edges in the cross section. The cross section of the nanowire is illustrated in Fig. 4.3(b). The magnon bands exhibit two Weyl points on the $k_z$ axis and are connected by a set of almost flat states analogous to the arc states in Weyl semimetals. (b) Magnon bands for the nanowire with periodic boundary conditions for the cross section. The flat bands disappear, indicating their surface origin. The red curves are the analytical dispersion $\epsilon_{\boldsymbol{k}} = [K_+ + 3J_1 + 6J_2]S \pm [K_- + J_-(1 - \cos k_z a) - 3\sqrt{3}D]S$ for the Bloch Hamiltonian $\mathcal{H}_{\boldsymbol{k}}$ at the honeycomb lattice Brillouin zone corner $\boldsymbol{k}_\perp = (-4\pi/3\sqrt{3}a, 0)$. (c) Surface spectral function of the Bloch Hamiltonian which confirms that the almost flat states reside on surfaces. (d) Bulk spectral function which indicates the positions of Weyl cones.

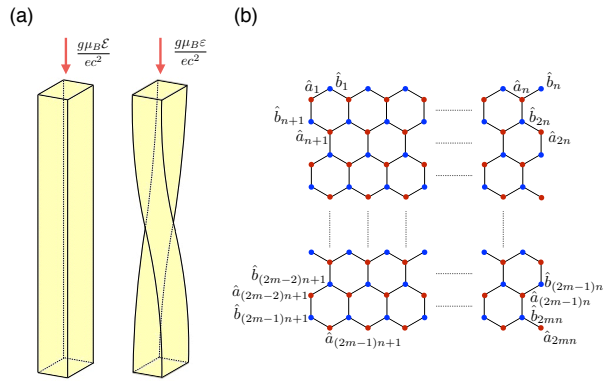


Figure 4.3: Schematic plot for the Weyl ferromagnet nanowire. (a) Nanowire under an inhomogeneous electric field and nanowire under a twist deformation. Landau quantization takes place in both cases. (b) Cross section of the Weyl ferromagnet nanowire with a pair of zigzag edges ($x$-direction) and a pair of armchair edges ($y$-direction). We use $m = n = 30$ unless otherwise specified so that all numerical simulations could be implemented with available computational resources.

## 4.2 Weyl ferromagnets under electromagnetic fields and strain

In Section 4.1, we introduced a multilayer model for the Weyl ferromagnet and discussed the magnon band topology. In order to obtain magnon quantum anomalies, gauge fields are needed to manipulate magnons. In the present section, we will first discuss the Landau quantization of magnon bands in the presence of an inhomogeneous electric field $\boldsymbol{E}$ (Section 4.2.1) or an inhomogeneous chiral pseudo-electric field $\boldsymbol{e}^\eta$ (Section 4.2.2) induced by a static twist deformation of the Weyl ferromagnet nanowire. Then we derive the equation of motion for magnons under an inhomogeneous magnetic field $\boldsymbol{B}$ (Section 4.2.3) or an inhomogeneous chiral pseudo-magnetic field $\boldsymbol{b}^\eta$ (Section 4.2.4) induced by a dynamic uniaxial strain.

### 4.2.1 Landau quantization in the presence of electric field

To begin with, we study the magnon band structure under an electric field $\boldsymbol{E}$. Dual to the Aharonov-Bohm phase $\phi_{\mathrm{AB}} = -\frac{e}{\hbar}\int_{\boldsymbol{r}}^{\boldsymbol{r}+\boldsymbol{\delta}} \boldsymbol{A}\cdot d\boldsymbol{l}$ acquired by

electrons moving in a magnetic field $\boldsymbol{B} = \nabla \times \boldsymbol{A}$, magnons moving in an electric field can acquire an Aharonov-Casher phase [83]

$$\phi_{\mathrm{AC}} = -\frac{e}{\hbar}\int_{\boldsymbol{r}}^{\boldsymbol{r}+\boldsymbol{\delta}} \frac{1}{ec^2}(\boldsymbol{E}\times\boldsymbol{\mu})\cdot d\boldsymbol{l}, \tag{4.13}$$

where the curl of the integrand $\frac{1}{ec^2}\nabla\times(\boldsymbol{E}\times\boldsymbol{\mu})$ is dual to the magnetic field in electronics and will Landau-quantize the magnon bands. When transformed to the reciprocal space, the Aharonov-Casher phase results in the Peierls substitution $\boldsymbol{k}\to\boldsymbol{k}+\frac{e}{\hbar}\frac{1}{ec^2}\boldsymbol{E}\times\boldsymbol{\mu}$. Explicitly, if we take the magnon magnetic moment $\boldsymbol{\mu} = -g\mu_B\hat{z}$ and the electric field $\boldsymbol{E} = (\frac{1}{2}\mathcal{E}x, \frac{1}{2}\mathcal{E}y, 0)$, which may be experimentally realized by periodically arranging scanning tunneling microscope (STM) tips [150][8]. The resulting Dirac-Landau levels are given by

$$\epsilon_n^\eta(q_z) = \pm\hbar\sqrt{\left(v_z^\eta q_z\right)^2 + 2n\left|\frac{g\mu_B\mathcal{E}}{\hbar c^2}v_x^\eta v_y^\eta\right|} \quad n = 1, 2, \cdots, \tag{4.14}$$

and

$$\epsilon_0^\eta(q_z) = -\mathrm{sgn}\left(\frac{g\mu_B\mathcal{E}}{\hbar c^2}v_x^\eta v_y^\eta\right)\hbar v_z^\eta q_z = -\eta\,\mathrm{sgn}(g\mathcal{E})\hbar|v_z^\eta|q_z. \tag{4.15}$$

The higher ($n > 1$) Landau levels at both Weyl points are identical and they always come in pairs with opposite energies at each momentum $q_z$. However, the zeroth Landau levels at the two Weyl points are not identical but counter-propagating. Without loss of generality, we choose $\mathrm{sgn}(g\mathcal{E}) = -1$ such that the right (left) Weyl cone hosts a right (left) moving zeroth Landau level $\hbar|v_z^\eta|q_z$ ($-\hbar|v_z^\eta|q_z$). Unlike higher Landau levels, at each Weyl point, the zeroth Landau levels are unpaired.

To numerically verify the Landau quantization due to the Aharonov-Casher effect, we consider the nanowire geometry under an electric field (left panel, Fig. 4.3(a)). The calculated band structure of the Weyl ferromagnet nanowire under an inhomogeneous electric field is shown in Fig. 4.4(a). The zeroth Landau levels can be easily identified, and are connected by a set of almost flat states whose surface origin can be confirmed by calculating the surface spectral function (Fig. 4.4(b)). The obscured higher Landau levels, on the other hand, are revealed by the bulk spectral function as illustrated in Fig. 4.4(c).

[8] At least in principle, there is another proposal to experimentally realize such electric field. In particular, a uniformly charged cylindrical Weyl ferromagnet nanowire produces an electric field $\boldsymbol{E} = \frac{1}{2}\mathcal{E}r\hat{r}$, where the field gradient is $\mathcal{E} = \frac{\rho}{\epsilon_0\epsilon_r}$ with $\rho$ being the charge density and $\epsilon_0\epsilon_r$ being the permittivity of the nanowire. For the field gradient used in Fig. 4.4, a charge density $\sim 10^{10}\mathrm{C/m}^3$ is needed.

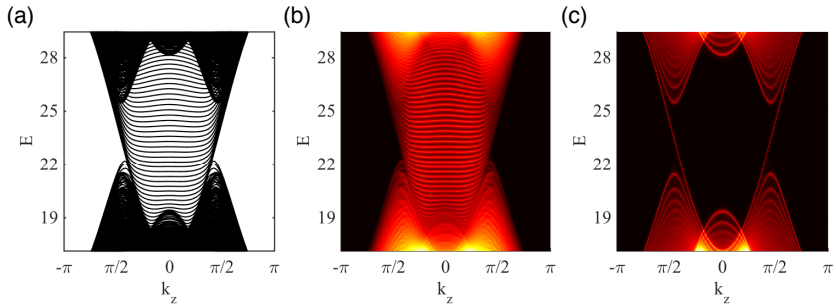


Figure 4.4: Magnon dispersion of the Weyl ferromagnet nanowire under an inhomogeneous electric field. For all panels, we take $\frac{g\mu_B \mathcal{E} a^2}{ec^2} = -0.0124\Phi_0$ where $\mathcal{E}$ represents the gradient of the external electric field and $\Phi_0 = h/2e$ is the magnetic flux quantum. (a) Magnon bands are Landau-quantized by the external inhomogeneous electric field due to the Aharonov-Casher effect. The two resulting zeroth Landau levels at different Weyl points have opposite velocities $\pm|v_z^\eta|$ and are connected by a set of almost flat states. (b) Surface spectral function, which reveals that these flat bands are localized at the surface of the Weyl ferromagnet nanowire. (c) Bulk spectral function highlighting the Dirac-Landau levels at each Weyl cone.

### 4.2.2 Landau quantization in the presence of pseudo-electric field

In the context of Weyl semimetals, besides applying a magnetic field $\boldsymbol{B}$, the electronic bands are also Landau-quantized by a suitable lattice deformation [92–95, 134], which spatially modulates the overlap integrals. The overall effect of such a deformation on the low-energy Hamiltonian is a minimal substitution analogous to that for a magnetic field. In other words, the lattice deformation due to external strain induces a pseudo-magnetic field. It is worth noting that such a strain-induced pseudo-magnetic field only couples to the Weyl points and becomes negligible at energies far away from the Weyl points. In this section, we will show that a similar strain-induced pseudo-electric field can be generated by spin lattice deformation and leads to Landau quantization of Weyl magnons.

For concreteness, we consider the spin lattice deformation due to a twist (Fig. 4.3(a), right panel). The resulting displacement field is

$$\boldsymbol{u} = \frac{z}{L}(\boldsymbol{\Omega} \times \boldsymbol{R}_\perp), \tag{4.16}$$

where $\Omega$ is the angle of rotation of the uppermost layer with respect to the lowermost layer, and $L$ is the spacing between these two layers, i.e., the length of the nanowire. For this displacement field, the non-zero components of the symmetric strain tensor $u_{ij} = \frac{1}{2}(\partial_i u_j + \partial_j u_i)$ are $u_{13} = u_{31} = -\Omega y/2L$ and $u_{23} = u_{32} = \Omega x/2L$. Based on the experience of the overlap integral substitution (Eq. 1.23) in Section 1.3, we only need to consider the exchange integrals whose arguments simultaneously have out-of-plane and in-plane components. In our model, this refers to the six $J_2$'s as illustrated in Fig. 4.5.

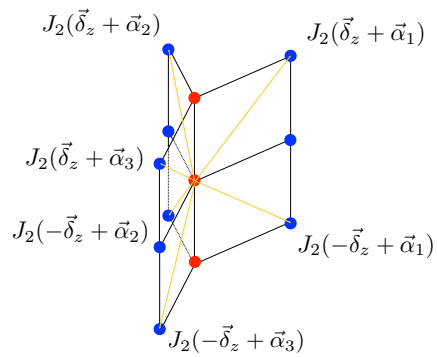


Figure 4.5: Schematic plot for the exchange integrals $J_2$. The most important impact of the twist deformation is to modulate $J_2$ spatially.

The substitutions for these $J_2$'s are

$$\begin{aligned}
&J_2(\boldsymbol{\alpha}_1 \pm a\hat{z}) \to J_2(1 \mp \tfrac{\sqrt{3}}{2}u_{31} \mp \tfrac{1}{2}u_{32}),\\
&J_2(\boldsymbol{\alpha}_2 \pm a\hat{z}) \to J_2(1 \pm \tfrac{\sqrt{3}}{2}u_{31} \mp \tfrac{1}{2}u_{32}),\\
&J_2(\boldsymbol{\alpha}_3 \pm a\hat{z}) \to J_2(1 \pm u_{32}),
\end{aligned}$$

under which an additional term appears in $\mathcal{H}_{\boldsymbol{k}}$

$$\delta\mathcal{H}^{\boldsymbol{e}}_{\boldsymbol{k}} = -2J_2 S \sin k_z a \sum_i d_i(\sin \boldsymbol{k}\cdot\boldsymbol{\alpha}_i\sigma^x + \cos \boldsymbol{k}\cdot\boldsymbol{\alpha}_i\sigma^y), \tag{4.17}$$

where

$$(d_1, d_2, d_3) = \Big(\frac{\sqrt{3}}{2}u_{31} + \frac{1}{2}u_{32}, -\frac{\sqrt{3}}{2}u_{31} + \frac{1}{2}u_{32}, -u_{32}\Big).$$

In the vicinity of the Weyl points $\boldsymbol{k}_W^\eta$, the Bloch Hamiltonian of the twisted Weyl ferromagnet nanowire reads

$$\begin{aligned}\mathcal{H}_{\boldsymbol{k}_W^\eta+\boldsymbol{q}} + \delta\mathcal{H}^{\boldsymbol{e}}_{\boldsymbol{k}_W^\eta+\boldsymbol{q}} &\approx \mathcal{H}_{\boldsymbol{k}_W^\eta} + \hbar v_0^\eta q_z \sigma^0 + \sum_i \hbar v_i^\eta q_i \sigma^i + \delta\mathcal{H}^{\boldsymbol{e}}_{\boldsymbol{k}_W^\eta} \\ &= \mathcal{H}_{\boldsymbol{k}_W^\eta} + \hbar v_0^\eta \Big(q_z + \frac{e}{\hbar} a^\eta_{S,z}\Big)\sigma^0 + \sum_i \hbar v_i^\eta \Big(q_i + \frac{e}{\hbar} a^\eta_{S,i}\Big)\sigma^i. \quad (4.18)\end{aligned}$$

It is worth noting that the strain-induced term can be incorporated into the linearized Hamiltonian through a minimal substitution $\boldsymbol{q} \to \boldsymbol{q} + \frac{e}{\hbar}\boldsymbol{a}_S^\eta$, where the strain-induced vector potential is

$$\boldsymbol{a}_S^\eta = -\eta \frac{2\hbar}{ea} \frac{J_2 \sin Qa}{J_1 + 2J_2 \cos Qa}(u_{31}, u_{32}, 0), \quad (4.19)$$

which is a chiral gauge field taking opposite values at different Weyl points. We note that the multilayer model in Ref. [25] does not have such a strain-induced vector potential because the inter-layer next nearest neighbor interaction is not considered, i.e., $J_2 = 0$. As $\nabla \times \boldsymbol{a}_S^\eta \neq 0$, this strain-induced vector potential will result in Landau quantization of magnon bands. In Section 4.2.1, we demonstrate that electric field $\boldsymbol{E} = (\frac{1}{2}\mathcal{E}x, \frac{1}{2}\mathcal{E}y, 0)$ produces Landau quantization through the Aharonov-Casher effect. Therefore, we may interpret $\boldsymbol{a}_S^\eta$ as the vector potential of a chiral pseudo-electric field $\boldsymbol{e}^\eta = \eta\boldsymbol{e} = \eta(\frac{1}{2}\varepsilon x, \frac{1}{2}\varepsilon y, 0)$, which only differs from $\boldsymbol{E}$ by a chiral charge $\eta$. The field gradient of this pseudo-electric field can be determined by $\nabla \times \boldsymbol{a}_S^\eta = \frac{1}{ec^2}\nabla \times (\boldsymbol{e}^\eta \times \boldsymbol{\mu}) = \eta \frac{g\mu_B \varepsilon}{ec^2}\hat{z}$. Explicitly, the gradient reads

$$\varepsilon = -\frac{2\hbar}{ea} \frac{J_2 \sin Qa}{J_1 + 2J_2 \cos Qa} \frac{\Omega}{L} \frac{ec^2}{g\mu_B}. \quad (4.20)$$

It is critically important to note that the strain-induced vector potential is a unique feature of relativistic particles. We thus expect that the strain-induced pseudo-electric field and magnon Dirac-Landau levels only reside in the vicinity of magnon Weyl points. Unlike the electric field $\boldsymbol{E}$ which produces counter-propagating zeroth Landau levels, the chiral pseudo-electric field $\boldsymbol{e}^\eta$ results in co-propagating zeroth Landau levels on the Weyl points as illustrated in Fig. 4.6(a,c). At the first glance, this causes an imbalance in the numbers of left-moving and right-moving channels, which must be the same in a lattice model. Considering that we have only discussed bulk Landau levels so far, we argue that there should be a set of surface states connecting the bulk Landau levels at the two Weyl cones, providing the needed counter-propagating channels to compensate the imbalance. Our argument has been

confirmed by the numerical simulation of the surface spectral function as illustrated in Fig. 4.6(b). Remarkably, we note that inside the gap spanned by the two first Landau levels, the left-moving surface channels and right-moving bulk channels are spatially well separated and cannot be scattered into each other. Therefore, if the reservoirs are fine-tuned to populate this gap with magnons [25, 173], the bulk magnon particle current and surface magnon particle current are counter-propagating in the ballistic regime. This leads to exotic spin and heat transport known as the bulk-surface separation which will be elaborated in Section 4.3.

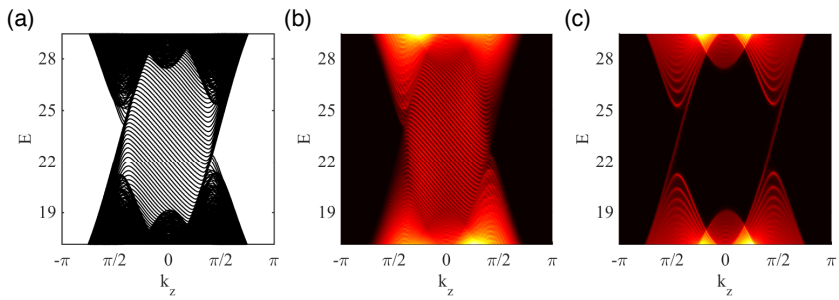


Figure 4.6: Magnon dispersion of a twisted Weyl ferromagnet nanowire. For all panels, we take $\frac{g\mu_B \varepsilon a^2}{ec^2} = -0.0124\Phi_0$ where $\varepsilon$ represents the gradient of the strain-induced pseudo-electric field. (a) Magnon bands are Landau-quantized by the strain-induced pseudo-electric field. The resulting zeroth Landau levels at the two Weyl points are both right-moving and are connected by a set of left-moving states. (b) Surface spectral function, which reveals that these left-moving states are localized at the surface of the Weyl ferromagnet nanowire. (c) Bulk spectral function highlighting the Dirac-Landau levels at each Weyl cone.

### 4.2.3 Magnon motion in the presence of magnetic field

In Section 4.2.1, we have Landau-quantized the magnon bands by applying an inhomogeneous electric field $\boldsymbol{E}$. To implement quantum anomalies with magnons, we need to pump them through the zeroth Landau levels. In this section, we will elucidate how magnons are pumped by an inhomogeneous magnetic field $\boldsymbol{B}$. The equation of motion of magnons will be derived.

Due to the magnetic moment it carries, a magnon has a Zeeman energy $U = -\boldsymbol{\mu} \cdot \boldsymbol{B}$ in the presence of a magnetic field $\boldsymbol{B}$. The force exerted on

the magnon is then $\boldsymbol{F} = -\nabla U = \nabla(\boldsymbol{\mu}\cdot\boldsymbol{B}) = \hbar\frac{d\boldsymbol{k}}{dt}$. Practically, we are only concerned about the transport in the $z$ direction, which is governed by

$$\hbar\frac{dk_z}{dt} = \partial_z(\boldsymbol{\mu}\cdot\boldsymbol{B}). \tag{4.21}$$

Therefore, an inhomogeneous magnetic field in the $z$-direction will be capable of driving magnons from one magnon Weyl point to the other. More generally, we consider the case where there is also an electric field $\boldsymbol{E}$ in addition to $\boldsymbol{B}$. As discussed in Section 4.2.1, due to the Aharonov-Casher phase, the canonical momentum will be shifted through the Peierls substitution $\boldsymbol{p}\to\boldsymbol{p}+\frac{1}{c^2}\boldsymbol{E}\times\boldsymbol{\mu}$ in the presence of $\boldsymbol{E}$. Then the magnon Hamiltonian can be written down as

$$\mathscr{H}_M = K\big(\boldsymbol{p}+\tfrac{1}{c^2}\boldsymbol{E}\times\boldsymbol{\mu}\big) - \boldsymbol{\mu}\cdot\boldsymbol{B}, \tag{4.22}$$

where $K(\boldsymbol{p})$ is the magnon kinetic energy whose specific form does not matter for our purpose. The Hamilton's equations of motion give

$$\boldsymbol{v} = \frac{\partial\mathscr{H}_M}{\partial\boldsymbol{p}} = \frac{\partial K}{\partial\boldsymbol{p}}, \tag{4.23}$$

and

$$\frac{d\boldsymbol{p}}{dt} = -\frac{\partial\mathscr{H}_M}{\partial\boldsymbol{r}} = \frac{1}{c^2}\nabla[\boldsymbol{v}\cdot(\boldsymbol{\mu}\times\boldsymbol{E})] + \nabla(\boldsymbol{\mu}\cdot\boldsymbol{B}). \tag{4.24}$$

Therefore, the equation of motion for the crystal momentum $\boldsymbol{k} = \frac{1}{\hbar}\boldsymbol{p}+\frac{1}{\hbar c^2}\boldsymbol{E}\times\boldsymbol{\mu}$ is

$$\hbar\frac{d\boldsymbol{k}}{dt} = \nabla(\boldsymbol{\mu}\cdot\boldsymbol{B}) - \frac{\partial}{\partial t}\frac{1}{c^2}\boldsymbol{\mu}\times\boldsymbol{E} + \frac{1}{c^2}\boldsymbol{v}\times[\nabla\times(\boldsymbol{\mu}\times\boldsymbol{E})], \tag{4.25}$$

which clearly shows the duality to electronics with the magnon Zeeman energy $-\boldsymbol{\mu}\cdot\boldsymbol{B}$ (the electric momentum $\boldsymbol{\mu}\times\boldsymbol{E}$) playing the role of the electric potential energy $-e\phi$ (the magnetic momentum $e\boldsymbol{A}$). For the inhomogeneous electric field $\boldsymbol{E} = (\frac{1}{2}\mathcal{E}x, \frac{1}{2}\mathcal{E}y, 0)$ and the magnetic moment $\boldsymbol{\mu} = -g\mu_B\hat{z}$ used in Section 4.2.1, the $z$ component of Eq. 4.25 is exactly Eq. 4.21.

In summary, an inhomogeneous magnetic field can be used to pump magnons along the $z$ direction and is capable of producing magnon quantum anomalies. This will be discussed in detail in Section 4.3.1 and Section 4.3.4. In the meanwhile, a static inhomogeneous electric field only provides Landau quantization and does not affect the magnon transport in the $z$ direction.

### 4.2.4 Magnon motion in the presence of pseudo-magnetic field

In Section 4.2.2, we have shown that magnon bands can be Landau-quantized by a chiral pseudo-electric field $\boldsymbol{e}^\eta$ induced by a static twist, under which the magnon Hamiltonian is modified by the Peierls substitution $\boldsymbol{q} \to \boldsymbol{q} + \frac{e}{\hbar}\frac{1}{ec^2}\boldsymbol{e}^\eta \times \boldsymbol{\mu}$. Therefore, by comparing to Eq. 4.25, the magnon equation of motion in the presence of $\boldsymbol{e}^\eta$ and $\boldsymbol{B}$ can be immediately written down as

$$\hbar\frac{d\boldsymbol{k}}{dt} = \nabla(\boldsymbol{\mu}\cdot\boldsymbol{B}) - \frac{\partial}{\partial t}\frac{1}{c^2}\boldsymbol{\mu}\times\boldsymbol{e}^\eta + \frac{1}{c^2}\boldsymbol{v}\times[\nabla\times(\boldsymbol{\mu}\times\boldsymbol{e}^\eta)]. \tag{4.26}$$

Because $\boldsymbol{e}^\eta$ field has exactly the same spacetime dependence as the inhomogeneous electric field $\boldsymbol{E}$ except for the chiral nature, our analysis for $\boldsymbol{E}$ in Section 4.2.3 can be transplanted to $\boldsymbol{e}^\eta$. Therefore we argue that magnons cannot be pumped by the pseudo-electric field induced by a static twist deformation. For this reason, in order to pump magnons, we resort to a *dynamic* deformation.

We consider a dynamic uniaxial strain whose only nonzero strain tensor component is $u_{33}$. Such a strain can be generated by the displacement field $\boldsymbol{u} = u_z(z,t)\hat{z}$. The knowledge of the explicit form of $u_z$ is not necessary for our purpose. Experimentally, a legitimate $u_z$ may be obtained by applying ultrasonic sound waves along the $z$ direction. Based on our experience of the overlap integral substitution (Eq. 1.23) in Section 1.3, under this uniaxial strain $u_{33}$, we need to modify the exchange integrals whose arguments has nonzero $z$ components. Such exchange integrals are $J_A$, $J_B$, and the six $J_2$'s illustrated in Fig. 4.5. The substitutions are

$$\begin{aligned} J_A &\to J_A(1-u_{33}),\\ J_B &\to J_B(1-u_{33}),\\ J_2 &\to J_2(1-\tfrac{1}{2}u_{33}), \end{aligned}$$

under which an extra term enters the Bloch Hamiltonian (Eq. 4.7),

$$\begin{aligned} \delta\mathcal{H}^{\boldsymbol{b}}_{\boldsymbol{k}} = {}& u_{33}J_2S\cos k_za\sum_i\cos(\boldsymbol{k}\cdot\boldsymbol{\alpha}_i)\sigma^x - u_{33}J_2S\cos k_za\sum_i\sin(\boldsymbol{k}\cdot\boldsymbol{\alpha}_i)\sigma^y\\ &- u_{33}J_-S(1-\cos k_za)\sigma^z - u_{33}[3J_2 + J_+(1-\cos k_za)]S\sigma^0. \end{aligned} \tag{4.27}$$

In the vicinity of the Weyl points $\boldsymbol{k}^\eta_W$, the Bloch Hamiltonian under the

uniaxial deformation becomes

$$\mathcal{H}_{\boldsymbol{k}_W^\eta+\boldsymbol{q}} + \delta\mathcal{H}^{\boldsymbol{b}}_{\boldsymbol{k}_W^\eta+\boldsymbol{q}} \approx \mathcal{H}_{\boldsymbol{k}_W^\eta} + \hbar v_0^\eta\Big(q_z + \frac{e}{\hbar}a^\eta_{D,z}\Big)\sigma^0 + \sum_i \hbar v_i^\eta\Big(q_i + \frac{e}{\hbar}a^\eta_{D,i}\Big)\sigma^i - 3J_2Su_{33}\sigma^0. \quad (4.28)$$

Similar to the static twist (Eq. 4.18), the dynamic uniaxial strain also shifts the momentum through the minimal substitution $\boldsymbol{q} \to \boldsymbol{q} + \frac{e}{\hbar}\boldsymbol{a}_D^\eta$, where the strain-induced vector potential reads

$$\boldsymbol{a}_D^\eta = -\eta\frac{\hbar}{ea}\frac{1-\cos Qa}{\sin Qa}(0,0,u_{33}). \quad (4.29)$$

Similar to the its static counterpart $\boldsymbol{a}_S^\eta$, this dynamic strain-induced vector potential $\boldsymbol{a}_D^\eta$ is also chiral. However, it is critically important to note that this vector potential cannot be interpreted as the vector potential of a pseudo-electric field because $\nabla\times\boldsymbol{a}_D^\eta = 0$. In fact, $\boldsymbol{a}_D^\eta$ is associated with a chiral pseudo-magnetic field. To see this, by replicating the derivation in Section 4.2.3, we first write down the equation of motion for magnons under the dynamic uniaxial strain

$$\hbar\frac{d\boldsymbol{k}}{dt} = e\frac{\partial\boldsymbol{a}_D^\eta}{\partial t} - e\boldsymbol{v}\times(\nabla\times\boldsymbol{a}_D^\eta) + \nabla(3J_2Su_{33}). \quad (4.30)$$

The extra non-chiral gradient term $\nabla(3J_2Su_{33})$ appears because the dynamic strain induces in the Hamiltonian an on-site term $3J_2Su_{33}\sigma^0$, which cannot be characterized by the minimal substitution. However, in systems where $J_2$ is reasonably small, namely $J_2S \ll \hbar c_s/a$ ($c_s$ is the speed of sound in the nanowire), this non-chiral term becomes negligible relative to the chiral time-derivative term[9]. We concentrate on such systems in the remainder of this paper. Therefore, considering the fact that $\nabla\times\boldsymbol{a}_D^\eta = 0$, the $z$ component of Eq. 4.30 is reduced to

$$\hbar\frac{dk_z}{dt} = e\frac{\partial a^\eta_{D,z}}{\partial t} = \partial_z(\boldsymbol{\mu}\cdot\boldsymbol{b}^\eta), \quad (4.31)$$

where

$$\boldsymbol{b}^\eta = \frac{\boldsymbol{\mu}}{\mu^2}\int dz e\frac{\partial a^\eta_{D,z}}{\partial t} = \frac{\eta}{g\mu_B}\frac{\hbar}{a}\frac{1-\cos Qa}{\sin Qa}\int dz\frac{\partial u_{33}}{\partial t}\hat{z} \quad (4.32)$$

[9]In systems where the non-chiral gradient term is no longer negligible, its effects are similar to those of a inhomogeneous magnetic field $\boldsymbol{B}$. Therefore, the resulting magnon quantum anomalies will be a combination of purely magnetic field induced anomalies and purely chiral pseudo-magnetic field induced anomalies.

can be understood as an inhomogeneous pseudo-magnetic field. Due to its chiral nature, $\boldsymbol{b}^\eta$ pumps magnons oppositely in the vicinity of the two Weyl points.

To sum up, a dynamic uniaxial strain can induce a chiral pseudo-magnetic field, accompanied by a non-chiral field whose effects can be neglected for reasonably small $J_2$. The pseudo-magnetic field pumps magnons in opposite directions $\pm z$ at the two Weyl points. Therefore, it may also result in magnon quantum anomalies as will be detailed in Section 4.3.2 and Section 4.3.3. In the meanwhile, the static torsional strain only provides the needed Landau quantization and does not affect the magnon transport in the $z$ direction.

## 4.3 Magnon quantum anomalies and the anomalous transport

In Section 4.2, we have found that magnon bands can be Landau-quantized by either an inhomogeneous transverse electric field $\boldsymbol{E}$ or a chiral pseudo-electric field $\boldsymbol{e}^\eta$ induced by a static twist. To drive the magnons along the zeroth Landau levels, we may use either an inhomogeneous longitudinal magnetic field $\boldsymbol{B}$, or a chiral pseudo-magnetic field $\boldsymbol{b}^\eta$ induced by a dynamic uniaxial strain. In this section, we will show that each of the four possible combinations of an electric/pseudo-electric field and a magnetic/pseudo-magnetic field gives rise to a magnon quantum anomaly. We will derive the anomaly equations and discuss the associated anomalous spin and heat transport.

### 4.3.1 Magnon chiral anomaly due to electric and magnetic fields

In the present section, for completeness, we will derive the magnon chiral anomaly and the associated anomalous spin and heat currents in the presence of $\boldsymbol{E}$ and $\boldsymbol{B}$, though these have been briefly mentioned in Ref. [25].

We consider a Weyl ferromagnet nanowire aligned in the $z$ direction under the electric field $\boldsymbol{E} = (\frac{1}{2}\mathcal{E}x, \frac{1}{2}\mathcal{E}y, 0)$, whose magnon Landau levels are illustrated in Fig. 4.4. The left and right ends are attached to magnon reservoirs subjected to a uniform magnetic field $\boldsymbol{B}_0 = B_0\hat{z}$. Magnons will then attain a Zeeman energy $-\boldsymbol{\mu}\cdot\boldsymbol{B}_0 = g\mu_B B_0$ and the magnon population edge, which is originally located in the band minima, can be lifted up to the gap of the first Landau levels (Fig. 4.7(a)) by a suitable $B_0$. This is an analog to putting the chemical potential in the gap of Landau levels in Weyl

semimetals [25, 173]. While electrons contributing to ballistic transport can have energies above or below the chemical potential, magnons must reside above the population edge $g\mu_B B_0$ in the magnon reservoirs to participate in ballistic transport. Then a spatially varying magnetic field $\boldsymbol{B} = B_z\hat{z}$ is overlaid, where $B_z$ has a nonzero gradient $\partial_z B_z = \mathcal{B}$. Based on Eq. 4.21, the magnons begin to propagate along the Landau levels in the $-z$ direction according to semiclassical equation of motion $q_z(t) = q_z(0) - g\mu_B \int_0^t \mathcal{B}dt'/\hbar$. Thus the magnons originally on the left zeroth Landau level will be pumped to the right zeroth Landau level across the Brillouin zone boundary, which results in a chirality imbalance, a key feature of the magnon chiral anomaly.

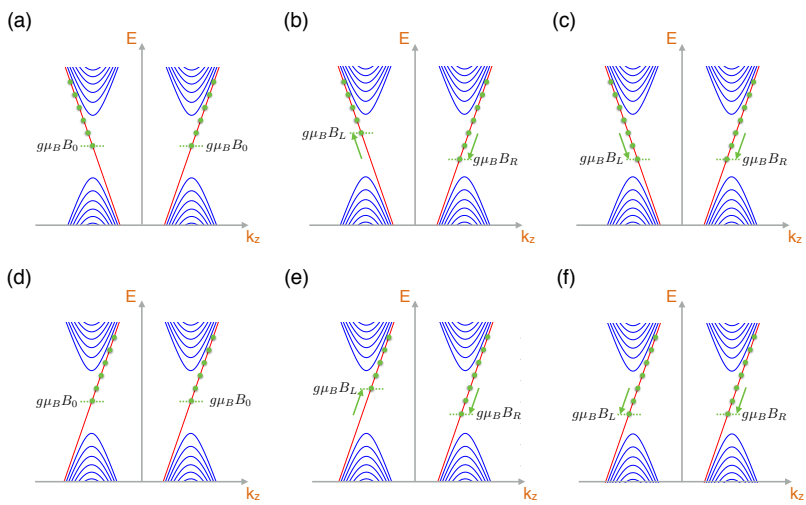


Figure 4.7: Schematic plot of the magnon band structures and distributions in various quantum anomalies of a Weyl ferromagnet, which is in contact with two magnon reservoirs in a uniform magnetic field $\boldsymbol{B}_0$. (a)-(c) Magnon Dirac-Landau levels due to an inhomogeneous electric field. (d)-(f) Magnon Dirac-Landau levels due to a strain-induced pseudo-electric field. (a, d) Magnon distributions in the absence of pumping. (b, e) Magnon chiral anomaly with chirality imbalance created by ordinary magnetic field pumping in (b) and by pseudo-magnetic field pumping in (e). (c, f) Magnon heat anomaly with magnon concentration variation created by pseudo-magnetic field pumping in (c) and by ordinary magnetic field pumping in (f). For all panels, only the distributions (green dots) on the zeroth Landau levels (red) are plotted. In principle, magnons can occupy all bands above the population edges provided that the relaxation time is sufficiently long.

During this pumping process, the magnon population edge is gradually elevated (lowered) on the left (right) zeroth Landau level (Fig. 4.7(b)). The difference between the left and right magnon population edges is analogous to the chiral chemical potential in Weyl semimetals. Here we will see the difference in magnon population edges as a magnetic field bias $B_5 \ll B_0$ such that the left (right) Weyl cone experiences a magnetic field $B_L = B_0 + B_5$ ($B_R = B_0 - B_5$). From the semiclassical equation of motion, we obtain

$$B_5 = -\frac{\hbar|v_z^\eta| \int dq_z}{g\mu_B} = \int_0^t \mathcal{B}|v_z^\eta|dt'. \tag{4.33}$$

We now derive the chiral anomaly equation for magnons. The magnon concentration variation on the right zeroth Landau level can be written down as a Taylor series

$$\begin{aligned} n_R^{\boldsymbol{E},\boldsymbol{B}} &= \int_{g\mu_B B_R}^{g\mu_B B_0} g_{\boldsymbol{E}}(\epsilon) n_B(\epsilon) d\epsilon \\ &= \frac{n_B(g\mu_B B_0)}{4\pi^2 l_E^2} \frac{g\mu_B B_5}{\hbar|v_z^\eta|} - \sum_{n=1} \frac{n_B^{(n)}(g\mu_B B_0)}{(n+1)!} \frac{(-g\mu_B B_5)^{n+1}}{4\pi^2 l_E^2 \hbar|v_z^\eta|}, \end{aligned} \tag{4.34}$$

where $g_{\boldsymbol{E}}(\epsilon) = \frac{1}{2\pi l_E^2} \frac{1}{2\pi\hbar|v_z^\eta|}$ is the density of states with the electric length $l_E = (-\hbar c^2/g\mu_B\mathcal{E})^{1/2}$ [10], and $n_B(\epsilon) = (e^{\epsilon/k_B T} - 1)^{-1}$ is the magnon distribution function. Similarly, the magnon concentration variation on the left zeroth Landau level is

$$\begin{aligned} n_L^{\boldsymbol{E},\boldsymbol{B}} &= \int_{g\mu_B B_L}^{g\mu_B B_0} g_{\boldsymbol{E}}(\epsilon) n_B(\epsilon) d\epsilon \\ &= -\frac{n_B(g\mu_B B_0)}{4\pi^2 l_E^2} \frac{g\mu_B B_5}{\hbar|v_z^\eta|} - \sum_{n=1} \frac{n_B^{(n)}(g\mu_B B_0)}{(n+1)!} \frac{(g\mu_B B_5)^{n+1}}{4\pi^2 l_E^2 \hbar|v_z^\eta|}. \end{aligned} \tag{4.35}$$

In the low bias limit $g\mu_B B_5 \ll k_B T$, the net chirality pumping rate can be well approximated as

$$\frac{d\rho_5^{\boldsymbol{E},\boldsymbol{B}}}{dt} = \chi_R \frac{dn_R^{\boldsymbol{E},\boldsymbol{B}}}{dt} + \chi_L \frac{dn_L^{\boldsymbol{E},\boldsymbol{B}}}{dt} \approx -\frac{g^2\mu_B^2}{2\pi^2\hbar^2 c^2} n_B(g\mu_B B_0)\mathcal{E}\mathcal{B}, \tag{4.36}$$

where, as in Eq. 4.10, $\chi_R = +1$ and $\chi_L = -1$. More generally, for arbitrarily oriented $\boldsymbol{E}$ and $\boldsymbol{B}$, the magnon chiral anomaly equation reads

$$\frac{d\rho_5^{\boldsymbol{E},\boldsymbol{B}}}{dt} + \nabla \cdot \boldsymbol{j}_5^{\boldsymbol{E},\boldsymbol{B}} \approx \frac{n_B(g\mu_B B_0)}{2\pi^2\hbar^2 c^2} \nabla(\boldsymbol{\mu} \cdot \boldsymbol{B}) \cdot [\nabla \times (\boldsymbol{E} \times \boldsymbol{\mu})]. \tag{4.37}$$

[10] The minus sign comes from the assumption that $\mathrm{sgn}(g\mathcal{E}) = -1$ in Section 4.2.1

Such a magnon chiral anomaly is dual to the electron chiral anomaly [56–58]. It is worth noting that Eq. 4.37 is true to the first order in $B_5$; at this order the number of magnons pumped out of the left zeroth Landau level is approximately equal to the number of magnons pumped into the right zeroth Landau level $-n_L \approx n_R$. However, at the second order in $B_5$, we have

$$\begin{aligned} n_R^{\boldsymbol{E},\boldsymbol{B}} + n_L^{\boldsymbol{E},\boldsymbol{B}} &= -\sum_{n=1} \frac{n_B^{(n)}(g\mu_B B_0)}{(n+1)!} \frac{(g\mu_B B_5)^{n+1}[1+(-1)^{n+1}]}{4\pi^2 l_E^2 \hbar |v_z^\eta|} \\ &\approx \frac{e^{g\mu_B B_0/k_B T}}{(e^{g\mu_B B_0/k_B T}-1)^2} \frac{1}{k_B T} \frac{(g\mu_B B_5)^2}{4\pi^2 l_E^2 \hbar |v_z^\eta|} > 0, \end{aligned} \tag{4.38}$$

indicating that the magnon number is not conserved, because magnons are bosonic collective excitations rather than fundamental particles. From another point of view, if the magnon number were conserved, higher-energy magnons pumped out of the left zeroth Landau level would result in the same number of lower-energy magnons populating the right zeroth Landau level, and the magnon distribution in Fig. 4.7(b) would have a lower total energy than that in Fig. 4.7(a), making the pumping process spontaneous. However, magnon pumping actually requires energy injection by EM fields. Explicitly, the energy injection into the right zeroth Landau level is

$$\begin{aligned} U_R^{\boldsymbol{E},\boldsymbol{B}} &= \int_{g\mu_B B_R}^{+\infty} \epsilon g_{\boldsymbol{E}}(\epsilon) n_B(\epsilon) d\epsilon - \int_{g\mu_B B_0}^{+\infty} \epsilon g_{\boldsymbol{E}}(\epsilon) n_B(\epsilon) d\epsilon \\ &= \frac{1}{4\pi^2 l_E^2 \hbar |v_z^\eta|} \Bigg\{ \frac{1}{2} n_B(g\mu_B B_0) g^2 \mu_B^2 (2B_0 B_5 - B_5^2) \\ &\quad - \sum_{n=1} \frac{n_B^{(n)}(g\mu_B B_0)}{n!} \frac{g\mu_B B_0 (-g\mu_B B_5)^{n+1}}{n+1} \\ &\quad - \sum_{n=1} \frac{n_B^{(n)}(g\mu_B B_0)}{n!} \frac{(-g\mu_B B_5)^{n+2}}{n+2} \Bigg\} \\ &\approx \frac{1}{4\pi^2 l_E^2 \hbar |v_z^\eta|} \Bigg\{ \frac{1}{2} n_B(g\mu_B B_0) g^2 \mu_B^2 (2B_0 B_5 - B_5^2) \\ &\quad - n_B'(g\mu_B B_0) \frac{g\mu_B B_0 (-g\mu_B B_5)^2}{2} \Bigg\}, \end{aligned} \tag{4.39}$$

where the approximation is still taken in the low bias limit $g\mu_B B_5 \ll k_B T$. Similarly, the energy depletion on the left zeroth Landau level can be easily

written down by making the substitution $-B_5 \to +B_5$,

$$U_L^{\boldsymbol{E},\boldsymbol{B}} = \int_{g\mu_B B_L}^{+\infty} \epsilon g_{\boldsymbol{E}}(\epsilon) n_B(\epsilon) d\epsilon - \int_{g\mu_B B_0}^{+\infty} \epsilon g_{\boldsymbol{E}}(\epsilon) n_B(\epsilon) d\epsilon$$
$$\approx \frac{1}{4\pi^2 l_E^2 \hbar |v_z^\eta|} \left\{ \frac{1}{2} n_B(g\mu_B B_0) g^2 \mu_B^2 (-2B_0 B_5 - B_5^2) - n_B'(g\mu_B B_0) \frac{g\mu_B B_0 (g\mu_B B_5)^2}{2} \right\}. \quad (4.40)$$

And the total energy variation

$$U_R^{\boldsymbol{E},\boldsymbol{B}} + U_L^{\boldsymbol{E},\boldsymbol{B}} = -\frac{1}{4\pi^2 l_E^2 \hbar |v_z^\eta|} n_B(g\mu_B B_0)(g\mu_B B_5)^2 - \frac{1}{4\pi^2 l_E^2 \hbar |v_z^\eta|} n_B'(g\mu_B B_0) g\mu_B B_0 (g\mu_B B_5)^2$$
$$= -\frac{(g\mu_B B_5)^2}{4\pi^2 l_E^2 \hbar |v_z^\eta|} \frac{d}{d\epsilon} \epsilon n_B(\epsilon) \Big|_{g\mu_B B_0} > 0 \quad (4.41)$$

is indeed positive as expected, because $\epsilon n_B(\epsilon)$ is a decreasing function. Therefore, in the magnon pumping process, higher-energy magnons pumped out of the left zeroth Landau level should result in more lower-energy magnons on the right zeroth Landau level with the assistance of electromagnetic energy injection. The total energy after pumping will then increase.

Before we leave this section, we calculate the anomalous spin and heat currents due to the magnon chiral anomaly. For the Weyl ferromagnet we considered, the spin and heat currents are given by the Landauer-Büttiker formalism [173],

$$J_{\text{spin}}^{\boldsymbol{E},\boldsymbol{B}} = -\int_{g\mu_B B_R}^{+\infty} \hbar g_{\boldsymbol{E}}(\epsilon) n_B(\epsilon) v_R^{\boldsymbol{E}}(\epsilon) d\epsilon - \int_{g\mu_B B_L}^{+\infty} \hbar g_{\boldsymbol{E}}(\epsilon) n_B(\epsilon) v_L^{\boldsymbol{E}}(\epsilon) d\epsilon, \quad (4.42)$$

$$J_{\text{heat}}^{\boldsymbol{E},\boldsymbol{B}} = \int_{g\mu_B B_R}^{+\infty} \epsilon g_{\boldsymbol{E}}(\epsilon) n_B(\epsilon) v_R^{\boldsymbol{E}}(\epsilon) d\epsilon + \int_{g\mu_B B_L}^{+\infty} \epsilon g_{\boldsymbol{E}}(\epsilon) n_B(\epsilon) v_L^{\boldsymbol{E}}(\epsilon) d\epsilon, \quad (4.43)$$

where the magnon drifting velocity in the zeroth Landau levels are $v_R^{\boldsymbol{E}}(\epsilon) = \frac{1}{\hbar}\frac{d\epsilon}{dq_z}|_R$ and $v_L^{\boldsymbol{E}}(\epsilon) = \frac{1}{\hbar}\frac{d\epsilon}{dq_z}|_L$. Further simplification gives the spin and heat currents as

$$J_{\text{spin}}^{\boldsymbol{E},\boldsymbol{B}} = -\hbar |v_z^\eta| (n_R^{\boldsymbol{E},\boldsymbol{B}} - n_L^{\boldsymbol{E},\boldsymbol{B}}) \approx \hbar \frac{g^2 \mu_B^2}{2\pi^2 \hbar^2 c^2} n_B(g\mu_B B_0) B_5 \mathcal{E}, \quad (4.44)$$

$$J_{\text{heat}}^{\boldsymbol{E},\boldsymbol{B}} = |v_z^\eta|(U_R^{\boldsymbol{E},\boldsymbol{B}} - U_L^{\boldsymbol{E},\boldsymbol{B}}) \approx -\frac{g^3\mu_B^3}{2\pi^2\hbar^2c^2} n_B(g\mu_B B_0) B_0 B_5 \mathcal{E}, \tag{4.45}$$

where $v_R^{\boldsymbol{E}}(\epsilon) = -v_L^{\boldsymbol{E}}(\epsilon) = |v_z^\eta|$ is used. As discussed in Section 4.2.3, the electric field $\boldsymbol{E}$ for magnons is dual to the vector potential $\boldsymbol{A}$ for electrons; the electric field gradient $\mathcal{E}$ thus plays the role of the magnetic field for electrons. $g\mu_B B_5$ measures the difference of the magnon population edges, and is therefore dual to the electron chiral chemical potential $\mu_5$. Consequently, the anomalous spin and heat currents of the magnon chiral anomaly is akin to the chiral magnetic current [62, 63] of the electron chiral anomaly. We will refer to Eqs. 4.44, 4.45 as the "chiral electric effect."

### 4.3.2 Magnon chiral anomaly due to pseudo-electric and pseudo-magnetic fields

We now consider another possibility of implementing the magnon chiral anomaly. We use a chiral electric field $\boldsymbol{e}^\eta = \eta\boldsymbol{e} = (\frac{1}{2}\eta\varepsilon x, \frac{1}{2}\eta\varepsilon y, 0)$ induced by a static torsional strain, whose Landau levels are illustrated in Fig. 4.6 with both zeroth Landau levels being right-moving. The twisted Weyl ferromagnet is aligned in the $z$ direction and in contact with magnon reservoirs, which will lift the magnon population edge to $-\boldsymbol{\mu}\cdot\boldsymbol{B}_0 = g\mu_B B_0$. As with the case of an electric field $\boldsymbol{E}$, in principle, the magnon population edge can be tuned into the gap of the first Landau levels (Fig. 4.7(d)) by a proper choice of $B_0$. Then a chiral magnetic field $\boldsymbol{b}^\eta = \eta\boldsymbol{b} = \eta b_z\hat{z}$, which is induced by a dynamic uniaxial strain, is overlaid, where $b_z$ has a nonzero gradient $\partial_z b_z = \beta$. Based on Eq. 4.31, the magnons are pumped through Landau levels according to the semiclassical equation of motion $q_z(t) = q_z(0) - \eta g\mu_B \int_0^t \beta t'/\hbar$. Thus magnons originally on the left zeroth Landau level are pumped into the right zeroth Landau level, giving rise to a magnon chiral anomaly.

Unlike the magnon pumping due to $\boldsymbol{B}$, magnons on different Weyl cones are pumped oppositely by the chiral magnetic field $\boldsymbol{b}^\eta$ such that the magnon population edge on left (right) zeroth Landau level is elevated (lowered) as illustrated in Fig. 4.7(e). The difference between magnon population edges can be characterized by a magnetic field bias $b_5 \ll B_0$ under which the left (right) Weyl cone experiences a magnetic field $b_L = B_0 + b_5$ ($b_R = B_0 - b_5$). According to the semiclassical equation of motion, we have

$$b_5 = -\frac{\hbar|v_z^\eta|\eta\int dq_z}{g\mu_B} = \int_0^t \beta|v_z^\eta|dt'. \tag{4.46}$$

To derive the chiral anomaly due to $\boldsymbol{e}^\eta$ and $\boldsymbol{b}^\eta$, we need to know the magnon

concentration variations on both zeroth Landau levels, which can be directly written down by referring to Eqs. 4.34, 4.35 as

$$n_R^{\boldsymbol{e},\boldsymbol{b}} = \frac{n_B(g\mu_B B_0)}{4\pi^2 l_e^2}\frac{g\mu_B b_5}{\hbar|v_z^\eta|} - \sum_{n=1}\frac{n_B^{(n)}(g\mu_B B_0)}{(n+1)!}\frac{(-g\mu_B b_5)^{n+1}}{4\pi^2 l_e^2\hbar|v_z^\eta|}, \tag{4.47}$$

$$n_L^{\boldsymbol{e},\boldsymbol{b}} = -\frac{n_B(g\mu_B B_0)}{4\pi^2 l_e^2}\frac{g\mu_B b_5}{\hbar|v_z^\eta|} - \sum_{n=1}\frac{n_B^{(n)}(g\mu_B B_0)}{(n+1)!}\frac{(g\mu_B b_5)^{n+1}}{4\pi^2 l_e^2\hbar|v_z^\eta|}, \tag{4.48}$$

where the pseudo-electric length $l_e = (-\hbar c^2/g\mu_B\varepsilon)^{1/2}$. We assume $\mathrm{sgn}(g\varepsilon) = -1$ in order to be parallel to the assumption that $\mathrm{sgn}(g\mathcal{E}) = -1$ (see Section 4.2.1). In the low bias limit $g\mu_B b_5 \ll k_B T$, the chirality pumping rate is

$$\frac{d\rho_5^{\boldsymbol{e},\boldsymbol{b}}}{dt} = \chi_R\frac{dn_R^{\boldsymbol{e},\boldsymbol{b}}}{dt} + \chi_L\frac{dn_L^{\boldsymbol{e},\boldsymbol{b}}}{dt} \approx -\frac{g^2\mu_B^2}{2\pi^2\hbar^2c^2}n_B(g\mu_B B_0)\varepsilon\beta. \tag{4.49}$$

In the more general case, the magnon chiral anomaly equation can be written as

$$\frac{d\rho_5^{\boldsymbol{e},\boldsymbol{b}}}{dt} + \nabla\cdot j_5^{\boldsymbol{e},\boldsymbol{b}} \approx \frac{n_B(g\mu_B B_0)}{2\pi^2\hbar^2c^2}\nabla(\boldsymbol{\mu}\cdot\boldsymbol{b})\cdot[\nabla\times(\boldsymbol{e}\times\boldsymbol{\mu})], \tag{4.50}$$

which is parallel to Eq. 4.37. Similarly, this anomaly equation only contains the leading order terms in Eqs. 4.47, 4.48. More rigorously, $n_R^{\boldsymbol{e},\boldsymbol{b}} + n_L^{\boldsymbol{e},\boldsymbol{b}} > 0$; otherwise the magnon pumping will become spontaneous. This can also be confirmed by checking the energy variations on both zeroth Landau levels. By referring to Eqs. 4.39, 4.40, the estimated energy variations on the zeroth Landau levels are

$$U_R^{\boldsymbol{e},\boldsymbol{b}} \approx \frac{1}{4\pi^2 l_e^2\hbar|v_z^\eta|}\Big\{\frac{1}{2}n_B(g\mu_B B_0)g^2\mu_B^2[2B_0b_5 - b_5^2] - n_B'(g\mu_B B_0)\frac{g\mu_B B_0(-g\mu_B b_5)^2}{2}\Big\}, \tag{4.51}$$

$$U_L^{\boldsymbol{e},\boldsymbol{b}} \approx \frac{1}{4\pi^2 l_e^2\hbar|v_z^\eta|}\Big\{\frac{1}{2}n_B(g\mu_B B_0)g^2\mu_B^2[-2B_0b_5 - b_5^2] - n_B'(g\mu_B B_0)\frac{g\mu_B B_0(g\mu_B b_5)^2}{2}\Big\}. \tag{4.52}$$

$U_R^{\boldsymbol{e},\boldsymbol{b}} + U_L^{\boldsymbol{e},\boldsymbol{b}} > 0$, indicating energy injection due to the pseudo-EM fields during the pumping process.

We now derive the anomalous spin and heat currents resulting from the chiral anomaly due to $\boldsymbol{e}^\eta$ and $\boldsymbol{b}^\eta$. First, it is important to note that before the chiral magnetic field $\boldsymbol{b}^\eta$ is switched on, there must be an equal number of right-moving magnons and left-moving magnons; otherwise the net spin/heat current will be nonzero in the absence of a driving force. As demonstrated in Section 4.2.2, under the chiral electric field $\boldsymbol{e}^\eta$, the bulk only hosts right-moving magnons while the left-moving magnons are localized at the surface. Therefore, the bulk spin/heat current must be balanced by the surface spin/heat current when $\boldsymbol{b}^\eta = 0$. Explicitly, we have

$$\mathcal{J}_{\text{spin}}^{\text{bulk}} = -\int_{g\mu_B B_0}^{+\infty} \hbar g_{\boldsymbol{e}}(\epsilon) n_B(\epsilon) v_R^{\boldsymbol{e}}(\epsilon) d\epsilon - \int_{g\mu_B B_0}^{+\infty} \hbar g_{\boldsymbol{e}}(\epsilon) n_B(\epsilon) v_L^{\boldsymbol{e}}(\epsilon) d\epsilon = -\mathcal{J}_{\text{spin}}^{\text{surface}}, \quad (4.53)$$

$$\mathcal{J}_{\text{heat}}^{\text{bulk}} = \int_{g\mu_B B_0}^{+\infty} \epsilon g_{\boldsymbol{e}}(\epsilon) n_B(\epsilon) v_R^{\boldsymbol{e}}(\epsilon) d\epsilon + \int_{g\mu_B B_0}^{+\infty} \epsilon g_{\boldsymbol{e}}(\epsilon) n_B(\epsilon) v_L^{\boldsymbol{e}}(\epsilon) d\epsilon = -\mathcal{J}_{\text{heat}}^{\text{surface}}, \quad (4.54)$$

where the density of states is $g_{\boldsymbol{e}}(\epsilon) = \frac{1}{2\pi l_e^2} \frac{1}{2\pi\hbar|v_z^\eta|}$ and the velocities are $v_R^{\boldsymbol{e}} = v_L^{\boldsymbol{e}} = |v_z^\eta|$. To verify our argument, we have numerically calculated the spatial distribution of magnon spin and heat currents on the cross section of the Weyl ferromagnet nanowire illustrated in the right panel of Fig. 4.3(a). As shown in Fig. 4.8(b), the spin current in the bulk of the rectangular cross section (Fig. 4.3(b)) propagates along the $-z$ direction while the spin current on the edges of the cross section propagates along the $+z$ direction. On the other hand, the bulk heat current of the rectangular cross section propagates along the $+z$ direction while the edge heat current propagates along the $-z$ direction, as illustrated in Fig. 4.8(c). We have carefully evaluated the total spin and heat currents through the rectangular cross section under various numerical settings, and find that both currents are vanishingly small when the gradient of $b_z$ vanishes, $\beta = 0$. We further examine a Weyl ferromagnet nanowire with an almost circular cross section, whose bulk-surface separation for spin/heat transport is exhibited again in Fig. 4.8 (e) and (f).

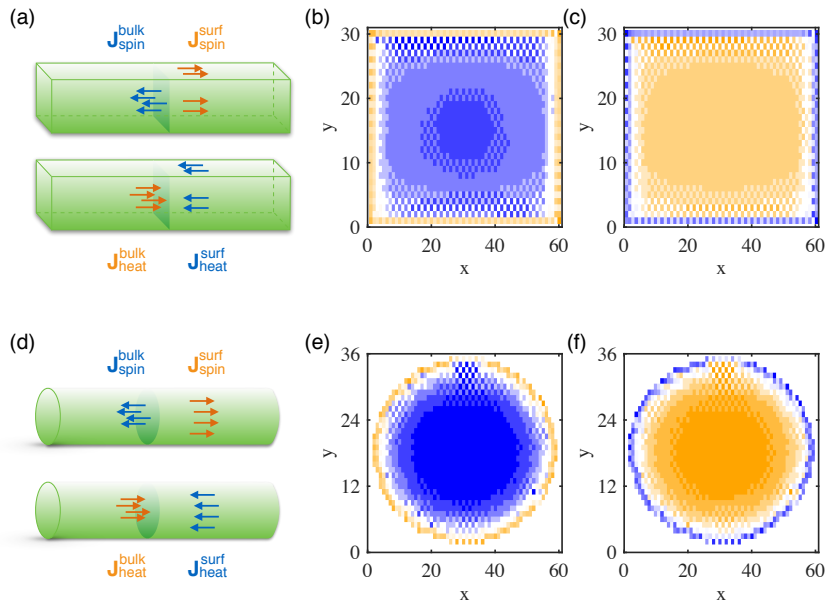


Figure 4.8: Bulk-surface separation for the twisted Weyl ferromagnet nanowire. (a) Schematic plot of a Weyl ferromagnet nanowire with a rectangular cross section. The spin current propagates along the $-z$ direction in the bulk but along the $+z$ direction on the surface, while the heat current propagates along the $+z$ direction in the bulk but along the $-z$ direction on the surface. (b) Spatially resolved spin current on the cross section of the cuboid Weyl ferromagnet nanowire. (c) Spatially resolved heat current on the cross section of the cuboid Weyl ferromagnet nanowire. The directions of currents are color coded with blue (orange) representing $-z$ ($+z$). (d)-(f) Same as (a)-(c) but for a Weyl ferromagnet nanowire with an (almost) circular cross section. The total spin current on the rectangular (circular) cross section is $0.002DS$ ($0.0001DS$) while the total heat current on the rectangular (circular) cross section is $-0.0473D^2S^2/\hbar$ ($-0.0018D^2S^2/\hbar$).

Then, we switch on the chiral pseudo-magnetic field $\boldsymbol{b}^\eta$, and the magnons begin to propagate along the Landau levels, giving rise to net anomalous spin and heat currents

$$J^{\boldsymbol{e},\boldsymbol{b}}_{\text{spin}} = -\int_{g\mu_B b_R}^{+\infty} \hbar g_{\boldsymbol{e}}(\epsilon) n_B(\epsilon) v^{\boldsymbol{e}}_R(\epsilon) d\epsilon - \int_{g\mu_B b_L}^{+\infty} \hbar g_{\boldsymbol{e}}(\epsilon) n_B(\epsilon) v^{\boldsymbol{e}}_L(\epsilon) d\epsilon - \mathcal{J}^{\text{bulk}}_{\text{spin}}, \tag{4.55}$$

$$J_{\text{heat}}^{\boldsymbol{e},\boldsymbol{b}} = \int_{g\mu_B b_R}^{+\infty} \epsilon g_{\boldsymbol{e}}(\epsilon) n_B(\epsilon) v_R^{\boldsymbol{e}}(\epsilon) d\epsilon + \int_{g\mu_B b_L}^{+\infty} \epsilon g_{\boldsymbol{e}}(\epsilon) n_B(\epsilon) v_L^{\boldsymbol{e}}(\epsilon) d\epsilon - \mathcal{J}_{\text{heat}}^{\text{bulk}}. \tag{4.56}$$

Again, in the low bias limit $g\mu_B b_5 \ll k_B T$, we obtain the spin and heat currents to the lowest non-vanishing order

$$J_{\text{spin}}^{\boldsymbol{e},\boldsymbol{b}} = -\hbar |v_z^\eta| (n_R^{\boldsymbol{e},\boldsymbol{b}} + n_L^{\boldsymbol{e},\boldsymbol{b}}) \approx -\hbar \frac{g^3 \mu_B^3}{4\pi^2 \hbar^2 c^2} n_B'(g\mu_B B_0) b_5^2 \varepsilon, \tag{4.57}$$

$$J_{\text{heat}}^{\boldsymbol{e},\boldsymbol{b}} = |v_z^\eta| (U_R^{\boldsymbol{e},\boldsymbol{b}} + U_L^{\boldsymbol{e},\boldsymbol{b}}) \approx \frac{g^3 \mu_B^3}{4\pi^2 \hbar^2 c^2} \Big[ n_B(g\mu_B B_0) + n_B'(g\mu_B B_0) g\mu_B B_0 \Big] b_5^2 \varepsilon. \tag{4.58}$$

Unlike the magnon chiral electric spin and heat currents Eqs. 4.44, 4.45, which are proportional to the magnetic field bias $B_5$, the anomalous spin and heat currents due to $(\boldsymbol{e}^\eta, \boldsymbol{b}^\eta)$ are quadratic in the pseudo-magnetic field bias $b_5$, because magnons on both zeroth Landau levels have the identical velocity. These small but nonzero spin and heat currents reflect the non-conservation of magnon number, in contrast to the chiral anomaly of electrons with pure strain-induced pseudo-EM fields, where the anomalous current is exactly zero due to charge conservation.

### 4.3.3 Magnon heat anomaly due to electric and pseudo-magnetic fields

Besides the chiral anomalies discussed in Section 4.3.1 and Section 4.3.2, Weyl magnons can exhibit another type of quantum anomaly in which the thermal energy in the bulk is not conserved. In this section, we will quantitatively characterize such a magnon "heat anomaly" in the presence of an inhomogeneous electric field $\boldsymbol{E}$ and an inhomogeneous pseudo-magnetic field $\boldsymbol{b}^\eta$.

We again consider a Weyl ferromagnet nanowire subjected to an inhomogeneous electric field $\boldsymbol{E} = (\frac{1}{2}\mathcal{E}x, \frac{1}{2}\mathcal{E}y, 0)$. The two ends of the wire are attached to magnon reservoirs with a uniform magnetic field $\boldsymbol{B}_0 = B_0\hat{z}$ such that the magnon population edge $g\mu_B B_0$ is located in the gap of the first Landau levels (Fig. 4.7(a)). Rather than using an inhomogeneous magnetic field $\boldsymbol{B}$ as is the case in Section 4.3.1, we drive magnons with an inhomogeneous pseudo-magnetic field $\boldsymbol{b}^\eta = \eta \boldsymbol{b} = \eta b_z \hat{z}$, where $b_z$ has a nonzero gradient $\partial_z b_z = \beta$. As analyzed in Section 4.3.2, the magnon motion is governed by the semiclassical equation of motion $q(t) = q(0) - \eta g \mu_B \int_0^t \beta dt'/\hbar$.

Thus magnons are pumped into both zeroth Landau levels, indicating thermal energy non-conservation in the bulk, which is a clue of the magnon heat anomaly.

Due to the chiral nature of the pseudo-magnetic field $\boldsymbol{b}^\eta$, magnons on different zeroth Landau levels are oppositely pumped such that the magnon population edge on both zeroth Landau levels are lowered as illustrated in Fig. 4.7(c). The variation of the magnon population edge is denoted by $\delta_b \ll B_0$, and correspondingly both Weyl cones experience a magnetic field $b'_L = b'_R = B_0 - \delta_b$. According to the semiclassical equation of motion, we have

$$\delta_b = -\frac{\hbar|v_z^\eta|\eta \int dq_z}{g\mu_B} = \int_0^t \beta|v_z^\eta|dt'. \tag{4.59}$$

By comparing to Eqs. 4.34, 4.35, we can directly write down the magnon concentration variation on both zeroth Landau levels as

$$n_R^{\boldsymbol{E},\boldsymbol{b}} = n_L^{\boldsymbol{E},\boldsymbol{b}} \approx \frac{n_B(g\mu_B B_0)}{4\pi^2 l_E^2}\frac{g\mu_B\delta_b}{\hbar|v_z^\eta|}, \tag{4.60}$$

where we make the approximation $g\mu_B\delta_b \ll k_B T$. Because the magnon population edge is shifted identically on both chiral Landau levels, there is no net chirality transport between two Weyl cones. Nevertheless, the fact $n_R^{\boldsymbol{E},\boldsymbol{b}} + n_L^{\boldsymbol{E},\boldsymbol{b}} > 0$ indicates that there are more magnons in the bulk[11]. Therefore, the thermal energy in the bulk increases. By comparing to Eqs. 4.39, 4.40, we immediately obtain the heat injection into the two zeroth Landau levels in the limit $g\mu_B\delta_b \ll k_B T$ as

$$U_R^{\boldsymbol{E},\boldsymbol{b}} = U_L^{\boldsymbol{E},\boldsymbol{b}} \approx \frac{n_B(g\mu_B B_0)}{4\pi^2 l_E^2} g\mu_B B_0 \frac{g\mu_B\delta_b}{\hbar|v_z^\eta|}. \tag{4.61}$$

Thus the bulk heat injection rate can be written down as

$$\frac{d\rho_{\text{heat}}^{\boldsymbol{E},\boldsymbol{b}}}{dt} = \frac{dU_R^{\boldsymbol{E},\boldsymbol{b}}}{dt} + \frac{dU_L^{\boldsymbol{E},\boldsymbol{b}}}{dt} \approx -\frac{g^3\mu_B^3 n_B(g\mu_B B_0)}{2\pi^2\hbar^2 c^2} B_0 \mathcal{E}\beta. \tag{4.62}$$

More generally, the bulk heat injection rate reads

$$\frac{d\rho_{\text{heat}}^{\boldsymbol{E},\boldsymbol{b}}}{dt} + \nabla\cdot\boldsymbol{j}_{\text{heat}}^{\boldsymbol{E},\boldsymbol{b}} \approx \frac{g\mu_B B_0 n_B(g\mu_B B_0)}{2\pi^2\hbar^2 c^2}\nabla(\boldsymbol{\mu}\cdot\boldsymbol{b})\cdot[\nabla\times(\boldsymbol{E}\times\boldsymbol{\mu})]. \tag{4.63}$$

[11] In the limit $g\mu_B\delta_b \ll k_B T$, the total magnon concentration variation on zeroth Landau levels $n_R^{\boldsymbol{E},\boldsymbol{b}} + n_L^{\boldsymbol{E},\boldsymbol{b}} \sim g\mu_B\delta_b$ is linear in magnetic field variation $\delta_b$. And it is fundamentally different from the total magnon concentration variation $n_R^{\boldsymbol{E},\boldsymbol{B}} + n_L^{\boldsymbol{E},\boldsymbol{B}} \sim g^2\mu_B^2 B_5^2$ ($n_R^{\boldsymbol{e},\boldsymbol{b}} + n_L^{\boldsymbol{e},\boldsymbol{b}} \sim g^2\mu_B^2 b_5^2$) associated with magnon chiral anomaly in the low bias limit, which is of quadratic order of magnetic field bias $B_5$ ($b_5$).

This magnon heat anomaly equation is analogous to the magnon chiral anomaly equation (Eqs. 4.37, 4.50). It is a heat continuity equation with a source indicating that the bulk thermal energy is not conserved. Unfortunately, this heat anomaly does not have measurable anomalous currents

$$J_{\text{spin}}^{\boldsymbol{E},\boldsymbol{b}} = 0, \tag{4.64}$$

$$J_{\text{heat}}^{\boldsymbol{E},\boldsymbol{b}} = 0. \tag{4.65}$$

Because left-moving and right-moving magnons are always created/annihilated in pairs, as illustrated in Fig. 4.7(c).

We note that though the bulk thermal energy is not conserved, the total energy of a closed system must be conserved. Since Eq. 4.63 only characterizes the variation rate of the bulk thermal energy, we need to consider how the surface thermal energy is altered by the pseudo-magnetic field. As illustrated in Fig. 4.4(a), the bulk zeroth Landau levels are connected by a set of surface states. The magnons residing in these states can enter the bulk such that the thermal energy is transferred from the surface to the bulk. During this process, the external pseudo-magnetic field also does work on magnons; otherwise the heat pumping from surface to bulk would be spontaneous. The thermal energy from the surface and the mechanical energy from the pseudo-magnetic field constitute the heat injection into the bulk of the Weyl ferromagnet nanowire. In particular, if the pseudo-magnetic field is induced by the dynamic lattice deformation resulting from applying an ultrasonic sound wave, the energy loss during sound propagation in the Weyl ferromagnet will lead to sound attenuation, which, in principle, should be experimentally measurable.

### 4.3.4 Magnon heat anomaly due to pseudo-electric and magnetic fields

We consider another possibility of implementing the magnon heat anomaly. We apply a strain-induced chiral pseudo-electric field $\boldsymbol{e}^{\eta} = \eta\boldsymbol{e} = \eta(\frac{1}{2}\varepsilon x, \frac{1}{2}\varepsilon y, 0)$ to a Weyl ferromagnet nanowire aligned in $z$ direction. The two ends of the wire are attached to magnon reservoirs subjected to a magnetic field $\boldsymbol{B}_0 = B_0\hat{z}$ with the magnon population edges lying in the gap of the first Landau levels (Fig. 4.7(d)). We drive magnons with an inhomogeneous magnetic field $\boldsymbol{B} = B_z\hat{z}$, where $B_z$ has a nonzero gradient $\partial_z B_z = \mathcal{B}$. According to Section 4.3.1, the magnon motion is governed by the semiclassical equation of motion $q_z(t) = q_z(0) - g\mu_B \int_0^t \mathcal{B}dt'/\hbar$. Consequently, magnons are

pumped into both zeroth Landau levels and the thermal energy in the bulk increases, indicating a magnon heat anomaly.

The magnetic field $\boldsymbol{B}$ pumps magnons on different Weyl cones identically. However, due to the chiral nature of pseudo-electric field $\boldsymbol{e}^{\eta}$, the magnon population edge on both zeroth Landau levels are lowered as illustrated in Fig. 4.7(f). The variation of the magnon population edge is denoted as $\delta_B \ll B_0$ and both Weyl cones experience a magnetic field $B'_L = B'_R = B_0 - \delta_B$. According to the semiclassical equation of motion, we have

$$\delta_B = -\frac{\hbar|v_z^{\eta}|\int dq_z}{g\mu_B} = \int_0^t \mathcal{B}|v_z^{\eta}|dt'. \tag{4.66}$$

By comparing to Eqs. 4.34, 4.35, the magnon concentration variation on both zeroth Landau levels can be calculated as

$$n_R^{\boldsymbol{e},\boldsymbol{B}} = n_L^{\boldsymbol{e},\boldsymbol{B}} \approx \frac{n_B(g\mu_B B_0)}{4\pi^2 l_e^2}\frac{g\mu_B\delta_B}{\hbar|v_z^{\eta}|}, \tag{4.67}$$

in the limit $g\mu_B\delta_B \ll k_B T$. Because magnons on both zeroth Landau levels are always created in pairs, there is no net chirality transport between the two Weyl points, but the larger total number of magnons on the zeroth Landau levels indicates a thermal energy injection into the bulk of the Weyl ferromagnet. By comparing to Eqs. 4.39, 4.40, we can directly write down the heat injection into the two zeroth Landau levels in the limit $g\mu_B\delta_B \ll k_B T$ as

$$U_R^{\boldsymbol{e},\boldsymbol{B}} = U_L^{\boldsymbol{e},\boldsymbol{B}} \approx \frac{n_B(g\mu_B B_0)}{4\pi^2 l_e^2} g\mu_B B_0 \frac{g\mu_B\delta_B}{\hbar|v_z^{\eta}|}. \tag{4.68}$$

Thus the rate of heat injection into the bulk of the Weyl ferromagnet nanowire reads

$$\frac{d\rho_{\text{heat}}^{\boldsymbol{e},\boldsymbol{B}}}{dt} = \frac{dU_R^{\boldsymbol{e},\boldsymbol{B}}}{dt} + \frac{dU_L^{\boldsymbol{e},\boldsymbol{B}}}{dt} \approx -\frac{g^3\mu_B^3 n_B(g\mu_B B_0)}{2\pi^2\hbar^2 c^2} B_0 \varepsilon \mathcal{B}. \tag{4.69}$$

More generally, the bulk heat injection rate reads

$$\frac{d\rho_{\text{heat}}^{\boldsymbol{e},\boldsymbol{B}}}{dt} + \nabla\cdot\boldsymbol{j}_{\text{heat}}^{\boldsymbol{e},\boldsymbol{B}} \approx \frac{g\mu_B B_0 n_B(g\mu_B B_0)}{2\pi^2\hbar^2 c^2}\nabla(\boldsymbol{\mu}\cdot\boldsymbol{B})\cdot[\nabla\times(\boldsymbol{e}\times\boldsymbol{\mu})], \tag{4.70}$$

which is similar to the heat anomaly equation (Eq. 4.63), showing non-conservation of the bulk thermal energy. Again, when we take into account the contribution of the surface states and the applied pseudo-electric field, the heat anomaly will be removed and the total energy is conserved. In

contrast to the heat anomaly due to $\boldsymbol{E}$ and $\boldsymbol{b}^\eta$ in Section 4.3.3, the heat anomaly due to $\boldsymbol{e}^\eta$ and $\boldsymbol{B}$ does result in anomalous spin and heat currents

$$J_{\text{spin}}^{\boldsymbol{e},\boldsymbol{B}} = -\hbar|v_z^\eta|(n_R^{\boldsymbol{e},\boldsymbol{B}} + n_L^{\boldsymbol{e},\boldsymbol{B}}) \approx \hbar\frac{g^2\mu_B^2}{2\pi^2\hbar^2c^2}n_B(g\mu_B B_0)\delta_B\varepsilon, \tag{4.71}$$

$$J_{\text{heat}}^{\boldsymbol{e},\boldsymbol{B}} = |v_z^\eta|(U_R^{\boldsymbol{e},\boldsymbol{B}} + U_L^{\boldsymbol{e},\boldsymbol{B}}) \approx -\frac{g^3\mu_B^3}{2\pi^2\hbar^2c^2}n_B(g\mu_B B_0)B_0\delta_B\varepsilon, \tag{4.72}$$

both of which should be experimentally measurable. Unlike the magnon "chiral electric effect" (Eqs. 4.44, 4.45, 4.57, 4.58) whose spin and heat currents result from either EM fields or pseudo EM fields, the anomalous currents Eqs. 4.71, 4.72 result from their combination. Since the required pseudo-electric field $\boldsymbol{e}^\eta$ is induced by torsional strain, we refer to Eqs. 4.71, 4.72 as the magnon "chiral torsional effect".

## 4.4 Field dependence of anomalous spin and heat currents

In Section 4.3, we listed the magnon quantum anomaly equations (Eqs. 4.37, 4.50, 4.63, 4.70) and the associated anomalous spin (Eqs. 4.44, 4.57, 4.64, 4.71) and heat (Eqs. 4.45, 4.58, 4.65, 4.72) currents. The anomaly equations have explicit EM/pesudo-EM field dependence while the anomalous currents do not, because the explicit field dependence of magnetic field bias ($B_5/b_5$) and magnetic field variation ($\delta_b/\delta_B$) is unknown. In this section, we will derive how these quantities depend on EM/pseudo-EM fields, and eventually give the full field dependence for the anomalous spin and heat currents in both the semiclassical limit and the quantum limit.

We take the magnon chiral anomaly due to $\boldsymbol{E}$ and $\boldsymbol{B}$ as an example and determine how $B_5$ depends on these fields. In the semiclassical limit, the magnetic field bias between the two zeroth Landau levels dominates over the magnon Landau spacing $g\mu_B B_5 \gg \hbar\sqrt{2|g\mu_B\mathcal{E}v_x^\eta v_y^\eta/\hbar c^2|}$. Therefore, the chirality transported between the Weyl cones is

$$\begin{aligned}\rho_5^{\boldsymbol{E},\boldsymbol{B}} = \left\{\chi_R\int_{g\mu_B B_R}^{+\infty} + \chi_L\int_{g\mu_B B_L}^{+\infty}\right\}D_s(\epsilon)n_B(\epsilon)d\epsilon \\ \approx \frac{g^2\mu_B^2B_0^2}{2\pi^2\hbar^3|v_x^\eta v_y^\eta v_z^\eta|}n_B(g\mu_B B_0)\cdot 2g\mu_B B_5,\end{aligned} \tag{4.73}$$

where the magnon density of states can be estimated using the dispersion $\varepsilon_{\boldsymbol{k}} = \hbar\sqrt{(v_x^\eta k_x)^2 + (v_y^\eta k_y)^2 + (v_z^\eta k_z)^2}$ as

$$D_s(\epsilon) = \frac{1}{V}\sum_{\boldsymbol{k}} \delta(\epsilon - \varepsilon_{\boldsymbol{k}}) = \frac{\epsilon^2}{2\pi^2\hbar^3|v_x^\eta v_y^\eta v_z^\eta|}.$$

In Section 4.2.1, we have obtained the chirality pumping rate (Eq. 4.36) in the absence of scattering of magnons between the two zeroth Landau levels. However, in a realistic magnet, the chirality mixing scattering mechanism always exists; otherwise the chirality transported between Weyl cones goes to infinity. Due to such scattering, the chirality pumping rate is changed to

$$\frac{d\rho_5^{\boldsymbol{E},\boldsymbol{B}}}{dt} = -\frac{g^2\mu_B^2}{2\pi^2\hbar^2c^2} n_B(g\mu_B B_0)\mathcal{E}\mathcal{B} - \frac{\rho_5^{\boldsymbol{E},\boldsymbol{B}}}{\tau^{\boldsymbol{E},\boldsymbol{B}}}, \tag{4.74}$$

where $\tau^{\boldsymbol{E},\boldsymbol{B}}$ is the mean free time of magnons due to chirality mixing scattering. The solution for $\rho_5^{\boldsymbol{E},\boldsymbol{B}}$ at sufficiently long times $t \gg \tau^{\boldsymbol{E},\boldsymbol{B}}$ is then

$$\rho_5^{\boldsymbol{E},\boldsymbol{B}} = -\frac{g^2\mu_B^2}{2\pi^2\hbar^2c^2} n_B(g\mu_B B_0)\mathcal{E}\mathcal{B}\tau^{\boldsymbol{E},\boldsymbol{B}}. \tag{4.75}$$

By referring to Eq. 4.73, we obtain the field dependence of the effective magnetic field bias as

$$B_5 = -\frac{\hbar|v_x^\eta v_y^\eta v_z^\eta|}{2g\mu_B c^2 B_0^2}\mathcal{E}\mathcal{B}\tau^{\boldsymbol{E},\boldsymbol{B}} \propto \mathcal{E}\mathcal{B}. \tag{4.76}$$

where we have assumed that the chirality mixing scattering is characterized by a constant magnon mean free time $\tau^{\boldsymbol{E},\boldsymbol{B}}$. In that case, the field dependence of the anomalous spin/heat current can be obtained as $J^{\boldsymbol{E},\boldsymbol{B}}_{\text{spin/heat}} \propto \mathcal{E}^2\mathcal{B}$, which is dual to the electron chiral magnetic current since magnon EM fields are dual to electron EM potentials.

In the quantum limit, the Landau level spacing becomes comparable to the magnetic field bias $g\mu_B B_5 \lesssim \hbar\sqrt{2|g\mu_B\mathcal{E}v_x^\eta v_y^\eta/\hbar c^2|}$, and the magnon density of states is proportional to the electric field gradient ($D_q(\epsilon) \sim 1/l_E^2 \propto \mathcal{E}$). The chirality transported between Weyl cones is then $\rho_5^{\boldsymbol{E},\boldsymbol{B}} \propto \mathcal{E}B_5$, distinct from the semiclassical result Eq. 4.73. By comparing to Eq. 4.75, we obtain the field dependence of the magnetic field bias $B_5 \propto \mathcal{B}$, provided that the magnon mean free time is constant. As a result, the field dependence of the anomalous spin/heat current in the quantum limit can be immediately obtained as $J^{\boldsymbol{E},\boldsymbol{B}}_{\text{spin/heat}} \propto \mathcal{E}\mathcal{B}$.

By replicating the analysis above, we can determine the field dependence of other magnetic field bias/variations as $b_5 \propto \varepsilon\beta$, $\delta_b \propto \mathcal{E}\beta$, and $\delta_B \propto \varepsilon\mathcal{B}$

in the semiclassical limit and $b_5 \propto \beta$, $\delta_b \propto \beta$, and $\delta_B \propto \mathcal{B}$ in the quantum limit. The resulting field dependence of the corresponding spin/heat current is summarized in Table. 4.1. The magnon chiral electric spin/heat current (Eqs. 4.44, 4.45) is dual to the chiral magnetic current [62, 63], and the magnon chiral torsional spin/heat current (Eqs. 4.71, 4.72) is dual to the chiral torsional current given in Ref. [94]. However, it is worth noting that the magnon anomalous spin/heat current (Eqs. 4.57, 4.58) due to $\boldsymbol{e}$ and $\boldsymbol{b}$ shows unprecedented field dependence without any anomalous electric current counterpart.

Table 4.1: Summary of field (gradient) dependence of anomalous spin and heat currents in magnon quantum anomalies.

| **Field** | **Semiclassical limit** | **Quantum limit** |
|---|---|---|
| $\boldsymbol{E}, \boldsymbol{B}$ | $J^{\boldsymbol{E},\boldsymbol{B}}_{\text{spin/heat}} \propto \mathcal{E}^2\mathcal{B}$ | $J^{\boldsymbol{E},\boldsymbol{B}}_{\text{spin/heat}} \propto \mathcal{E}\mathcal{B}$ |
| $\boldsymbol{e}, \boldsymbol{b}$ | $J^{\boldsymbol{e},\boldsymbol{b}}_{\text{spin/heat}} \propto \varepsilon^3\beta^2$ | $J^{\boldsymbol{e},\boldsymbol{b}}_{\text{spin/heat}} \propto \varepsilon\beta^2$ |
| $\boldsymbol{E}, \boldsymbol{b}$ | $J^{\boldsymbol{E},\boldsymbol{b}}_{\text{spin/heat}} = 0$ | $J^{\boldsymbol{E},\boldsymbol{b}}_{\text{spin/heat}} = 0$ |
| $\boldsymbol{e}, \boldsymbol{B}$ | $J^{\boldsymbol{e},\boldsymbol{B}}_{\text{spin/heat}} \propto \varepsilon^2\mathcal{B}$ | $J^{\boldsymbol{e},\boldsymbol{B}}_{\text{spin/heat}} \propto \varepsilon\mathcal{B}$ |

## 4.5 Experimental measurement of magnon quantum anomalies

In Section 4.4, we have obtained the field (gradient) dependence of anomalous spin and heat currents in magnon quantum anomalies as summarized in Tab. 4.1. Unfortunately, the direct measurement of such anomalous spin and heat transport is experimentally non-trivial due to the lack of induced electric field from spin currents and the dissipation of thermal energy from heat currents. For this reason, an easily measurable signature quantity is required for the experimental detection of magnon quantum anomalies.

We propose that the force on the magnon current carrying Weyl ferromagnet nanowire exerted by an external inhomogeneous electric or pseudo-electric field could be such a signature quantity. Intuitively, this force onto a magnon current can be understood as an analog of Ampère force, which

emerges when applying an external magnetic field to an electric current. In the following, we will derive this force quantitatively for each magnon quantum anomaly.

### 4.5.1 Experimental signature of magnon chiral anomaly due to electric and magnetic fields

In Section 4.2.1, we have demonstrated that magnon bands are Landau-quantized by an external inhomogeneous electric field $\boldsymbol{E} = (\frac{1}{2}\mathcal{E}x, \frac{1}{2}\mathcal{E}y, 0)$. We now apply an additional electric field $\boldsymbol{E}' = (0, \mathcal{E}'z, 0)$ with $\mathcal{E}' \ll \mathcal{E}$ to the Weyl ferromagnet nanowire. This weak additional electric field will not lead to further Landau quantization of magnon bands. But, according to the magnon equation of motion (Eq. 4.25), it gives rise to a "magnon Lorentz force"

$$\hbar\frac{d\boldsymbol{k}}{dt} = \frac{1}{c^2}\boldsymbol{v} \times [\nabla \times (\boldsymbol{\mu} \times \boldsymbol{E}')], \tag{4.77}$$

which results from the Aharonov-Casher effect [83]. For the magnon population illustrated in Fig. 4.7(a), the net force contributed by magnons from two zeroth Landau levels is zero, because for each magnon drifting at velocity $|v_z^\eta|$, there is always another magnon drifting at velocity $-|v_z^\eta|$.

However, when magnons are pumped by an inhomogeneous magnetic field in the $z$ direction $\boldsymbol{B} = B_z\hat{z}$, a magnon imbalance develops on the zeroth Landau levels as illustrated in Fig. 4.7(b) such that there are more right-moving magnons than left-moving magnons. This imbalance is the cause of the magnon chiral anomaly (Eq. 4.37) and the associated anomalous transport (Eqs. 4.44, 4.45). It also produces a force acting on the whole nanowire, which may serve as a signature quantity for the experimental confirmation of the magnon chiral anomaly due to $\boldsymbol{E}$ and $\boldsymbol{B}$. Explicitly, the force reads

$$\boldsymbol{F}^{\boldsymbol{E},\boldsymbol{B}} = \sum_{LL_0} \frac{1}{c^2}\boldsymbol{v} \times [\nabla \times (\boldsymbol{\mu} \times \boldsymbol{E}')] = -V(n_R^{\boldsymbol{E},\boldsymbol{B}} - n_L^{\boldsymbol{E},\boldsymbol{B}})|v_z^\eta|\frac{g\mu_B\mathcal{E}'}{c^2}\hat{x}, \tag{4.78}$$

where the summation goes over the zeroth Landau levels ($LL_0$) and $V$ refers to the volume of the nanowire. To estimate the magnitude of this force, we first assume the additional electric field gradient $\mathcal{E}' = 0.1\mathcal{E}$ such that $\mathcal{E}'$ has little effects on the magnon band structure in Fig. 4.4. We then take the magnon drifting velocity $|v_z^\eta| \sim 10^2$m/s of the same order as that of yttrium iron garnet (YIG) [174]. For a typical nanowire with cross section radius $\sim$ 100nm and length $\sim 100\mu$m, the volume can be estimated as $V \sim 10^{-18}\text{m}^3$.

To estimate the magnon concentration imbalance, we make use of Eqs. 4.34, 4.35 and get

$$n_R^{\boldsymbol{E},\boldsymbol{B}} - n_L^{\boldsymbol{E},\boldsymbol{B}} \approx \frac{n_B(g\mu_B B_0)}{2\pi^2 l_E^2}\frac{g\mu_B \mathcal{B}}{\hbar}\tau^{\boldsymbol{E},\boldsymbol{B}}. \tag{4.79}$$

For the electric field gradient used in Fig. 4.4, we obtain $1/2\pi^2 l_E^2 \sim 10^{14}\mathrm{m}^{-2}$. We further estimate the magnon mean free time $\tau^{\boldsymbol{E},\boldsymbol{B}} \sim 10^{-6}$s, which is of the same order as that of YIG [175]. Lastly, an inhomogeneous magnetic field with gradient $\mathcal{B} \sim 10\mathrm{T/m}$ should be experimentally available. These lead to a magnon concentration imbalance $n_R^{\boldsymbol{E},\boldsymbol{B}} - n_L^{\boldsymbol{E},\boldsymbol{B}} \sim 10^{20}\mathrm{m}^{-3}$ and a force $F^{\boldsymbol{E},\boldsymbol{B}} \sim 10^{-15}$N. By means of atomic force microscopy (AFM), this small force can be sensed as a clue of magnon chiral anomaly due to $\boldsymbol{E}$ and $\boldsymbol{B}$.

Before we leave this section, we briefly analyze the mechanical effects of magnons on the surface and the higher Landau levels. According to Fig. 4.4(a, b), the almost flat surface states indicate a vanishing magnon drifting velocity, thus a negligible force contribution is expected from the surface magnons. For the higher Landau levels, the magnon population alters little during the whole pumping process because all states in these bands are occupied. The force contribution is thus ideally zero because the numbers of left-moving magnons and right-moving magnons are equal. In conclusion, the net force on the nanowire is mostly contributed by the magnon imbalance on the zeroth Landau levels.

### 4.5.2 Experimental signature of magnon chiral anomaly due to pseudo-electric and pseudo-magnetic fields

In Section 4.2.2, we have demonstrated that magnon bands are Landau-quantized by an inhomogeneous pseudo-electric field $\boldsymbol{e}^\eta = \eta(\frac{1}{2}\varepsilon x, \frac{1}{2}\varepsilon y, 0)$ induced by a static twist. Again, by applying an additional electric field $\boldsymbol{E}' = (0, \mathcal{E}' z, 0)$, a magnon will experience a Lorentz force given by Eq. 4.77. However, for the magnon population illustrated in Fig. 4.7(d), the net force contributed by magnons on two zeroth Landau levels is nonzero because these two bands are now co-propagating.

Nevertheless, when magnons are pumped by a pseudo-magnetic field in the $z$ direction $\boldsymbol{b}^\eta = \eta b_z \hat{z}$, a magnon imbalance develops as illustrated in Fig. 4.7(e), with slightly more right-moving magnons on the zeroth Landau levels. The force acting on the nanowire increases by

$$\delta \boldsymbol{F}^{\boldsymbol{e},\boldsymbol{b}} = -V(n_R^{\boldsymbol{e},\boldsymbol{b}} + n_L^{\boldsymbol{e},\boldsymbol{b}})|v_z^\eta|\frac{g\mu_B \mathcal{E}'}{c^2}\hat{x}, \tag{4.80}$$

where the magnon concentration variation can be estimated by Eqs. 4.47, 4.48 as

$$n_R^{\boldsymbol{e},\boldsymbol{b}} + n_L^{\boldsymbol{e},\boldsymbol{b}} \approx \frac{e^{g\mu_B B_0/k_B T}}{e^{g\mu_B B_0/k_B T} - 1} \frac{g\mu_B \beta |v_z^\eta| \tau^{\boldsymbol{e},\boldsymbol{b}}}{2k_B T} \frac{n_B(g\mu_B B_0)}{2\pi^2 l_e^2} \frac{g\mu_B \beta}{\hbar} \tau^{\boldsymbol{e},\boldsymbol{b}}. \quad (4.81)$$

If we assume similar parameters, i.e., $l_e \sim l_E$, $\beta \sim \mathcal{B}$, and $\tau^{\boldsymbol{e},\boldsymbol{b}} \sim \tau^{\boldsymbol{E},\boldsymbol{B}}$, we can estimate the force increase $\delta F^{\boldsymbol{e},\boldsymbol{b}} \sim 10^{-21}$N at room temperature. Though this force increase reflects the magnon number non-conservation as well as the magnon anomalous transport (Eqs. 4.57, 4.58), the difficulty of force sensing is greatly increased.

To avoid this difficulty, we propose the force sensing experiment using an additional pseudo-electric field $\boldsymbol{e}'_\eta = \eta(0, \varepsilon' z, 0)$, which can be generated by a circular bend deformation (Appendix E). For the magnon population shown in Fig. 4.7(d), the total Lorentz force on magnons on the zeroth Landau levels is restored to zero due to the chiral nature of the additional pseudo-electric field. However, as the pseudo-magnetic field is switched on, the magnon imbalance illustrated in Fig. 4.7(e) will produce a nonzero force $\boldsymbol{F}^{\boldsymbol{e},\boldsymbol{b}}$ acting on the whole nanowire. Explicitly, the force reads

$$\boldsymbol{F}^{\boldsymbol{e},\boldsymbol{b}} = -V(n_R^{\boldsymbol{e},\boldsymbol{b}} - n_L^{\boldsymbol{e},\boldsymbol{b}})|v_z^\eta| \frac{g\mu_B \varepsilon'}{c^2} \hat{x}, \quad (4.82)$$

where the magnon concentration imbalance is given by Eqs. 4.47, 4.48 as

$$n_R^{\boldsymbol{e},\boldsymbol{b}} - n_L^{\boldsymbol{e},\boldsymbol{b}} \approx \frac{n_B(g\mu_B B_0)}{2\pi^2 l_e^2} \frac{g\mu_B \beta}{\hbar} \tau^{\boldsymbol{e},\boldsymbol{b}}. \quad (4.83)$$

Using the parameters above, we obtain the magnon imbalance $n_R^{\boldsymbol{e},\boldsymbol{b}} - n_L^{\boldsymbol{e},\boldsymbol{b}} \sim 10^{20}\mathrm{m}^{-3}$ and the force exerted on the nanowire is then $F^{\boldsymbol{e},\boldsymbol{b}} \sim 10^{-15}$N, which can be measured by AFM. It is worth noting that the surface magnons, despite possessing a finite drifting velocity, do not have appreciable force contribution, because the additional pseudo-electric field $\boldsymbol{e}'_\eta$ only lives in the vicinity of Weyl cones deep in the bulk and thus has no effect on the surface. Unlike $\delta F^{\boldsymbol{e},\boldsymbol{b}}$ which reflects the anomalous magnon transport (Eqs. 4.57, 4.58), the force $F^{\boldsymbol{e},\boldsymbol{b}}$ indicates the magnon population imbalance on the zeroth Landau levels and is thus a signature of the magnon chiral anomaly due to $\boldsymbol{e}^\eta$ and $\boldsymbol{b}^\eta$.

### 4.5.3 Experimental signature of magnon heat anomaly due to electric and pseudo-magnetic fields

For the magnon heat anomaly due to $\boldsymbol{E}$ and $\boldsymbol{b}^\eta$, the Landau quantization is still provided by the inhomogeneous electric field, but the pumping field

is a chiral pseudo-magnetic field due to a dynamic uniaxial strain, leading to an equal number of left-moving and right-moving magnons injected into the bulk as illustrated in Fig. 4.7(c). This renders $\boldsymbol{E}' = (0, \mathcal{E}' z, 0)$ in Section 4.5.1 useless because the force contributed by the magnons on the zero Landau levels is always zero. However, an additional pseudo-electric field $\boldsymbol{e}'_\eta = \eta(0, \varepsilon' z, 0)$ produces a measurable mechanical effect.

Due to the chiral nature of $\boldsymbol{e}'_\eta$, the magnons on the zeroth Landau levels (Fig. 4.7(a)) contribute constructively to the force exerted on the nanowire. When the magnons are pumped by the pseudo-magnetic field, more magnons are driven into the zeroth Landau levels, leading to an increase in this force

$$\delta \boldsymbol{F}^{\boldsymbol{E},\boldsymbol{b}} = -V(n_R^{\boldsymbol{E},\boldsymbol{b}} + n_L^{\boldsymbol{E},\boldsymbol{b}})|v_z^\eta| \frac{g\mu_B \varepsilon'}{c^2} \hat{x}, \tag{4.84}$$

where the magnon concentration variation is given by Eq. 4.60 as

$$n_R^{\boldsymbol{E},\boldsymbol{b}} + n_L^{\boldsymbol{E},\boldsymbol{b}} \approx \frac{n_B(g\mu_B B_0)}{2\pi^2 l_E^2} \frac{g\mu_B \beta}{\hbar} \tau^{\boldsymbol{E},\boldsymbol{b}}. \tag{4.85}$$

Assuming $\tau^{\boldsymbol{E},\boldsymbol{b}} \sim 10^{-6}$s leads to an AFM measurable force increase $\delta F^{\boldsymbol{E},\boldsymbol{b}} \sim 10^{-15}$N. As analyzed in Section 4.5.1, this force is the actual force experienced by the nanowire because there is no force contribution from the magnons on the surface or the higher Landau levels. The force increase $\delta F^{\boldsymbol{E},\boldsymbol{b}}$ is of great experimental importance, because there is no magnon anomalous transport (Eqs. 4.64, 4.65) in the magnon quantum anomaly due to $\boldsymbol{E}$ and $\boldsymbol{b}^\eta$.

### 4.5.4 Experimental signature of magnon heat anomaly due to pseudo-electric and magnetic fields

For the magnon heat anomaly due to $\boldsymbol{e}^\eta$ and $\boldsymbol{B}$, the Landau quantization is provided by the inhomogeneous pseudo-electric field resulting from a static twist, but the pumping field is an ordinary magnetic field, leading to an equal number of magnons injected into each zeroth Landau level as illustrated in Fig. 4.7(f). Consequently, the magnons on the zeroth Landau levels contribute zero total force in the presence of the chiral pseudo-electric field $\boldsymbol{e}'_\eta = \eta(0, \varepsilon' z, 0)$. We thus resort to an additional ordinary electric field $\boldsymbol{E}' = (0, \mathcal{E}' z, 0)$ as is used in Section 4.5.1.

Because the two zeroth Landau levels are co-propagating under the pseudo-electric field $\boldsymbol{e}^\eta$, which results from a static twist, the magnons on these two zeroth Landau levels contribute constructively to the force exerted on the nanowire in the presence of the additional electric field $\boldsymbol{E}'$. When more

magnons are pumped by $\boldsymbol{B}$ into the zeroth Landau levels, the force increases by

$$\delta \boldsymbol{F}^{\boldsymbol{e},\boldsymbol{B}} = -V(n_R^{\boldsymbol{e},\boldsymbol{B}} + n_L^{\boldsymbol{e},\boldsymbol{B}})|v_z^\eta| \frac{g\mu_B \mathcal{E}'}{c^2}\hat{x}, \tag{4.86}$$

where the magnon concentration variation is given by Eq. 4.67 as

$$n_R^{\boldsymbol{e},\boldsymbol{B}} + n_L^{\boldsymbol{e},\boldsymbol{B}} \approx \frac{n_B(g\mu_B B_0)}{2\pi^2 l_e^2} \frac{g\mu_B \mathcal{B}}{\hbar} \tau^{\boldsymbol{e},\boldsymbol{B}}. \tag{4.87}$$

Assuming $\tau^{\boldsymbol{e},\boldsymbol{B}} \sim 10^{-6}$s leads to an AFM measurable force increase $\delta F^{\boldsymbol{e},\boldsymbol{B}} \sim 10^{-15}$N as a signature of both the magnon heat anomaly (Eq. 4.70) and the anomalous transport (Eqs. 4.71, 4.72). Unlike the case analyzed in Section 4.5.1 and Section 4.5.3 where surface magnons have a vanishing drifting velocity or the case analyzed in Section 4.5.2 where the effective surface pseudo-electric field is zero, the surface magnons in heat anomaly due to $\boldsymbol{e}^\eta$ and $\boldsymbol{B}$ give rise to non-trivial mechanical effect due to non-vanishing drifting velocity and effective surface electric field $\boldsymbol{E}'$. However, because surface states and the zeroth Landau levels are counter-propagating and their magnon numbers always change in opposite directions, the force due to surface magnon concentration variation always adds constructively to the bulk force variation $\delta F^{\boldsymbol{e},\boldsymbol{B}}$, leading to an even larger AFM measurable mechanical effect.

## 4.6 Summary

In this chapter, we have derived the magnon quantum anomalies and the anomalous spin and heat currents in a Weyl ferromagnet under electromagnetic fields and strain-induced chiral pseudo-electromagnetic fields. We first analyze a multilayer model of a Weyl ferromagnet whose spin wave structure possesses two linearly dispersive Weyl cones located on the $k_z$ axis at the corners of the honeycomb lattice Brillouin zone, akin to the electronic structure of Weyl semimetals. We show that the two Weyl cones are connected by a set of surface states analogous to the "Fermi arcs" in Weyl semimetals. These surface states can be understood as the combination of chiral edge states of each $k_z$-fixed 2D slice of the Weyl ferromagnet, which realizes a magnon Chern insulator whose Chern number is nontrivial for the momenta between the two Weyl points.

We then analyze how the Weyl ferromagnet reacts to EM fields and strain-induced chiral pseudo-EM fields. Under an inhomogeneous electric

field $\boldsymbol{E}$, due to the Aharonov-Casher effect [83], the magnons will be Landau-quantized. Similar Landau quantization can be obtained by a static twist (around $z$ axis) of the Weyl ferromagnet nanowire because an inhomogeneous pseudo-electric field $\boldsymbol{e}^\eta$ is induced. Such a chiral pseudo-electric field only lives in the vicinity of the magnon Weyl points and couples to them oppositely, leading to a pair of co-propagating zeroth Landau levels. The Landau-quantized magnons can be manipulated by applying an inhomogeneous magnetic field $\boldsymbol{B}$, which contributes a Zeeman energy whose gradient acts as a driving force. A similar pumping process is realized by applying a dynamic uniaxial strain to the Weyl ferromagnet, so that an inhomogeneous chiral pseudo-magnetic field $\boldsymbol{b}^\eta$ is induced. Again, this field strongly depends on the "Diracness" of the spin wave structure and only couples to Weyl magnons. Due to its chiral nature, magnons are pumped oppositely on different Weyl cones.

Furthermore, we show that the four possible combinations of electric field ($\boldsymbol{E}/\boldsymbol{e}^\eta$) and magnetic field ($\boldsymbol{B}/\boldsymbol{b}^\eta$) give rise to magnon quantum anomalies and anomalous spin and heat currents. For $(\boldsymbol{E}, \boldsymbol{B})$, magnons are pumped from one zeroth Landau level to the other, resulting in a chirality imbalance between the two Landau levels. Anomalous spin and heat currents arise and are proportional to this imbalance, resembling the chiral magnetic effect in Weyl semimetals. We thus call this anomaly-related transport the magnon "chiral electric effect." For $(\boldsymbol{e}^\eta, \boldsymbol{b}^\eta)$, magnons are also injected into one zeroth Landau level and extracted out of the other, leading to a chirality imbalance as well. Remarkably, this magnon chiral anomaly due to pure pseudo-electromagnetic fields has weak but non-zero anomalous spin and heat currents, unlike the electron chiral magnetic current which must be zero in the presence of pseudo-electromagnetic fields. This is because magnons are quasiparticles immune to the particle conservation law. For $(\boldsymbol{E}, \boldsymbol{b}^\eta)$, magnons are pumped between the surface and the bulk, giving rise to a heat imbalance between the two. For this reason, we refer to such a phenomenon as the magnon "heat anomaly" because the energy in the bulk itself is not conserved. Unfortunately, there are always an equal number of right-moving magnons and left-moving magnons; thus no net spin and heat currents exist. For $(\boldsymbol{e}^\eta, \boldsymbol{B})$, magnons are also pumped between the surface and the bulk. Due to the chiral nature of $\boldsymbol{e}^\eta$, the bulk and the surface always have opposite velocities. Such a bulk-surface separation thus causes a magnon "chiral torsional effect" that gives spin and heat currents proportional to the bulk-surface magnon imbalance.

Lastly, considering the difficulty of the direct measurement of magnon anomalous spin and heat currents, we propose AFM based force sensing

experiments. For $(\boldsymbol{E}, \boldsymbol{B})$, an additional electric field on the nanowire exerts a force $\boldsymbol{F}^{\boldsymbol{E},\boldsymbol{B}}$ caused by the magnon imbalance on zeroth Landau levels, reflecting the magnon chiral anomaly and the magnon chiral electric effect. For $(\boldsymbol{e}^\eta, \boldsymbol{b}^\eta)$, an additional pseudo-electric field on the nanowire gives rise to a force $\boldsymbol{F}^{\boldsymbol{e},\boldsymbol{b}}$, also caused by the magnon imbalance on zeroth Landau levels, indicating the magnon chiral anomaly due to pseudo-EM fields. For $(\boldsymbol{E}, \boldsymbol{b}^\eta)$, we demonstrate that the additional pseudo-electric field causes a force increase $\delta\boldsymbol{F}^{\boldsymbol{E},\boldsymbol{b}}$ on the nanowire, which is a signature of the magnon heat anomaly. This allows us to detect such an anomaly experimentally though the anomalous transport is lacking. For $(\boldsymbol{e}^\eta, \boldsymbol{B})$, we elucidate that the additional electric field produces a force increase $\delta F^{\boldsymbol{e},\boldsymbol{B}}$ on the nanowire, which is a clue of the magnon heat anomaly and the magnon chiral torsional effect.

To experimentally test the magnon quantum anomalies, we first require a Weyl ferromagnet, which may be artificially engineered by layering the honeycomb ferromagnet $CrX_3$ (X = F, Cl, Br, I) [169, 170]. Weyl ferromagnets are also proposed to occur intrinsically in the pyrochlore oxide $Lu_2V_2O_7$ [20]. However, our theory constructed for multilayer ferromagnets cannot be directly transplanted to the pyrochlore lattice, where a twist around [111] rather than $z$ axis may be the natural choice. The second requirement is that the candidate materials should be flexible to allow for sufficient twist in order to generate a strong pseudo-electric field to Landau-quantize the magnon bands. Unfortunately, the mechanical properties regarding the flexibility of candidate materials are lacking, and further experimental work is needed to verify whether or not layered honeycomb ferromagnets and $Lu_2V_2O_7$ are suitable materials.

There are several future directions that might be interesting to pursue based on the present work. The first is to test whether other types of spin lattice deformation can induce chiral pseudo-EM fields. In the context of Weyl semimetals, Ref. [93] shows that a screw dislocation can lead to the chiral torsional effect. It will be interesting to examine whether such deformation design will induce a pseudo-electric field in a Weyl magnet. Another direction is to study how other Weyl bosons react to strain-induced chiral gauge fields. To date, strain-induced Landau levels have been observed in photonic graphene [90]. Since "photonic Weyl semimetals" [29–31] have been proposed and realized, checking whether or not strain can induce chiral anomalies in these photonic systems will also be rewarding.

# Chapter 5

# Conclusions

In the present dissertation, we have studied three types of Dirac materials – Weyl semimetals, Weyl superconductors, and Weyl ferromagnets, paying close attention to their band structure under elastic lattice deformation due to strain. The associated electronic/thermal/spin transport is carefully investigated.

In Chapter 2, we study a Weyl semimetal thin film under a circular bend lattice deformation. The resulting spatial tuning of the electronic orbitals gives rise to a pseudo-magnetic field and the Landau quantization of energy bands. When the curvature of the thin film is continuously adjusted, the strain-induced pseudo-magnetic field begins to scan and the Landau levels begin to fall of the Fermi surface successively, leading to a periodic population on the Fermi surface. Consequently, the Shubnikov-de Haas quantum oscillation occurs in the complete absence of magnetic fields.

In Chapter 3, we apply a circular bend lattice deformation to a Weyl superconductor multilayer composed of alternately stacked topological insulator layers and $s$-wave superconductor layers. The spatially tuning of the electronic orbitals due to the lattice deformation is shown to Landau-quantize the *charge neutral* Bogoliubov quasiparticles, while the ordinary magnetic field is not capable of bringing Landau quantization due to the Meissner effect. When the lattice deformation varies, the thermal conductivity begins to oscillate. Remarkably, such quantum oscillation occurs in the superconducting regime, which is not accessible by the ordinary magnetic field, because strain cannot be screened by superconductivity.

In Chapter 4, we investigate the Weyl ferromagnet nanowire under a static torsional strain and a dynamic uniaxial strain and discover that the former lattice deformation provides magnon Landau quantization while the latter is responsible for magnon pumping. Considering the magnon Landau levels under an inhomogeneous electric field and magnon pumping under an inhomogeneous magnetic field, we propose that the torsional strain induces a pseudo-electric field while the uniaxial strain induces a pseudo-magnetic field. The combination of electromagnetic/pseudo-electromagnetic fields gives rise to magnon chiral anomaly and magnon heat anomaly. And the associated

spin and heat transport known as magnon chiral electric effect and magnon chiral torsional effect are derived to possess unique electromagnetic field (gradient) dependence.

The work presented in this dissertation provides a novel way of manipulating fermionic and bosonic quasiparticles and may have potential application to experiments which require large electromagnetic fields. For example, the observation of magnon Dirac-Landau levels may require an extremely inhomogeneous electric field with gradient $\sim 10^{22}\mathrm{V/m}^2$, which may not be easily accessible by an ordinary electric field but can be fairly easy to be realized by deforming the lattice constant of the spin lattice by just a few percent.

Based on the present dissertation, there are two further directions worthy to be investigated. Firstly, it will be rewarding to explore Weyl semimetals, Weyl superconductors, and Weyl ferromagnets in the presence of elastic gauge field and temperature gradient to see whether other non-equilibrium transport (e.g., gravitational anomaly, conformal anomaly, and gyrotropic magnetic effect) will occur. These studies may shed new light on understanding high energy physics in condensed matter systems. Secondly, it will be interesting to apply strain to other bosonic or classical Dirac systems (photonic Dirac/Weyl semimetals, phononic Weyl semimetals, graphene circuits, etc.) and investigate the transport related to Landau quantization. The technique of strain engineering may be of great experimental significance, because no other ways are currently known to bring about Landau quantization in most of the bosonic and classical systems.

# Bibliography


[1] P. A. M. Dirac, Proc. Royal Soc. Lond. A **117**, 610 (1928).

[2] L. H. Ryder (Cambridge University Press, 1996).

[3] A. Einstein, Ann. Phys. **322**, 891 (1905).

[4] E. Schrödinger, Ann. Phys. **385**, 437 (1926).

[5] C. D. Anderson, Phys. Rev. **43**, 491 (1933).

[6] E. Majorana, Nuovo Cimento **5**, 171 (1937).

[7] H. Weyl, Z. Phys. **56**, 330 (1929).

[8] W. Pauli, Phys. Today **31**, 27 (1930).

[9] L. Landau, Nucl. Phys. **3**, 127 (1957).

[10] T. D. Lee and C.-N. Yang, Phys. Rev. **105**, 1671 (1957).

[11] A. Salam, Nuovo Cimento **5**, 299 (1957).

[12] C. Cowan, Science **124**, 103 (1956).

[13] T. Kajita, Rev. Mod. Phys. **88**, 030501 (2016).

[14] A. B. McDonald, Rev. Mod. Phys. **88**, 030502 (2016).

[15] A. C. Neto, F. Guinea, N. M. Peres, K. S. Novoselov, and A. K. Geim, Rev. Mod. Phys. **81**, 109 (2009).

[16] M. Goerbig, Rev. Mod. Phys. **83**, 1193 (2011).

[17] N. Armitage, E. Mele, and A. Vishwanath, Rev. Mod. Phys. **90**, 015001 (2018).

[18] T. Meng and L. Balents, Phys. Rev. B **86**, 054504 (2012).

[19] S. A. Yang, H. Pan, and F. Zhang, Phys. Rev. Lett. **113**, 046401 (2014).

[20] Y. Su, X. Wang, and X. Wang, Phys. Rev. B **95**, 224403 (2017).

[21] A. Mook, J. Henk, and I. Mertig, Phys. Rev. Lett. **117**, 157204 (2016).

[22] F.-Y. Li, Y.-D. Li, Y. B. Kim, L. Balents, Y. Yu, and G. Chen, Nat. Commun. **7**, 12691 (2016).

[23] S.-K. Jian and W. Nie, Phys. Rev. B **97**, 115162 (2018).

[24] F.-Y. Li, Y.-D. Li, Y. Yu, A. Paramekanti, and G. Chen, Phys. Rev. B **95**, 085132 (2017).

[25] Y. Su and X. Wang, Phys. Rev. B **96**, 104437 (2017).

[26] V. A. Zyuzin and A. A. Kovalev, Phys. Rev. B **97**, 174407 (2018).

[27] S. Owerre, Phys. Rev. B **97**, 094412 (2018).

[28] Q. Guo, B. Yang, L. Xia, W. Gao, H. Liu, J. Chen, Y. Xiang, and S. Zhang, Phys. Rev. Lett. **119**, 213901 (2017).

[29] W. Gao, B. Yang, M. Lawrence, F. Fang, B. Béri, and S. Zhang, Nat. Commun. **7**, 12435 (2016).

[30] W.-J. Chen, M. Xiao, and C. T. Chan, Nat. Commun. **7**, 13038 (2016).

[31] Q. Lin, M. Xiao, L. Yuan, and S. Fan, Nat. Commun. **7**, 13731 (2016).

[32] V. Peri, M. Serra-Garcia, R. Ilan, and S. D. Huber, Nat. Phys. **15**, 357 (2019).

[33] J. E. Socolar, T. C. Lubensky, and C. L. Kane, New J. Phys. **19**, 025003 (2017).

[34] S. R. Elliott and M. Franz, Rev. Mod. Phys. **87**, 137 (2015).

[35] K. S. Novoselov, A. K. Geim, S. V. Morozov, D. Jiang, Y. Zhang, S. V. Dubonos, I. V. Grigorieva, and A. A. Firsov, Science **306**, 666 (2004).

[36] S. D. Sarma, S. Adam, E. Hwang, and E. Rossi, Rev. Mod. Phys. **83**, 407 (2011).

[37] X. Wan, A. M. Turner, A. Vishwanath, and S. Y. Savrasov, Phys. Rev. B **83**, 205101 (2011).

[38] A. Burkov and L. Balents, Phys. Rev. Lett. **107**, 127205 (2011).

[39] O. Vafek and A. Vishwanath, Annu. Rev. Condens. Matter Phys. **5**, 83 (2014).

[40] L. He, X. Hong, J. Dong, J. Pan, Z. Zhang, J. Zhang, and S. Li, Phys. Rev. Lett. **113**, 246402 (2014).

[41] Z. Wang, H. Weng, Q. Wu, X. Dai, and Z. Fang, Phys. Rev. B **88**, 125427 (2013).

[42] S. Borisenko, Q. Gibson, D. Evtushinsky, V. Zabolotnyy, B. Büchner, and R. J. Cava, Phys. Rev. Lett. **113**, 027603 (2014).

[43] M. Neupane, S.-Y. Xu, R. Sankar, N. Alidoust, G. Bian, C. Liu, I. Belopolski, T.-R. Chang, H.-T. Jeng, H. Lin, et al., Nat. Commun. **5**, 3786 (2014).

[44] S. Jeon, B. B. Zhou, A. Gyenis, B. E. Feldman, I. Kimchi, A. C. Potter, Q. D. Gibson, R. J. Cava, A. Vishwanath, and A. Yazdani, Nat. Mater. **13**, 851 (2014).

[45] Z. Liu, J. Jiang, B. Zhou, Z. Wang, Y. Zhang, H. Weng, D. Prabhakaran, S. K. Mo, H. Peng, P. Dudin, et al., Nat. Mater. **13**, 677 (2014).

[46] Z. Wang, Y. Sun, X.-Q. Chen, C. Franchini, G. Xu, H. Weng, X. Dai, and Z. Fang, Phys. Rev. B **85**, 195320 (2012).

[47] Z. Liu, B. Zhou, Y. Zhang, Z. Wang, H. Weng, D. Prabhakaran, S.-K. Mo, Z. Shen, Z. Fang, X. Dai, et al., Science **343**, 864 (2014).

[48] Y. Zhang, Z. Liu, B. Zhou, Y. Kim, Z. Hussain, Z.-X. Shen, Y. Chen, and S.-K. Mo, Appl. Phys. Lett. **105**, 031901 (2014).

[49] M. Brahlek, N. Bansal, N. Koirala, S.-Y. Xu, M. Neupane, C. Liu, M. Z. Hasan, and S. Oh, Phys. Rev. Lett. **109**, 186403 (2012).

[50] L. Wu, M. Brahlek, R. V. Aguilar, A. Stier, C. Morris, Y. Lubashevsky, L. Bilbro, N. Bansal, S. Oh, and N. Armitage, Nat. Phys. **9**, 410 (2013).

[51] X. Huang, L. Zhao, Y. Long, P. Wang, D. Chen, Z. Yang, H. Liang, M. Xue, H. Weng, Z. Fang, et al., Phys. Rev. X **5**, 031023 (2015).

[52] B. Lv, H. Weng, B. Fu, X. Wang, H. Miao, J. Ma, P. Richard, X. Huang, L. Zhao, G. Chen, et al., Phys. Rev. X **5**, 031013 (2015).

[53] L. Yang, Z. Liu, Y. Sun, H. Peng, H. Yang, T. Zhang, B. Zhou, Y. Zhang, Y. Guo, M. Rahn, et al., Nat. Phys. **11**, 728 (2015).

[54] G. Xu, H. Weng, Z. Wang, X. Dai, and Z. Fang, Phys. Rev. Lett. **107**, 186806 (2011).

[55] H. Niesen and M. Ninomiya, Phys. Lett. B **105**, 219 (1981).

[56] S. L. Adler, Phys. Rev. **177**, 2426 (1969).

[57] J. Bell and J. R, Nuovo Cimento A **60**, 47 (1969).

[58] H. B. Nielsen and M. Ninomiya, Phys. Lett. B **130**, 389 (1983).

[59] A. Vilenkin, Phys. Rev. D **22**, 3080 (1980).

[60] M. A. Metlitski and A. R. Zhitnitsky, Phys. Rev. D **72**, 045011 (2005).

[61] A. Vilenkin, Phys. Rev. D **20**, 1807 (1979).

[62] K. Fukushima, D. E. Kharzeev, and H. J. Warringa, Phys. Rev. D **78**, 074033 (2008).

[63] Q. Li, D. E. Kharzeev, C. Zhang, Y. Huang, I. Pletikosić, A. Fedorov, R. Zhong, J. Schneeloch, G. Gu, and T. Valla, Nat. Phys. **12**, 550 (2016).

[64] D. Kharzeev, J. Liao, S. Voloshin, and G. Wang, Prog. Part. Nucl. Phys. **88**, 1 (2016).

[65] D. Son and B. Spivak, Phys. Rev. B **88**, 104412 (2013).

[66] A. Burkov, J. Phys. Condens. Matter **27**, 113201 (2015).

[67] A. Y. Alekseev, V. V. Cheianov, and J. Fröhlich, Phys. Rev. Lett. **81**, 3503 (1998).

[68] H.-J. Kim, K.-S. Kim, J.-F. Wang, M. Sasaki, N. Satoh, A. Ohnishi, M. Kitaura, M. Yang, and L. Li, Phys. Rev. Lett. **111**, 246603 (2013).

[69] J. Xiong, S. K. Kushwaha, T. Liang, J. W. Krizan, M. Hirschberger, W. Wang, R. Cava, and N. Ong, Science **350**, 413 (2015).

[70] C.-L. Zhang, S.-Y. Xu, I. Belopolski, Z. Yuan, Z. Lin, B. Tong, G. Bian, N. Alidoust, C.-C. Lee, S.-M. Huang, et al., Nat. Commun. **7**, 10735 (2016).

[71] A. Chen and M. Franz, Phys. Rev. B **93**, 201105 (2016).

[72] A. C. Potter, I. Kimchi, and A. Vishwanath, Nat. Commun. **5**, 5161 (2014).

[73] P. J. Moll, N. L. Nair, T. Helm, A. C. Potter, I. Kimchi, A. Vishwanath, and J. G. Analytis, Nature **535**, 266 (2016).

[74] A. P. Schnyder and P. M. Brydon, J. Phys. Condens. Matter **27**, 243201 (2015).

[75] L. Fu and E. Berg, Phys. Rev. Lett. **105**, 097001 (2010).

[76] M. Smylie, H. Claus, U. Welp, W.-K. Kwok, Y. Qiu, Y. S. Hor, and A. Snezhko, Phys. Rev. B **94**, 180510 (2016).

[77] K. Matano, M. Kriener, K. Segawa, Y. Ando, and G.-q. Zheng, Nat. Phys. **12**, 852 (2016).

[78] S. Yonezawa, K. Tajiri, S. Nakata, Y. Nagai, Z. Wang, K. Segawa, Y. Ando, and Y. Maeno, Nat. Phys. **13**, 123 (2016).

[79] L. Fu, Phys. Rev. B **90**, 100509 (2014).

[80] J. W. Venderbos, V. Kozii, and L. Fu, Phys. Rev. B **94**, 180504 (2016).

[81] N. Ashcroft and N. Mermin (Thomson Learning, 1976).

[82] F. Bloch, Z. Phys. **61**, 206 (1930).

[83] Y. Aharonov and A. Casher, Phys. Rev. Lett. **53**, 319 (1984).

[84] S. Owerre, Can. J. Phys. **96**, 1216 (2018).

[85] J. Cano, B. Bradlyn, Z. Wang, M. Hirschberger, N. Ong, and B. Bernevig, Phys. Rev. B **95**, 161306 (2017).

[86] Y. Aharonov and D. Bohm, Phys. Rev. **115**, 485 (1959).

[87] F. Guinea, M. Katsnelson, and A. Geim, Nat. Phys. **6**, 30 (2010).

[88] M. A. Vozmediano, M. Katsnelson, and F. Guinea, Phys. Rep. **496**, 109 (2010).

[89] N. Levy, S. Burke, K. Meaker, M. Panlasigui, A. Zettl, F. Guinea, A. C. Neto, and M. Crommie, Science **329**, 544 (2010).

[90] M. C. Rechtsman, J. M. Zeuner, A. Tünnermann, S. Nolte, M. Segev, and A. Szameit, Nat. Photonics **7**, 153 (2013).

[91] Y. Ferreiros and M. A. Vozmediano, Phys. Rev. B **97**, 054404 (2018).

[92] A. Cortijo, Y. Ferreirós, K. Landsteiner, and M. A. Vozmediano, Phys. Rev. Lett. **115**, 177202 (2015).

[93] H. Sumiyoshi and S. Fujimoto, Phys. Rev. Lett. **116**, 166601 (2016).

[94] D. Pikulin, A. Chen, and M. Franz, Phys. Rev. X **6**, 041021 (2016).

[95] A. G. Grushin, J. W. Venderbos, A. Vishwanath, and R. Ilan, Phys. Rev. X **6**, 041046 (2016).

[96] A. Cortijo, D. Kharzeev, K. Landsteiner, and M. A. Vozmediano, Phys. Rev. B **94**, 241405 (2016).

[97] V. Arjona, E. V. Castro, and M. A. Vozmediano, Phys. Rev. B **96**, 081110 (2017).

[98] N. Barišić, S. Badoux, M. K. Chan, C. Dorow, W. Tabis, B. Vignolle, G. Yu, J. Béard, X. Zhao, C. Proust, et al., Nat. Phys. **9**, 761 (2013).

[99] N. Doiron-Leyraud, C. Proust, D. LeBoeuf, J. Levallois, J.-B. Bonnemaison, R. Liang, D. Bonn, W. Hardy, and L. Taillefer, Nature **447**, 565 (2007).

[100] B. Ramshaw, B. Vignolle, J. Day, R. Liang, W. Hardy, C. Proust, and D. Bonn, Nat. Phys. **7**, 234 (2011).

[101] D. LeBoeuf, N. Doiron-Leyraud, J. Levallois, R. Daou, J. Bonnemaison, N. Hussey, L. Balicas, B. Ramshaw, R. Liang, D. Bonn, et al., Nature **450**, 533 (2007).

[102] G. Grissonnanche, O. Cyr-Choiniere, F. Laliberté, S. R. de Cotret, A. Juneau-Fecteau, S. Dufour-Beauséjour, N. Hussey, B. Vignolle, C. Proust, M. Sutherland, et al., Nature **5**, 3280 (2014).

[103] C. Jaudet, D. Vignolles, A. Audouard, J. Levallois, D. LeBoeuf, N. Doiron-Leyraud, B. Vignolle, M. Nardone, A. Zitouni, R. Liang, et al., Phys. Rev. Lett. **100**, 187005 (2008).

[104] S. Banerjee, S. Zhang, and M. Randeria, Nat. Commun. **4**, 1700 (2013).

[105] A. Alexandrov, J. Phys. Condens. Matter **20**, 192202 (2008).

[106] R. Corcoran, P. Meeson, Y. Onuki, P.-A. Probst, M. Springford, K. Takita, H. Harima, G. Guo, and B. Gyorffy, J. Phys. Condens. Matter **6**, 4479 (1994).

[107] S. Parameswaran, T. Grover, D. Abanin, D. Pesin, and A. Vishwanath, Phys. Rev. X **4**, 031035 (2014).

[108] Y. Baum, E. Berg, S. Parameswaran, and A. Stern, Phys. Rev. X **5**, 041046 (2015).

[109] H. Shapourian, T. L. Hughes, and S. Ryu, Phys. Rev. B **92**, 165131 (2015).

[110] Y. Liu, C. Zhang, X. Yuan, T. Lei, C. Wang, D. Di Sante, A. Narayan, L. He, S. Picozzi, S. Sanvito, et al., NPG Asia Materials **7**, e221 (2015).

[111] J. Xiong, S. Kushwaha, J. Krizan, T. Liang, R. Cava, and N. Ong, Europhys. Lett. **114**, 27002 (2016).

[112] D. Shoenberg (Cambridge University Press, Cambridge, 1984).

[113] S.-Y. Xu, I. Belopolski, N. Alidoust, M. Neupane, G. Bian, C. Zhang, R. Sankar, G. Chang, Z. Yuan, C.-C. Lee, et al., Science **349**, 613 (2015).

[114] C. Shekhar, A. K. Nayak, Y. Sun, M. Schmidt, M. Nicklas, I. Leermakers, U. Zeitler, Y. Skourski, J. Wosnitza, Z. Liu, et al., Nat. Phys. **11**, 645 (2015).

[115] S.-Y. Xu, N. Alidoust, I. Belopolski, Z. Yuan, G. Bian, T.-R. Chang, H. Zheng, V. N. Strocov, D. S. Sanchez, G. Chang, et al., Nat. Phys. **11**, 748 (2015).

[116] H. Li, H. He, H.-Z. Lu, H. Zhang, H. Liu, R. Ma, Z. Fan, S.-Q. Shen, and J. Wang, Nat. Commun. **7**, 10301 (2016).

[117] C.-Z. Li, L.-X. Wang, H. Liu, J. Wang, Z.-M. Liao, and D.-P. Yu, Nat. Commun. **6**, 10137 (2015).

[118] L.-X. Wang, C.-Z. Li, D.-P. Yu, and Z.-M. Liao, Nat. Commun. **7**, 10769 (2016).

[119] S. Doniach and E. H. Sondheimer (Imperial College Press, 1974).

[120] T. Ando and Y. Uemura, J. Phys. Soc. Jpn. **36**, 959 (1974).

[121] P. E. Ashby and J. Carbotte, Phys. Rev. B **87**, 245131 (2013).

[122] D. Neubauer, J. Carbotte, A. Nateprov, A. Löhle, M. Dressel, and A. Pronin, Phys. Rev. B **93**, 121202 (2016).

[123] T. Liang, Q. Gibson, M. N. Ali, M. Liu, R. Cava, and N. Ong, Nat. mater. **14**, 280 (2015).

[124] M. Hakl, S. Tchoumakov, I. Crassee, A. Akrap, B. Piot, C. Faugeras, G. Martinez, A. Nateprov, E. Arushanov, F. Teppe, et al., Phys. Rev. B **97**, 115206 (2018).

[125] J. G. Checkelsky, Y. S. Hor, M.-H. Liu, D.-X. Qu, R. J. Cava, and N. Ong, Phys. Rev. Lett. **103**, 246601 (2009).

[126] A. Taskin and Y. Ando, Phys. Rev. B **80**, 085303 (2009).

[127] K. Eto, Z. Ren, A. Taskin, K. Segawa, and Y. Ando, Phys. Rev. B **81**, 195309 (2010).

[128] J. G. Analytis, J.-H. Chu, Y. Chen, F. Corredor, R. D. McDonald, Z. Shen, and I. R. Fisher, Phys. Rev. B **81**, 205407 (2010).

[129] D.-X. Qu, Y. S. Hor, J. Xiong, R. J. Cava, and N. Ong, Science **329**, 821 (2010).

[130] A. Potter, I. Kimchi, and A. Vishwanath, Nat. Commun. **5**, 5161 (2013).

[131] M. Franz and Z. Tešanović, Phys. Rev. Lett. **84**, 554 (2000).

[132] O. Vafek, A. Melikyan, M. Franz, and Z. Tešanović, Phys. Rev. B **63**, 134509 (2001).

[133] T. Liu and M. Franz, Phys. Rev. B **92**, 134519 (2015).

[134] T. Liu, D. Pikulin, and M. Franz, Phys. Rev. B **95**, 041201 (2017).

[135] T. Matsushita, T. Liu, T. Mizushima, and S. Fujimoto, Phys. Rev. B **97**, 134519 (2018).

[136] G. Massarelli, G. Wachtel, J. Y. Wei, and A. Paramekanti, Phys. Rev. B **96**, 224516 (2017).

[137] E. M. Nica and M. Franz, Phys. Rev. B **97**, 024520 (2018).

[138] B. Reznik and Y. Aharonov, Phys. Rev. D **40**, 4178 (1989).

[139] M. Pacholski, C. Beenakker, and İ. Adagideli, Phys. Rev. Lett. **121**, 037701 (2018).

[140] J. M. Murray and O. Vafek, Phys. Rev. B **92**, 134520 (2015).

[141] H. Sumiyoshi and S. Fujimoto, J. Phys. Soc. Jpn. **82**, 023602 (2013).

[142] Z. Wang, X.-L. Qi, and S.-C. Zhang, Phys. Rev. B **84**, 014527 (2011).

[143] N. Ong, K. Krishana, Y. Zhang, and Z. Xu, Physics and Chemistry of Transition Metal Oxides **125**, 202 (1999).

[144] J. Bardeen, G. Rickayzen, and L. Tewordt, Phys. Rev. **113**, 982 (1959).

[145] L. Tewordt, Phys. Rev. **128**, 12 (1962).

[146] S.-P. Lee, D. Nandi, F. Marsiglio, and J. Maciejko, Phys. Rev. B **95**, 174517 (2017).

[147] T. Holstein and H. Primakoff, Phys. Rev. **58**, 1098 (1940).

[148] B. Brockhouse, Phys. Rev. **106**, 859 (1957).

[149] K. Nakata, K. A. van Hoogdalem, P. Simon, and D. Loss, Phys. Rev. B **90**, 144419 (2014).

[150] K. Nakata, J. Klinovaja, and D. Loss, Phys. Rev. B **95**, 125429 (2017).

[151] K. Nakata, P. Simon, and D. Loss, Phys. Rev. B **92**, 134425 (2015).

[152] P. Laurell and G. A. Fiete, Phys. Rev. B **98**, 094419 (2018).

[153] R. Matsumoto, R. Shindou, and S. Murakami, Phys. Rev. B **89**, 054420 (2014).

[154] L. Zhang, J. Ren, J.-S. Wang, and B. Li, Phys. Rev. B **87**, 144101 (2013).

[155] R. Matsumoto and S. Murakami, Phys. Rev. Lett. **106**, 197202 (2011).

[156] H. Katsura, N. Nagaosa, and P. A. Lee, Phys. Rev. Lett. **104**, 066403 (2010).

[157] Y. Onose, T. Ideue, H. Katsura, Y. Shiomi, N. Nagaosa, and Y. Tokura, Science **329**, 297 (2010).

[158] J. Xiao, G. E. Bauer, K.-c. Uchida, E. Saitoh, S. Maekawa, et al., Phys. Rev. B **81**, 214418 (2010).

[159] S. Rezende, R. Rodríguez-Suárez, R. Cunha, A. Rodrigues, F. Machado, G. F. Guerra, J. L. Ortiz, and A. Azevedo, Phys. Rev. B **89**, 014416 (2014).

[160] K.-i. Uchida, H. Adachi, T. An, T. Ota, M. Toda, B. Hillebrands, S. Maekawa, and E. Saitoh, Nat. Mater. **10**, 737 (2011).

[161] K. Uchida, J. Xiao, H. Adachi, J.-i. Ohe, S. Takahashi, J. Ieda, T. Ota, Y. Kajiwara, H. Umezawa, H. Kawai, et al., Nat. Mater. **9**, 894 (2010).

[162] K. Uchida, S. Takahashi, K. Harii, J. Ieda, W. Koshibae, K. Ando, S. Maekawa, and E. Saitoh, Nature **455**, 778 (2008).

[163] A. A. Kovalev and Y. Tserkovnyak, Europhys. Lett. **97**, 67002 (2012).

[164] J. Flipse, F. Dejene, D. Wagenaar, G. Bauer, J. B. Youssef, and B. Van Wees, Phys. Rev. Lett. **113**, 027601 (2014).

[165] R. Cheng, S. Okamoto, and D. Xiao, Phys. Rev. Lett. **117**, 217202 (2016).

[166] V. A. Zyuzin and A. A. Kovalev, Phys. Rev. Lett. **117**, 217203 (2016).

[167] A. A. Kovalev and V. Zyuzin, Phys. Rev. B **93**, 161106 (2016).

[168] Y. Shiomi, R. Takashima, and E. Saitoh, Phys. Rev. B **96**, 134425 (2017).

[169] B. Huang, G. Clark, E. Navarro-Moratalla, D. R. Klein, R. Cheng, K. L. Seyler, D. Zhong, E. Schmidgall, M. A. McGuire, D. H. Cobden, et al., Nature **546**, 270 (2017).

[170] S. S. Pershoguba, S. Banerjee, J. Lashley, J. Park, H. Ågren, G. Aeppli, and A. V. Balatsky, Phys. Rev. X **8**, 011010 (2018).

[171] I. Dzyaloshinsky, J. Phys. Chem. Solids **4**, 241 (1958).

[172] T. Moriya, Phys. Rev. **120**, 91 (1960).

[173] F. Meier and D. Loss, Phys. Rev. Lett. **90**, 167204 (2003).

[174] L.-S. Xie, G.-X. Jin, L. He, G. E. Bauer, J. Barker, and K. Xia, Phys. Rev. B **95**, 014423 (2017).

[175] R. Douglass, Phys. Rev. **129**, 1132 (1963).

[176] T. Liu, M. Franz, and S. Fujimoto, Phys. Rev. B **96**, 224518 (2017).

# Appendix A

# Electronic structure of Dirac semimetal $Cd_3As_2$

In Chapter 2, we have elaborated that a 2-band toy model of Weyl semimetal – $\frac{1}{2}$-$Cd_3As_2$, which is the spin-up sector of Dirac semimetal $Cd_3As_2$, exhibits quantum oscillations in the presence of continuously tuned bend deformation but in the absence of ordinary magnetic field. In this section, we argue that similar zero-field quantum oscillations can be realized in Dirac semimetal $Cd_3As_2$. And we will verify our argument by examining the band structure of $Cd_3As_2$.

We model $Cd_3As_2$ using Hamiltonian Eq. 2.1 with parameters taken from first principles band structure calculation [85]. We use rectangular lattice, which captures the actual geometry of the crystal lattice of $Cd_3As_2$, rather than assuming cubic lattice as we did in Section 2.1. The lattice constants are $a_x = a_y = 3\text{Å}$ and $a_z = 5\text{Å}$. The other parameters to be used in Eq. 2.1 are listed in Table. A.1.

Table A.1: Parameters of Dirac semimetal $Cd_3As_2$. All quantities are measured in terms of electron volt (eV).

| $t_0$ | $t_1$ | $t_2$ | $\Lambda$ | $r_0$ | $r_1$ | $r_2$ |
|---|---|---|---|---|---|---|
| -7.8411 | 1.5016 | 3.0 | 0.296 | 5.9439 | -0.8472 | -2.5556 |

The results for the energy dispersion and DOS for the realistic particle-hole asymmetric case are shown in Fig. A.1. We note the similarity to the results displayed in Fig. 2.3 in Section 2.3. Specifically, both ordinary magnetic field $\boldsymbol{B}$ and strain-induced pseudo-magnetic field $\boldsymbol{b}$ give rise to pronounced Landau levels. We thus conclude that all our predictions remain valid for the Dirac semimetal $Cd_3As_2$.

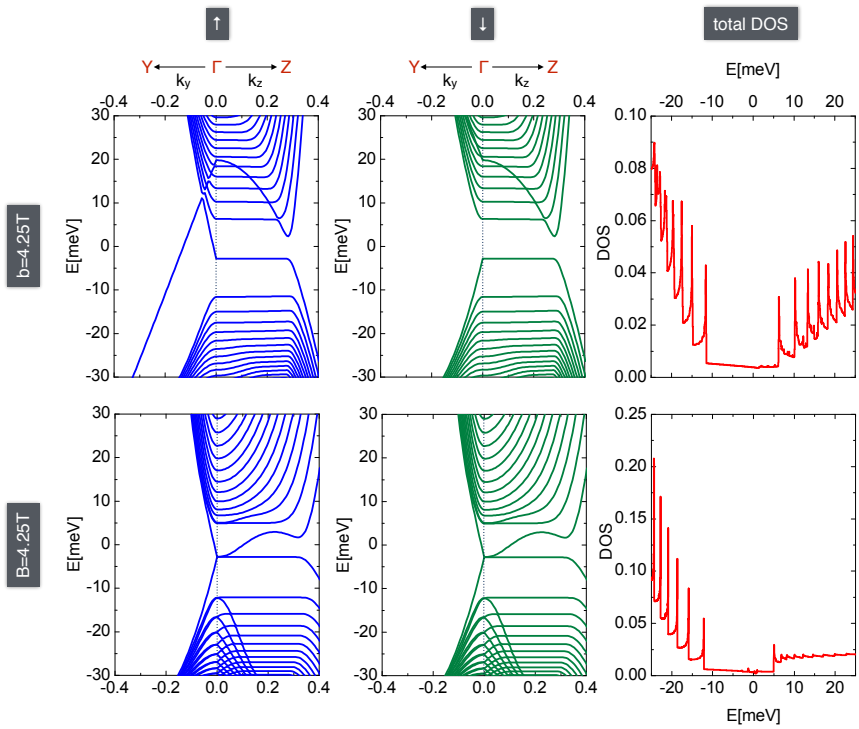


Figure A.1: Numerically calculated band structure and density of states for Dirac semimetal $Cd_3As_2$ with both spin sectors and particle-hole asymmetric term $\epsilon_{\boldsymbol{k}}$ considered. Top row is for the pseudo-magnetic field $b = 4.25$T and the bottom row is for the ordinary magnetic field $B = 4.25$T. From left to right – band structure of spin up sector, band structure of spin down sector, and normalized total DOS. The appearance of Landau levels is obviously showed in all panels.

# Appendix B

# Weyl superconductor with a vortex lattice

In this section we study Weyl superconductors under ordinary magnetic field $\boldsymbol{B}$ and compare the results to Section 3.2. Due to the Meissner effect, $\boldsymbol{B}$ field is known to generate quasiparticle Bloch waves rather than Dirac-Landau levels in 2D nodal superconductors, such as those with a $d$-wave symmetry of the gap function [131, 132]. It is however not known how this result translates to three-dimensional Weyl SC.

We consider magnetic field along $z$-direction, so that $k_z$ remains a good quantum number. Thus, the system can, in principle, stay gapless. To study the vortex lattice, we write Eq. 3.1 as

$$H = \frac{1}{2}\sum_{\boldsymbol{k}} \Psi_{\boldsymbol{r}}^{\dagger}\mathcal{H}_{\boldsymbol{r}}\Psi_{\boldsymbol{r}} = \frac{1}{2}\sum_{\boldsymbol{k}} \Psi_{\boldsymbol{r}}^{\dagger}\begin{pmatrix}\mathcal{H}_{\boldsymbol{r}}^{11} & \mathcal{H}_{\boldsymbol{r}}^{12}\\ \mathcal{H}_{\boldsymbol{r}}^{21} & \mathcal{H}_{\boldsymbol{r}}^{22}\end{pmatrix}\Psi_{\boldsymbol{r}}, \tag{B.1}$$

with the real space basis to be written as $\Psi_{\boldsymbol{r}} = (c_{\boldsymbol{r},\uparrow,1}, c_{\boldsymbol{r},\downarrow,1}, c_{\boldsymbol{r},\uparrow,2}, c_{\boldsymbol{r},\downarrow,2}, c^{\dagger}_{\boldsymbol{r},\uparrow,1}, c^{\dagger}_{\boldsymbol{r},\downarrow,1}, c^{\dagger}_{\boldsymbol{r},\uparrow,2}, c^{\dagger}_{\boldsymbol{r},\downarrow,2})^T$ and the blocks are defined as

$$\mathcal{H}_{\boldsymbol{r}}^{11} = \begin{pmatrix} m-4b+b\sum_{\boldsymbol{\delta}}\hat{s}_{\boldsymbol{\delta}} & -i\frac{\hbar v_F}{2a}\sum_{\boldsymbol{\delta}}\hat{\eta}^*_{\boldsymbol{\delta}} & t_s+t_d e^{-ik_z a} & 0\\ -i\frac{\hbar v_F}{2a}\sum_{\boldsymbol{\delta}}\hat{\eta}_{\boldsymbol{\delta}} & -m+4b-b\sum_{\boldsymbol{\delta}}\hat{s}_{\boldsymbol{\delta}} & 0 & t_s+t_d e^{-ik_z a}\\ t_s+t_d e^{ik_z a} & 0 & m-4b+b\sum_{\boldsymbol{\delta}}\hat{s}_{\boldsymbol{\delta}} & i\frac{\hbar v_F}{2a}\sum_{\boldsymbol{\delta}}\hat{\eta}^*_{\boldsymbol{\delta}}\\ 0 & t_s+t_d e^{ik_z a} & i\frac{\hbar v_F}{2a}\sum_{\boldsymbol{\delta}}\hat{\eta}_{\boldsymbol{\delta}} & -m+4b-b\sum_{\boldsymbol{\delta}}\hat{s}_{\boldsymbol{\delta}}\end{pmatrix}, \tag{B.2}$$

$$\mathcal{H}_{\boldsymbol{r}}^{22} = \begin{pmatrix} -m+4b-b\sum_{\boldsymbol{\delta}}\hat{s}_{\boldsymbol{\delta}} & -i\frac{\hbar v_F}{2a}\sum_{\boldsymbol{\delta}}\hat{\eta}_{\boldsymbol{\delta}} & -t_s-t_d e^{-ik_z a} & 0\\ -i\frac{\hbar v_F}{2a}\sum_{\boldsymbol{\delta}}\hat{\eta}^*_{\boldsymbol{\delta}} & m-4b+b\sum_{\boldsymbol{\delta}}\hat{s}_{\boldsymbol{\delta}} & 0 & -t_s-t_d e^{-ik_z a}\\ -t_s-t_d e^{ik_z a} & 0 & -m+4b-b\sum_{\boldsymbol{\delta}}\hat{s}_{\boldsymbol{\delta}} & i\frac{\hbar v_F}{2a}\sum_{\boldsymbol{\delta}}\hat{\eta}_{\boldsymbol{\delta}}\\ 0 & -t_s-t_d e^{ik_z a} & i\frac{\hbar v_F}{2a}\sum_{\boldsymbol{\delta}}\hat{\eta}^*_{\boldsymbol{\delta}} & m-4b+b\sum_{\boldsymbol{\delta}}\hat{s}_{\boldsymbol{\delta}}\end{pmatrix}, \tag{B.3}$$

$$\mathcal{H}_{\boldsymbol{r}}^{12} = \begin{pmatrix} 0 & \Delta & 0 & 0\\ -\Delta & 0 & 0 & 0\\ 0 & 0 & 0 & \Delta\\ 0 & 0 & -\Delta & 0\end{pmatrix}, \qquad \mathcal{H}_{\boldsymbol{r}}^{21} = \begin{pmatrix} 0 & -\Delta^* & 0 & 0\\ \Delta^* & 0 & 0 & 0\\ 0 & 0 & 0 & -\Delta^*\\ 0 & 0 & \Delta^* & 0\end{pmatrix}. \tag{B.4}$$

Here the shift operator is defined as

$$\hat{s}_{\boldsymbol{\delta}} f(\boldsymbol{r}) = f(\boldsymbol{r} + \boldsymbol{\delta}) \qquad \boldsymbol{\delta} = \pm a\hat{x}, \pm a\hat{y}, \tag{B.5}$$

and

$$\hat{\eta}_{\boldsymbol{\delta}} = \begin{cases} \mp i\hat{s}_{\boldsymbol{\delta}} & \text{if } \boldsymbol{\delta} = \pm a\hat{x} \\ \pm \hat{s}_{\boldsymbol{\delta}} & \text{if } \boldsymbol{\delta} = \pm a\hat{y} \end{cases}. \tag{B.6}$$

To model vortex lattice, the phase of $\Delta(\boldsymbol{r}) = \Delta_0 e^{i\phi(\boldsymbol{r})}$ is taken to wind by $2\pi$ around each vortex center. We solve the problem by performing a unitary transformation [131] in the Nambu space defined by

$$U = \begin{pmatrix} e^{i\phi_A(\boldsymbol{r})} & 0 \\ 0 & e^{-i\phi_B(\boldsymbol{r})} \end{pmatrix}, \tag{B.7}$$

where we have partitioned vortices into two sublattices A and B such that $\phi_A(\boldsymbol{r}) + \phi_B(\boldsymbol{r}) = \phi(\boldsymbol{r})$. This removes the phase winding from the off-diagonal part of the Hamiltonian and makes it periodic in real space with a unit cell depicted in Fig. B.1.

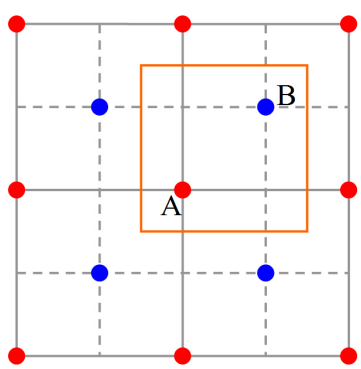


Figure B.1: Schematic plot of square vortex lattice. The red and blue dots correspond to two vortex sublattices. The orange square is the magnetic unit cell with vortices placed on the diagonal. The dimension of the magnetic unit cell is chosen to be $L = 30a$ in the simulation.

The eigenstates of the transformed Hamiltonian are Bloch waves [131–133] that read $\Phi_{n\boldsymbol{K}}(\boldsymbol{r}) = e^{i\boldsymbol{K}\cdot\boldsymbol{r}}[U_{n\boldsymbol{K}}(\boldsymbol{r}), V_{n\boldsymbol{K}}(\boldsymbol{r})]^T$ with crystal momentum $\boldsymbol{K}$ associated with the vortex lattice (Fig. B.1). The BdG type Bloch Hamiltonian is $H_{\boldsymbol{K}} = e^{-i\boldsymbol{K}\cdot\boldsymbol{r}} U^{-1} H_{\boldsymbol{r}} U e^{i\boldsymbol{K}\cdot\boldsymbol{r}}$ with its 4 blocks $H^{ij}_{\boldsymbol{K}} = e^{-i\boldsymbol{K}\cdot\boldsymbol{r}} U^{-1} H^{ij}_{\boldsymbol{r}} U e^{i\boldsymbol{K}\cdot\boldsymbol{r}}$

defined as

$$\mathcal{H}_{\boldsymbol{K}}^{11} = \begin{pmatrix} m-4b+b\sum_{\boldsymbol{\delta}} e^{i\boldsymbol{K}\cdot\boldsymbol{\delta}} e^{i\mathcal{V}_{\boldsymbol{\delta}}^{A}} \hat{s}_{\boldsymbol{\delta}} & -i\frac{\hbar v_F}{2a}\sum_{\boldsymbol{\delta}} e^{i\boldsymbol{K}\cdot\boldsymbol{\delta}} e^{i\mathcal{V}_{\boldsymbol{\delta}}^{A}} \hat{\eta}_{\boldsymbol{\delta}}^{*} & t_s+t_d e^{ik_z a} & 0 & t_s+t_d e^{-ik_z a} & 0 \\ -i\frac{\hbar v_F}{2a}\sum_{\boldsymbol{\delta}} e^{i\boldsymbol{K}\cdot\boldsymbol{\delta}} e^{i\mathcal{V}_{\boldsymbol{\delta}}^{A}} \hat{\eta}_{\boldsymbol{\delta}} & -m+4b-b\sum_{\boldsymbol{\delta}} e^{i\boldsymbol{K}\cdot\boldsymbol{\delta}} e^{i\mathcal{V}_{\boldsymbol{\delta}}^{A}} \hat{s}_{\boldsymbol{\delta}} & 0 & t_s+t_d e^{ik_z a} & 0 & t_s+t_d e^{-ik_z a} \\ t_s+t_d e^{-ik_z a} & 0 & m-4b+b\sum_{\boldsymbol{\delta}} e^{i\boldsymbol{K}\cdot\boldsymbol{\delta}} e^{i\mathcal{V}_{\boldsymbol{\delta}}^{A}} \hat{s}_{\boldsymbol{\delta}} & i\frac{\hbar v_F}{2a}\sum_{\boldsymbol{\delta}} e^{i\boldsymbol{K}\cdot\boldsymbol{\delta}} e^{i\mathcal{V}_{\boldsymbol{\delta}}^{A}} \hat{\eta}_{\boldsymbol{\delta}}^{*} \\ 0 & t_s+t_d e^{-ik_z a} & i\frac{\hbar v_F}{2a}\sum_{\boldsymbol{\delta}} e^{i\boldsymbol{K}\cdot\boldsymbol{\delta}} e^{i\mathcal{V}_{\boldsymbol{\delta}}^{A}} \hat{\eta}_{\boldsymbol{\delta}} & -m+4b-b\sum_{\boldsymbol{\delta}} e^{i\boldsymbol{K}\cdot\boldsymbol{\delta}} e^{i\mathcal{V}_{\boldsymbol{\delta}}^{A}} \hat{s}_{\boldsymbol{\delta}} \end{pmatrix}, \tag{B.8}$$

$$\mathcal{H}_{\boldsymbol{K}}^{22} = \begin{pmatrix} -m+4b-b\sum_{\boldsymbol{\delta}} e^{i\boldsymbol{K}\cdot\boldsymbol{\delta}} e^{-i\mathcal{V}_{\boldsymbol{\delta}}^{B}} \hat{s}_{\boldsymbol{\delta}} & -i\frac{\hbar v_F}{2a}\sum_{\boldsymbol{\delta}} e^{i\boldsymbol{K}\cdot\boldsymbol{\delta}} e^{-i\mathcal{V}_{\boldsymbol{\delta}}^{B}} \hat{\eta}_{\boldsymbol{\delta}} & -t_s-t_d e^{ik_z a} & 0 & -t_s-t_d e^{-ik_z a} & 0 \\ -i\frac{\hbar v_F}{2a}\sum_{\boldsymbol{\delta}} e^{i\boldsymbol{K}\cdot\boldsymbol{\delta}} e^{-i\mathcal{V}_{\boldsymbol{\delta}}^{B}} \hat{\eta}_{\boldsymbol{\delta}}^{*} & m-4b+b\sum_{\boldsymbol{\delta}} e^{i\boldsymbol{K}\cdot\boldsymbol{\delta}} e^{-i\mathcal{V}_{\boldsymbol{\delta}}^{B}} \hat{s}_{\boldsymbol{\delta}} & 0 & -t_s-t_d e^{ik_z a} & 0 & -t_s-t_d e^{-ik_z a} \\ -t_s-t_d e^{-ik_z a} & 0 & -m+4b-b\sum_{\boldsymbol{\delta}} e^{i\boldsymbol{K}\cdot\boldsymbol{\delta}} e^{-i\mathcal{V}_{\boldsymbol{\delta}}^{B}} \hat{s}_{\boldsymbol{\delta}} & i\frac{\hbar v_F}{2a}\sum_{\boldsymbol{\delta}} e^{i\boldsymbol{K}\cdot\boldsymbol{\delta}} e^{-i\mathcal{V}_{\boldsymbol{\delta}}^{B}} \hat{\eta}_{\boldsymbol{\delta}} \\ 0 & -t_s-t_d e^{-ik_z a} & i\frac{\hbar v_F}{2a}\sum_{\boldsymbol{\delta}} e^{i\boldsymbol{K}\cdot\boldsymbol{\delta}} e^{-i\mathcal{V}_{\boldsymbol{\delta}}^{B}} \hat{\eta}_{\boldsymbol{\delta}}^{*} & m-4b+b\sum_{\boldsymbol{\delta}} e^{i\boldsymbol{K}\cdot\boldsymbol{\delta}} e^{-i\mathcal{V}_{\boldsymbol{\delta}}^{B}} \hat{s}_{\boldsymbol{\delta}} \end{pmatrix}, \tag{B.9}$$

$$\mathcal{H}_{\boldsymbol{K}}^{12} = \begin{pmatrix} 0 & \Delta & 0 & 0 \\ -\Delta & 0 & 0 & 0 \\ 0 & 0 & 0 & \Delta \\ 0 & 0 & -\Delta & 0 \end{pmatrix}, \tag{B.10}$$

$$\mathcal{H}_{\boldsymbol{K}}^{21} = \begin{pmatrix} 0 & -\Delta^* & 0 & 0 \\ \Delta^* & 0 & 0 & 0 \\ 0 & 0 & 0 & -\Delta^* \\ 0 & 0 & \Delta^* & 0 \end{pmatrix}, \tag{B.11}$$

where the phase factors associated with two types of vortices are

$$\mathcal{V}_{\boldsymbol{\delta}}^{\mu} = \frac{m}{\hbar}\int_{\boldsymbol{r}}^{\boldsymbol{r}+\boldsymbol{\delta}} \boldsymbol{v}_s^{\mu}(\boldsymbol{r})\cdot d\boldsymbol{l} \qquad \mu = A, B. \tag{B.12}$$

The integral is along the bond connecting lattice point $\boldsymbol{r}$ to its nearest neighbor $\boldsymbol{r}+\boldsymbol{\delta}$. The superfluid velocity is

$$\boldsymbol{v}_s^{\mu}(\boldsymbol{r}) = \frac{\hbar}{m}\big(\nabla\phi^{\mu} - \frac{e}{\hbar}\boldsymbol{A}(\boldsymbol{r})\big) \qquad \mu = A, B. \tag{B.13}$$

Following the standard derivation [132] an expression for $\mathcal{V}_{\boldsymbol{\delta}}^{\mu}$ can be derived in terms of summation over the reciprocal lattice vectors $\boldsymbol{G}$ of the vortex lattice,

$$\mathcal{V}_{\boldsymbol{\delta}}^{\mu}(\boldsymbol{r}) = \frac{2\pi}{L^2}\sum_{\boldsymbol{G}}\int_{\boldsymbol{r}}^{\boldsymbol{r}+\boldsymbol{\delta}} e^{i\boldsymbol{G}\cdot(\boldsymbol{r}-\boldsymbol{\delta}^{\mu})}\frac{i\boldsymbol{G}\times\hat{z}}{G^2}\cdot d\boldsymbol{l}. \tag{B.14}$$

We apply Eq. B.14 to the real space Hamiltonian $H_{\boldsymbol{r}}$ and exactly diagonalize $H_{\boldsymbol{r}}$ for various vortex lattice configurations. The dispersions along the $k_z$-axis are summarized in Fig. B.2(a-c). We observe that the Weyl points survive as we change the A-B vortex distance within each unit cell. Surprisingly, the variation of the vortex positions barely changes the dispersion. Therefore, we conclude that the $k_z$ component of the Weyl dispersion is stable under magnetic field $B$ as long as vortices form a periodic lattice.

Dispersion in the $K_x - K_y$ plane however changes dramatically. In Fig. B.2(d-f), we plot dispersions along $K_x$ for the vortex configurations used in panels (a-c). We see that the energy bands are reorganized into almost completely flat Dirac-Landau levels which are qualitatively similar to those reported by Ref. [139]. For comparison we also indicate the expected energies $\sim \sqrt{n}$ of Dirac-Landau levels (orange curves) by matching to the $n = 0, 1$ bands. It is worth noting that the deviation of numerically calculated bands (green curves) from the ideal $\sqrt{n}$ sequence is due to the fact that Dirac-Landau levels exist only in the low-energy regime in the vicinity of the Weyl points. For our model, Lifshitz transition occurs at $E_{\mathrm{Lif}} = 0.138$. Therefore, we do not expect a perfect match to the $\sqrt{n}$ behavior beyond the lowest few energy levels.

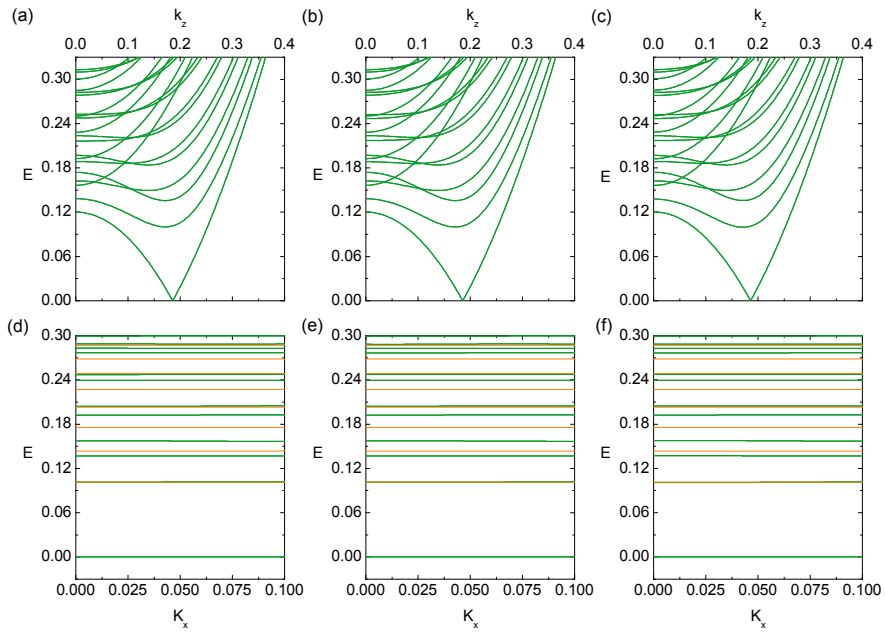


Figure B.2: Spectra of Weyl superconductor with vortex lattice. The size of magnetic unit cell is $L \times L = 30a \times 30a$. The spacings between two vortices in the magnetic unit cell are (a) $\boldsymbol{d} = (15a, 15a)$ (b) $\boldsymbol{d} = (10a, 10a)$ (c) $\boldsymbol{d} = (5a, 5a)$ (d) $\boldsymbol{d} = (15a, 15a)$ (e) $\boldsymbol{d} = (10a, 10a)$ (f) $\boldsymbol{d} = (5a, 5a)$ The orange curves in panel (d)-(f) are analytical Dirac-Landau levels with $n = 1$ band matched to the numerics.

# Appendix C

# Weyl ferromagnets under electric field and strain

In Chapter 4, we have seen that the magnon bands of the Weyl ferromagnet can be Landau-quantized by either applying an inhomogeneous electric field $\boldsymbol{E}$ (Section 4.2.1) or applying a twist which induces an inhomogeneous pseudo-electric field $\boldsymbol{e}^{\eta}$ (Section 4.2.2). The former acts on the whole Weyl ferromagnet, while the latter only couples to Weyl magnons and is greatly suppressed at higher energies where the "Diracness" of magnon bands is no longer preserved. Moreover, the pseudo-electric field is chiral and oppositely couples to different Weyl cones, resulting in two identically dispersing zeroth Landau levels, as illustrated in Fig. 4.6.

We now further test the chiral nature of the strain-induced pseudo-electric field $\boldsymbol{e}^{\eta} = \eta \boldsymbol{e}$. When an inhomogeneous electric field $\boldsymbol{E}$ is applied in addition to the twist, the effective electric field for the right (left) magnon Weyl cone is $\boldsymbol{E}_R = \boldsymbol{E} + \boldsymbol{e}$ ($\boldsymbol{E}_L = \boldsymbol{E} - \boldsymbol{e}$). For the special case that $\boldsymbol{E} = \boldsymbol{e}$, the left magnon Weyl cone feels no electric field but the electric field at the right magnon Weyl cone is doubled. Therefore, the left Weyl cone is unchanged but the right Weyl cone is Landau-quantized as illustrated in Fig. C.1(c). Compared to Fig. 4.4(c) and Fig. 4.6(c), the number of magnon Dirac-Landau levels in Fig. C.1(c) is halved due to the doubling of the effective electric field. These Dirac-Landau levels correspond to the even order Landau levels ($n = 2, 4, \cdots$) in Fig. 4.4(c) and Fig. 4.6(c).

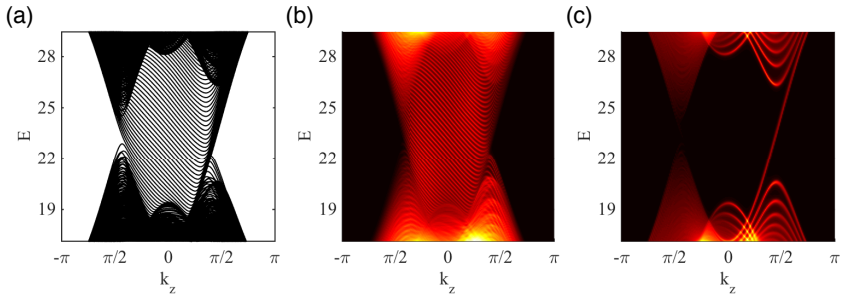


Figure C.1: Magnon dispersion for a twisted Weyl ferromagnet nanowire in the presence of an inhomogeneous electric field. For all panels, we take $\frac{g\mu_B \mathcal{E} a^2}{ec^2} = \frac{g\mu_B \varepsilon a^2}{ec^2} = -0.0124\Phi_0$. (a) Magnon band structure. Due to the chiral nature of the strain-induced pseudo-electric field, the effective electric field at the left Weyl cone vanishes while the effective field at the right Weyl cone is doubled. Therefore, the left Weyl cone is not Landau-quantized but the right Weyl cone exhibits Dirac-Landau levels. (b) Surface spectral function, which shows a set of left-moving surface states connecting the left Weyl cone and the right zeroth Landau level. (c) Bulk spectral function, which clearly unveils the linear band touching at the left Weyl cone, and Dirac-Landau levels at the right Weyl cone. Compared to Fig. 4.4(c) and Fig. 4.6(c), the Landau level spacing is doubled due to the doubling of the effective electric field.

# Appendix D

# Magnon bands of multilayer Weyl ferromagnets

In Chapter 4, we have neglected the $J_+(1-\cos k_z a)S\sigma^0$ term in the first-quantized Bloch Hamiltonian $\mathcal{H}_{\boldsymbol{k}}$ (Eq. 4.7) for ease of presentation. (We have carefully ensured that the magnon energy remains positive-definite relative to the ferromagnetic ground state.) In general, however, $J_+ > 0$ because the couplings $J_A$ and $J_B$ are both ferromagnetic. For this reason, we add the $J_+$ term back in this section and discuss its effects on the magnon band structure, pumping, and transport.

First, we examine the magnon band structure with the advent of the $J_+$ term. In the absence of an inhomogeneous electric field and strain, this term only shifts the magnon bands in Fig. 4.2 by $J_+(1-\cos k_z a)S$ without altering the band topology. Thus the Chern number (Eq. 4.11) is still valid and guarantees that there are surface states akin to Fermi arcs connecting the magnon Weyl cones. When a transverse inhomogeneous electric field $\boldsymbol{E} = (\frac{1}{2}\mathcal{E}x, \frac{1}{2}\mathcal{E}y, 0)$ is switched on, Aharonov-Casher phases must be added to the magnon "hopping" terms (the first three terms of Eq. 4.7). However, the diagonal term $m_{\boldsymbol{k}}\sigma^0 = [K_+ + J_+(1-\cos k_z a) + 3J_1 + 6J_2]S\sigma^0$ corresponds to an "on-site" magnon energy whose Aharonov-Casher phase is zero; thus the $J_+$ term is invariant under the electric field. On the other hand, when a static twist is applied, an extra term $\delta\mathcal{H}^{\boldsymbol{e}}_{\boldsymbol{k}}$ must be added to the first-quantized Bloch Hamiltonian $\mathcal{H}_{\boldsymbol{k}}$, but as shown in Eq. 4.17, $J_+$ does not contribute to $\delta\mathcal{H}^{\boldsymbol{e}}_{\boldsymbol{k}}$. Therefore, even in the presence of (pseudo-)electric fields, the effect of the $J_+$ term is simply shifting the magnon bands in Fig. 4.4, Fig. 4.6 and Fig. C.1 by $J_+(1-\cos k_z a)S$. The magnon band structure in the presence of the $J_+$ term is summarized in Fig. D.1.

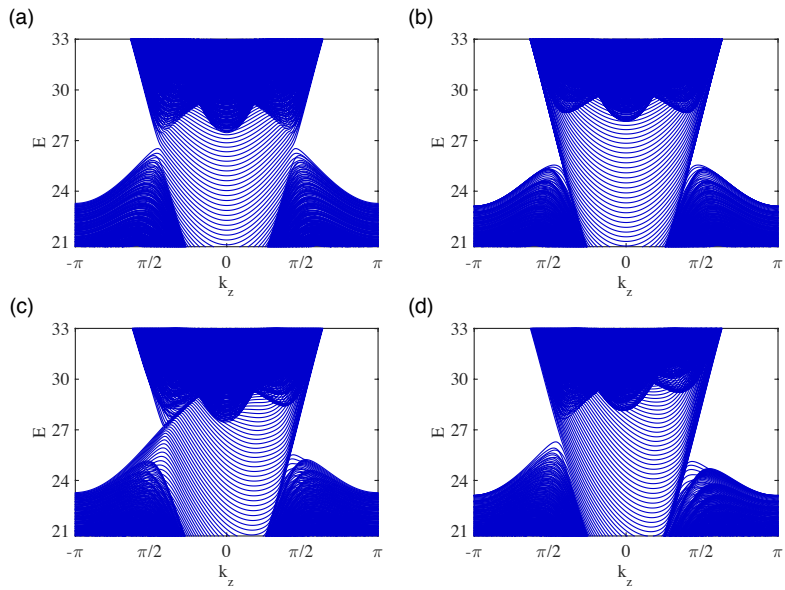


Figure D.1: Magnon dispersion for the Weyl ferromagnet nanowire. For all panels, the parameters are same as those of Fig. 4.2 in Chapter 4 except that we reintroduce a nonzero $J_+S = 4.08$. (a) Magnon band structure of a nanowire without external fields. Due to the nonzero $J_+$ the Weyl cones and arc states are tilted. (b) Magnon band structure of a nanowire under an inhomogeneous external electric field whose gradient $\mathcal{E}$ satisfies $\frac{g\mu_B\mathcal{E}a^2}{ec^2} = -0.0124\Phi_0$. The Dirac-Landau levels are tilted by $J_+$ such that the velocity of the right (left) zeroth Landau level is $|v_z^\eta|+|v_0^\eta|$ $(-|v_z^\eta|-|v_0^\eta|)$. (c) Magnon band structure of a twisted nanowire. The gradient of the strain-induced pseudo-electric field $\varepsilon$ satisfies $\frac{g\mu_B\varepsilon a^2}{ec^2} = -0.0124\Phi_0$. The Dirac-Landau levels are tilted by $J_+$ such that the velocity of the right (left) zeroth Landau level is $|v_z^\eta|+|v_0^\eta|$ $(|v_z^\eta|-|v_0^\eta|)$. (d) Magnon band structure of a twisted nanowire under an inhomogeneous external electric field, with $\frac{g\mu_B\mathcal{E}a^2}{ec^2} = \frac{g\mu_B\varepsilon a^2}{ec^2} = -0.0124\Phi_0$. Due to the chiral nature of the strain-induced pseudo-electric field, the effective electric field at the left Weyl cone vanishes while the effective electric field at the right Weyl cone is doubled. Therefore, the left tilted Weyl cone is not Landau-quantized but the right tilted Weyl cone exhibits tilted Landau levels.

Then, we discuss the effect of the $J_+$ term on the magnon equations of motion (Eqs. 4.25, 4.30). In the presence of a magnetic field $\boldsymbol{B}$, a Zeeman energy $U = -\boldsymbol{\mu} \cdot \boldsymbol{B}$ exists for both sublattices. It is thus diagonal in the sublattice basis $\phi_{\boldsymbol{k}} = (a_{\boldsymbol{k}}, b_{\boldsymbol{k}})^T$, in which the Bloch Hamiltonian $\mathcal{H}_{\boldsymbol{k}}$ is defined. For this reason, the total potential energy of magnons is $U' = U + m_{\boldsymbol{k}}$. When $m_{\boldsymbol{k}}$ has no spatial dependence, the gradient of the potential energy is unchanged by $m_{\boldsymbol{k}}$: $\nabla U' = \nabla U$ irrespective of the value of $J_+$. Therefore, the magnon equation of motion Eq. 4.25 is not affected when considering $J_+$. On the other hand, when a dynamic uniaxial strain is applied, an extra term $\delta\mathcal{H}^{\boldsymbol{b}}_{\boldsymbol{k}}$ must be added to the first-quantized Bloch Hamiltonian $\mathcal{H}_{\boldsymbol{k}}$. It is worth noting that the contribution from $J_+$ to $\delta\mathcal{H}^{\boldsymbol{b}}_{\boldsymbol{k}}$ has already been considered in Eq. 4.27. Therefore, the $J_+$ term is still a constant correction to the potential energy and will not affect the magnon equation of motion Eq. 4.30.

Lastly, we consider how the magnon quantum anomalies and the anomalous spin and heat currents are affected by the $J_+$ term. It is straightforward to see such a diagonal term has two effects. First, it shifts the magnon Weyl points in the energy dimension by an amount of $J_+(1-\cos Qa)S$. Second, it alters the velocities of the two zeroth Landau levels by $v_0^\eta = \eta J_+ Sa \sin Qa/\hbar$. To derive a generic theory of magnon transport in the presence of these two effects, we consider a Weyl ferromagnet nanowire aligned in the $z$ direction and subjected to a generalized electric field gradient $\mathscr{E}$, which can be generated by either an inhomogeneous electric field or a twist. Following the set-up in Section 4.3, the Weyl ferromagnet nanowire is attached to magnon reservoirs in a uniform magnetic field $\tilde{\boldsymbol{B}}_0 = \tilde{B}_0\hat{z}$ where $\tilde{B}_0 = B_0 + J_+(1-\cos Qa)S/g\mu_B$, so that the magnon population edges on both zeroth Landau levels remains tuned into the gap spanned by the first Landau levels. Then a generalized magnetic field gradient $\mathscr{B}$ generated by either an inhomogeneous magnetic field or a dynamic uniaxial strain is applied to the nanowire, under which magnons are pumped along Landau levels according to the generalized semiclassical equation of motion

$$q_z^{R/L}(t) = q_z^{R/L}(0) - s_{R/L} g\mu_B \int_0^t \mathscr{B} dt'/\hbar, \tag{D.1}$$

where the index $s_{R/L}$ indicates the nature of the magnetic field such that

$$(s_R, s_L) = \begin{cases} (+1,+1) & \text{for magnetic field} \\ (+1,-1) & \text{for pseudo-magnetic field} \end{cases}. \tag{D.2}$$

During the pumping process, the magnon population edge of the right/left zeroth Landau level is slightly shifted by $\delta_{R/L} \ll \tilde{B}_0$, so that the right/left

Weyl cone experiences a magnetic field $B_{R/L} = \tilde{B}_0 - \delta_{R/L}$. From the generalized semiclassical equation of motion Eq. D.1, we obtain the magnetic field variation for the right/left Weyl cone as

$$\delta_{R/L} = s_{R/L} v_{R/L} \int_0^t \mathscr{B} dt'. \tag{D.3}$$

By comparing to Eqs. 4.34, 4.35, the magnon concentration variation on the right/left zeroth Landau level reads

$$\begin{aligned} n_{R/L} &= \int_{g\mu_B B_{R/L}}^{g\mu_B \tilde{B}_0} g_{R/L}(\epsilon) n_B(\epsilon) d\epsilon \\ &\approx \frac{n_B(g\mu_B \tilde{B}_0)}{4\pi^2 l_{\mathscr{E}}^2} \frac{g\mu_B \delta_{R/L}}{\hbar |v_{R/L}|} - \frac{n_B'(g\mu_B \tilde{B}_0)}{2} \frac{(g\mu_B \delta_{R/L})^2}{4\pi^2 l_{\mathscr{E}}^2 \hbar |v_{R/L}|}, \end{aligned} \tag{D.4}$$

where we take the limit $g\mu_B \delta_{R/L} \ll k_B T$. The magnon density of states on the right/left zeroth Landau level is $g_{R/L}(\epsilon) = \frac{1}{2\pi l_{\mathscr{E}}^2} \frac{1}{2\pi\hbar |v_{R/L}|}$ with the generalized electric length $l_{\mathscr{E}} = (|\hbar c^2 / g\mu_B \mathscr{E}|)^{1/2}$. Due to the variation of magnon population, thermal energy will be injected into or depleted from the right/left zeroth Landau level. Explicitly, the thermal energy variation can be obtained by referring to Eqs. 4.39, 4.40 as

$$\begin{aligned} U_{R/L} &= \int_{g\mu_B B_{R/L}}^{g\mu_B \tilde{B}_0} \epsilon g_{R/L}(\epsilon) n_B(\epsilon) d\epsilon \\ &\approx \frac{1}{4\pi^2 l_{\mathscr{E}}^2 \hbar |v_{R/L}|} \Big\{ n_B(g\mu_B \tilde{B}_0) g\mu_B \tilde{B}_0 g\mu_B \delta_{R/L} \\ &\quad - \frac{1}{2} [n_B(g\mu_B \tilde{B}_0) + g\mu_B \tilde{B}_0 n_B'(g\mu_B \tilde{B}_0)] (g\mu_B \delta_{R/L})^2 \Big\}, \end{aligned} \tag{D.5}$$

where we again approximate $g\mu_B \delta_{R/L} \ll k_B T$. The magnon chiral anomaly and heat anomaly to the linear order in $g\mu_B \delta_{R/L}$ are given by

$$\frac{d\rho_5}{dt} = \chi_R \frac{dn_R}{dt} + \chi_L \frac{dn_L}{dt} \approx \frac{n_B(g\mu_B \tilde{B}_0)}{4\pi^2 l_{\mathscr{E}}^2 \hbar} g\mu_B \mathscr{B} (s_R \mathrm{sgn}(v_R) - s_L \mathrm{sgn}(v_L)), \tag{D.6}$$

$$\frac{d\rho_{\mathrm{heat}}}{dt} = \frac{dU_R}{dt} + \frac{dU_L}{dt} \approx \frac{n_B(g\mu_B \tilde{B}_0)}{4\pi^2 l_{\mathscr{E}}^2 \hbar} g^2 \mu_B^2 \tilde{B}_0 \mathscr{B} (s_R \mathrm{sgn}(v_R) + s_L \mathrm{sgn}(v_L)). \tag{D.7}$$

These anomalies only depend on the signs of velocities of the zeroth Landau levels. In the presence of an electric field, the inclusion of $J_+$ only changes the magnitude of $v_{R/L}$ without altering the directions of magnon propagation. Consequently, Eq. D.6 is reduced to Eq. 4.36 and Eq. D.7 is reduced to Eq. 4.62, and we still have the chiral anomaly for $(\boldsymbol{E}, \boldsymbol{B})$ and the heat anomaly for $(\boldsymbol{E}, \boldsymbol{b})$. In the presence of a pseudo-electric field, $J_+$ changes the velocity of the right (left) zeroth Landau level to $v_R = |v_z^\eta| + |v_0^\eta|$ ($v_L = |v_z^\eta| - |v_0^\eta|$). For a type-I Weyl ferromagnet, $|v_z^\eta| > |v_0^\eta|$, thus the advent of the $J_+$ term does not flip the sign of $v_L$. Consequently, Eq. D.6 is reduced to Eq. 4.49 and Eq. D.7 is reduced to Eq. 4.69, preserving the chiral anomaly for $(\boldsymbol{e}, \boldsymbol{b})$ and the heat anomaly for $(\boldsymbol{e}, \boldsymbol{B})$. On the other hand, for a type-II Weyl ferromagnet, $|v_z^\eta| < |v_0^\eta|$, and the sign of $v_L$ is flipped. In this case, $(\boldsymbol{e}, \boldsymbol{b})$ will have a heat anomaly but $(\boldsymbol{e}, \boldsymbol{B})$ will have a chiral anomaly. The anomalous spin and heat currents can be derived as

$$\begin{aligned} J_{\text{spin}} = -\hbar(n_R v_R + n_L v_L) \approx & -\frac{n_B(g\mu_B \tilde{B}_0)}{4\pi^2 l_{\mathscr{E}}^2} g\mu_B[\delta_R \text{sgn}(v_R) + \delta_L \text{sgn}(v_L)] \\ & + \frac{n_B'(g\mu_B \tilde{B}_0)}{8\pi^2 l_{\mathscr{E}}^2} g^2 \mu_B^2 [\delta_R^2 \text{sgn}(v_R) + \delta_L^2 \text{sgn}(v_L)], \end{aligned} \tag{D.8}$$

$$\begin{aligned} J_{\text{heat}} = v_R U_R + v_L U_L \approx & \frac{n_B(g\mu_B \tilde{B}_0)}{4\pi^2 l_{\mathscr{E}}^2 \hbar} g^2 \mu_B^2 \tilde{B}_0 [\delta_R \text{sgn}(v_R) + \delta_L \text{sgn}(v_L)] \\ & - \frac{n_B'(g\mu_B \tilde{B}_0)}{8\pi^2 l_{\mathscr{E}}^2 \hbar} g^3 \mu_B^3 \tilde{B}_0 [\delta_R^2 \text{sgn}(v_R) + \delta_L^2 \text{sgn}(v_L)] \\ & - \frac{n_B(g\mu_B \tilde{B}_0)}{8\pi^2 l_{\mathscr{E}}^2 \hbar} g^2 \mu_B^2 [\delta_R^2 \text{sgn}(v_R) + \delta_L^2 \text{sgn}(v_L)]. \end{aligned} \tag{D.9}$$

Unlike the anomalies (Eqs. D.6, D.7), the anomalous spin and heat currents depend on the magnitude of $v_{R/L}$ as well because $\delta_{R/L}$ is proportional to $v_{R/L}$ according to Eq. D.3. For $(\boldsymbol{E}, \boldsymbol{B})$, both zeroth Landau levels are steeper when the diagonal term is considered ($v_R = -v_L = |v_z^\eta| + |v_0^\eta|$). Therefore, the anomalous spin and heat currents are enhanced and the chiral electric effect becomes more pronounced. For $(\boldsymbol{E}, \boldsymbol{b})$, both the spin current and the heat current are zero because there are an equal number of right-moving magnons at the speed of $v_R = |v_z^\eta| + |v_0^\eta|$ and left-moving magnons at the speed of $v_L = -|v_z^\eta| - |v_0^\eta|$. For $(\boldsymbol{e}, \boldsymbol{b})$, importantly, the terms linear in $\delta_{R/L}$ in Eqs. D.8, D.9 are non-vanishing regardless of the sign of $v_{R/L}$, because $|\delta_R| \neq |\delta_L|$ when the $J_+$ term is considered. Therefore, the anomalous

spin/heat current $J^{\boldsymbol{e},\boldsymbol{b}}_{\text{spin/heat}} \sim b_5^2$ (Eqs. 4.57, 4.58) will be obscured by the dominant linear terms. Nevertheless, these less dominant chiral electric currents can in principle be extracted because they have unique pseudo-EM field dependence. For $(\boldsymbol{e}, \boldsymbol{B})$, the chiral torsional spin/heat current $J^{\boldsymbol{e},\boldsymbol{B}}_{\text{spin/heat}} \sim \delta_B$ (Eqs. 4.71, 4.72) is linear in the magnon population edge variation $\delta_B$, which is now replaced by $\frac{1}{2}[\delta_R \text{sgn}(v_R) + \delta_L \text{sgn}(v_L)]$ in Eqs. D.8, D.9. Such a variation, however, affects no qualitative changes to anomalous currents. To prove this, we reproduce Fig. 4.8 with the $J_+$ term considered. As illustrated in Fig. D.2, for a Weyl ferromagnet nanowire with a either rectangular or circular cross section, the bulk-surface separation for anomalous currents persists.

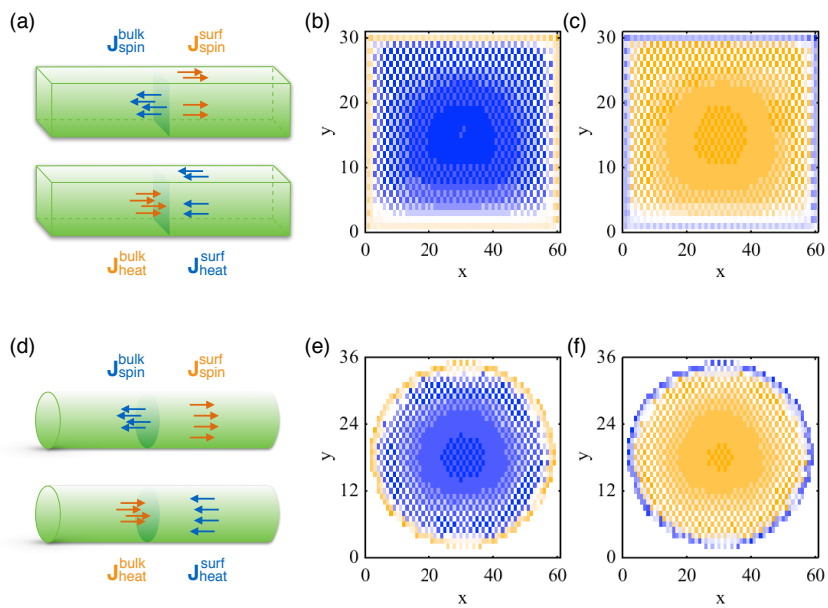


Figure D.2: Reproduction of bulk-surface separation for the twisted Weyl ferromagnet nanowire (Fig. 4.8) with a nonzero $J_+S = 4.08$. Though the Weyl cones are displaced and tilted, the bulk-surface separation of spin and heat currents is preserved for both the rectangular cross section (b, c) and the circular cross section (e, f). The total spin current on the rectangular (circular) cross section is $-0.0017DS$ ($-0.0016DS$) while the total heat current on the rectangular (circular) cross section is $0.046D^2S^2/\hbar$ ($0.0423D^2S^2/\hbar$).

# Appendix E

# Circular bend induced pseudo-electric field

In Chapter 4, we propose that the magnon chiral anomaly (Eq. 4.50) and the magnon heat anomaly (Eq. 4.63) may have experimentally measurable mechanical effects if an additional chiral pseudo-electric field $\boldsymbol{e}'_\eta = \eta(0, \varepsilon' z, 0)$ is applied. In this section, we will elaborate the implementation of such an additional pseudo-electric field.

We consider a simple circular bend lattice deformation as illustrated in Fig. E.1. As explained in Refs. [134, 176], to the lowest order of approximation, the displacement field of such a circular bend is $\boldsymbol{u} = \mathscr{U} xz\hat{z}$, resulting in nonzero strain tensor components $u_{13} = u_{31} = \frac{1}{2}\mathscr{U} z$ and $u_{33} = \mathscr{U} x$. The strain effect can then be incorporated by the following exchange integral substitutions

$$\begin{aligned}
J_2(\boldsymbol{\alpha}_1 \pm a\hat{z}) &\to J_2(1 \mp \tfrac{\sqrt{3}}{2}u_{31} - \tfrac{1}{2}u_{33}),\\
J_2(\boldsymbol{\alpha}_2 \pm a\hat{z}) &\to J_2(1 \pm \tfrac{\sqrt{3}}{2}u_{31} - \tfrac{1}{2}u_{33}),\\
J_2(\boldsymbol{\alpha}_3 \pm a\hat{z}) &\to J_2(1 - \tfrac{1}{2}u_{33}),\\
J_A &\to J_A(1 - u_{33}),\\
J_B &\to J_B(1 - u_{33}),
\end{aligned}$$

which result in an effective Hamiltonian

$$\begin{aligned}
\mathcal{H}_{\boldsymbol{k}^\eta_W+\boldsymbol{q}} + \delta\mathcal{H}_{\boldsymbol{k}^\eta_W+\boldsymbol{q}} \approx \mathcal{H}_{\boldsymbol{k}^\eta_W} &+ \hbar v_0^\eta\Big(q_z + \frac{e}{\hbar}a_z^\eta\Big)\sigma^0\\
&+ \sum_i \hbar v_i^\eta\Big(q_i + \frac{e}{\hbar}a_i^\eta\Big)\sigma^i - 3J_2 S u_{33}\sigma^0. \quad \text{(E.1)}
\end{aligned}$$

Here the strain-induced vector potential is

$$\boldsymbol{a}^\eta = -\eta\frac{\hbar}{ea}\left(\frac{2J_2\sin Qa}{J_1 + 2J_2\cos Qa}u_{31}, 0, \frac{1-\cos Qa}{\sin Qa}u_{33}\right), \quad \text{(E.2)}$$

which is incorporated by a minimal substitution in the same way as $\boldsymbol{a}^\eta_S$ and $\boldsymbol{a}^\eta_D$. Again, a non-chiral on-site term $-3J_2 S u_{33}\sigma^0$ appears, but such a

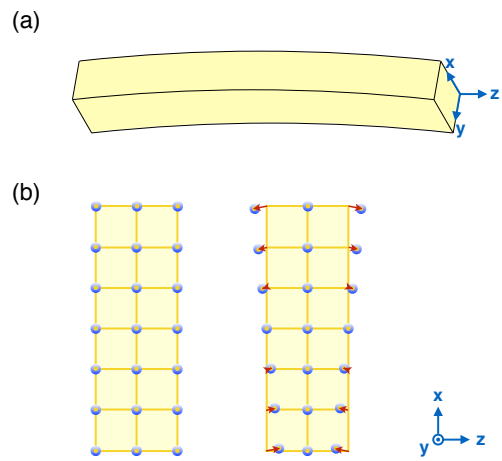


Figure E.1: Schematic plot for the Weyl ferromagnet nanowire. (a) Nanowire under a circular bend deformation. (b) Lattice site positions without deformation (left) and with a circular bend (right).

term is negligible when $\hbar|v_z^\eta|/a \gg J_2 S$, and it can be otherwise cancelled by an additional magnetic field $\boldsymbol{B}' = -\frac{3J_2 S u_{33}}{\mu^2}\boldsymbol{\mu}$. Therefore, its effect on magnon mechanics can be safely neglected. On the other hand, by referring to Eq. 4.30, the chiral gauge vector potential $\boldsymbol{a}^\eta$ gives rise to a magnon Lorentz force

$$\hbar\frac{d\boldsymbol{k}}{dt} = -e\boldsymbol{v} \times [\nabla \times \boldsymbol{a}^\eta]. \tag{E.3}$$

Comparing to the magnon Lorentz force (Eq. 4.77) due to an additional electric field $\boldsymbol{E}' = (0, \mathcal{E}' z, 0)$, we may interpret $\boldsymbol{a}^\eta$ as the vector potential of the additional chiral pseudo-electric field $\boldsymbol{e}'_\eta = \eta(0, \varepsilon' z, 0)$, which only differs from $\boldsymbol{E}'$ by a chiral charge $\eta$. The gradient of this additional pseudo-electric field can be determined by $\nabla \times \boldsymbol{a}^\eta = \frac{1}{ec^2}\nabla \times (\boldsymbol{e}'_\eta \times \boldsymbol{\mu}) = -\eta\frac{g\mu_B \varepsilon'}{ec^2}\hat{y}$. Explicitly, the field gradient reads

$$\varepsilon' = -\eta\frac{ec^2}{g\mu_B}\hat{y} \cdot (\nabla \times \boldsymbol{a}^\eta) = \frac{\hbar c^2}{g\mu_B a}\left[\frac{J_2 \sin Qa}{J_1 + 2J_2 \cos Qa} - \frac{1 - \cos Qa}{\sin Qa}\right]\mathscr{U}. \tag{E.4}$$

As discussed in Section 4.5.2 (Section 4.5.3), when $\varepsilon'$ is sufficiently small, i.e., $\varepsilon' \ll \varepsilon$ ($\varepsilon' \ll \mathcal{E}$), the bend-induced pseudo-electric field $\boldsymbol{e}'_\eta$ generates a transverse force that may be measured by AFM, while the magnon Landau levels are not strongly affected. On the other hand, if $\varepsilon'$ is sufficiently large, the bend-induced pseudo-electric field $\boldsymbol{e}'_\eta$ also results in Landau quantiza-

tion. In contrast to the Landau quantization due to a twist, the Landau quantization due to a bend takes place in the transverse direction.

# Appendix F

# The tetrahedron method

In Section 2.4, we have analytically calculated DOS and longitudinal electric conductivity $\sigma_{yy}$ of WSM with semiclassical methods. We then applied same technique to calculate DOS and longitudinal thermal conductivity $\kappa_{xx}$ of WSC in Section 3.4. In order to obtain high quality numerical data shown in Fig. 2.5 and Fig. 3.7, we have numerically calculated $\sigma_{yy}$ and $\kappa_{xx}$ using the tetrahedron method, which is detailed as below.

We consider a multi-band lattice model with good quantum numbers $k_\lambda$ and $k_\nu$. The energy bands satisfy $\epsilon_n(k_\lambda, k_\nu) = \epsilon_n(-k_\lambda, k_\nu) = \epsilon_n(k_\lambda, -k_\nu) = \epsilon_n(-k_\lambda, -k_\nu)$. Therefore, the full electronic structure of this lattice model can be obtained by diagonalizing in the first quadrant of Brillouin zone. Numerically, the diagonalization only happens at discrete $\boldsymbol{k}$ points, which constitute the grid shown in Fig. F.1. We further cut each rectangular plaquette into a pair of right triangular plaquettes, colored grey and white respectively, as illustrated in Fig. F.1. For a generic triangular plaquette $S_{\boldsymbol{k}}$, the momentum at the right angle vertex is denoted as $[k_\lambda(S_{\boldsymbol{k}}), k_\nu(S_{\boldsymbol{k}})]$. We then discretize the $n$-th energy band on $S_{\boldsymbol{k}}$. When $S_{\boldsymbol{k}}$ is sufficiently small, the $n$-th energy band can be approximated as a combination of many triangular pieces in the energy-momentum space.

For the triangular piece defined on $S_{\boldsymbol{k}}$, the energies of vertices are denoted as $\epsilon_1^n(S_{\boldsymbol{k}})$, $\epsilon_2^n(S_{\boldsymbol{k}})$, and $\epsilon_3^n(S_{\boldsymbol{k}})$. Particularly, for the grey triangular plaquettes we have $\epsilon_1^n(S_{\boldsymbol{k}}) = \epsilon_n[k_\lambda(S_{\boldsymbol{k}}), k_\nu(S_{\boldsymbol{k}}) + \frac{2\pi}{L_\nu}]$, $\epsilon_2^n(S_{\boldsymbol{k}}) = \epsilon_n[k_\lambda(S_{\boldsymbol{k}}), k_\nu(S_{\boldsymbol{k}})]$, and $\epsilon_3^n(S_{\boldsymbol{k}}) = \epsilon_n[k_\lambda(S_{\boldsymbol{k}}) + \frac{2\pi}{L_\lambda}, k_\nu(S_{\boldsymbol{k}})]$, while for the white triangular plaquettes we have $\epsilon_1^n(S_{\boldsymbol{k}}) = \epsilon_n[k_\lambda(S_{\boldsymbol{k}}), k_\nu(S_{\boldsymbol{k}}) - \frac{2\pi}{L_\nu}]$, $\epsilon_2^n(S_{\boldsymbol{k}}) = \epsilon_n[k_\lambda(S_{\boldsymbol{k}}), k_\nu(S_{\boldsymbol{k}})]$, and $\epsilon_3^n(S_{\boldsymbol{k}}) = \epsilon_n[k_\lambda(S_{\boldsymbol{k}}) - \frac{2\pi}{L_\lambda}, k_\nu(S_{\boldsymbol{k}})]$ with $L_\lambda$ and $L_\nu$ measuring the dimension of the lattice model. Thus, the dispersion of a triangular piece of energy band can be written down as

$$\epsilon_{S_{\boldsymbol{k}}}^n(k_\lambda, k_\nu) = \epsilon_2^n(S_{\boldsymbol{k}}) \pm \frac{\epsilon_3^n(S_{\boldsymbol{k}}) - \epsilon_2^n(S_{\boldsymbol{k}})}{2\pi/L_\lambda}(k_\lambda - k_\lambda(S_{\boldsymbol{k}})) \pm \frac{\epsilon_1^n(S_{\boldsymbol{k}}) - \epsilon_2^n(S_{\boldsymbol{k}})}{2\pi/L_\nu}(k_\nu - k_\nu(S_{\boldsymbol{k}})), \quad \text{(F.1)}$$

where the plus (minus) sign is for the grey (white) triangular plaquettes. And the corresponding DOS at energy $\mu$ of the lattice model is

$$g(\mu) = \sum_n \sum_{k_\lambda, k_\nu} \delta(\mu - \epsilon_n(k_\lambda, k_\nu))$$
$$\approx \frac{L_\lambda L_\nu}{\pi^2} \sum_n \sum_{S_{\boldsymbol{k}}} \oiint_{S_{\boldsymbol{k}}} dk_\lambda dk_\nu \delta(\mu - \epsilon_n(k_\lambda, k_\nu)) = 4 \sum_n \sum_{S_{\boldsymbol{k}}} g^n_{S_{\boldsymbol{k}}}(\mu), \quad \text{(F.2)}$$

where

$$g^n_{S_{\boldsymbol{k}}}(\mu) = \frac{[\mu - \epsilon^n_1(S_{\boldsymbol{k}})]\theta[\mu - \epsilon^n_1(S_{\boldsymbol{k}})]}{[(\epsilon^n_2(S_{\boldsymbol{k}})) - \epsilon^n_1(S_{\boldsymbol{k}})][(\epsilon^n_3(S_{\boldsymbol{k}})) - \epsilon^n_1(S_{\boldsymbol{k}})]}$$
$$+ \frac{[\mu - \epsilon^n_2(S_{\boldsymbol{k}})]\theta[\mu - \epsilon^n_2(S_{\boldsymbol{k}})]}{[(\epsilon^n_1(S_{\boldsymbol{k}})) - \epsilon^n_2(S_{\boldsymbol{k}})][(\epsilon^n_3(S_{\boldsymbol{k}})) - \epsilon^n_2(S_{\boldsymbol{k}})]}$$
$$+ \frac{[\mu - \epsilon^n_3(S_{\boldsymbol{k}})]\theta[\mu - \epsilon^n_3(S_{\boldsymbol{k}})]}{[(\epsilon^n_1(S_{\boldsymbol{k}})) - \epsilon^n_3(S_{\boldsymbol{k}})][(\epsilon^n_2(S_{\boldsymbol{k}})) - \epsilon^n_3(S_{\boldsymbol{k}})]}, \quad \text{(F.3)}$$

where $\theta(\epsilon)$ is the Heaviside step function. According to the Boltzmann equation approach, at low temperature, the electric conductivity reads

$$\sigma_{\lambda\lambda} = e^2 \sum_n \sum_{k_\lambda, k_\nu} \tau_n(\epsilon_n(k_\lambda, k_\nu)) v^n_\lambda(k_\lambda, k_\nu) v^n_\lambda(k_\lambda, k_\nu) \left( - \frac{\partial f(\epsilon)}{\partial \epsilon} \right)_{\epsilon_n(k_\lambda, k_\nu)}$$
$$\approx e^2 \frac{L_\lambda L_\nu}{\pi^2} \sum_n \sum_{S_{\boldsymbol{k}}} \oiint_{S_{\boldsymbol{k}}} dk_\lambda dk_\nu \tau_n(\epsilon^n_{S_{\boldsymbol{k}}}(k_\lambda k_\nu)) \left( \frac{1}{\hbar} \frac{\partial \epsilon^n_{S_{\boldsymbol{k}}}}{\partial k_\lambda} \right)^2 \delta(\mu - \epsilon^n_{S_{\boldsymbol{k}}}(k_\lambda, k_\nu))$$
$$= \frac{e^2}{\hbar^2} \frac{L^2_\lambda}{\pi^2} \sum_n \sum_{S_{\boldsymbol{k}}} \tau_n(\mu)(\epsilon^n_3(S_{\boldsymbol{k}}) - \epsilon^n_2(S_{\boldsymbol{k}}))^2 g_{S_{\boldsymbol{k}}}(\mu), \quad \text{(F.4)}$$

where we have used group velocity $v^n_\lambda(k_\lambda, k_\nu) = \frac{1}{\hbar} \frac{\partial \epsilon_n(k_\lambda, k_\nu)}{\partial k_\lambda}$ and $f(\epsilon) = \frac{1}{e^{(\epsilon - \mu)/k_B T} + 1}$ is the Fermi function with chemical potential $\mu$ and temperature $T$. On the other hand, Boltzmann equation gives thermal conductivity as

$$\kappa_{\lambda\lambda} = \frac{1}{T} \sum_n \sum_{k_\lambda, k_\nu} (\epsilon_n(k_\lambda, k_\nu) - \mu)^2 \tau_n(\epsilon_n(k_\lambda, k_\nu))$$
$$\times v^n_\lambda(k_\lambda, k_\nu) v^n_\lambda(k_\lambda, k_\nu) \left( - \frac{\partial f(\epsilon)}{\partial \epsilon} \right)_{\epsilon_n(k_\lambda, k_\nu)}, \quad \text{(F.5)}$$

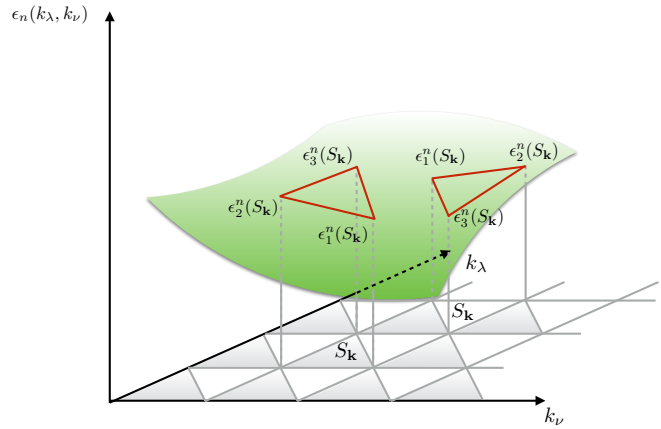


Figure F.1: Discretization of energy band in the tetrahedron method. The Brillouin zone spanned by $(k_\lambda, k_\nu)$ is first discretized into rectangular grid. Then each rectangular plaquette is cut into a pair of right triangular plaquettes colored grey and white. The $n$-th energy band $\epsilon_n(k_\lambda, k_\nu)$ is then discretized on the both types of triangular plaquettes. On each triangular plaquette $S_{\boldsymbol{k}}$, the discretized piece of energy band can be approximated as having zero curvature and each piece has vertex energies $\epsilon_1^n(S_{\boldsymbol{k}})$, $\epsilon_2^n(S_{\boldsymbol{k}})$, and $\epsilon_3^n(S_{\boldsymbol{k}})$.

which, by using the Sommerfeld expansion, can be further simplified as

$$\kappa_{\lambda\lambda} = \frac{\pi^2 k_B^2 T}{3} \sum_n \sum_{k_\lambda, k_\nu} \tau_n(\epsilon_n(k_\lambda, k_\nu)) v_\lambda^n(k_\lambda, k_\nu) v_\lambda^n(k_\lambda, k_\nu) \left( -\frac{\partial f(\epsilon)}{\partial \epsilon} \right)_{\epsilon_n(k_\lambda, k_\nu)}, \tag{F.6}$$

which reflects the Wiedemann-Franz law. According to Eq. F.4, we can directly write down the thermal conductivity as

$$\kappa_{\lambda\lambda} \approx \frac{\pi^2 k_B^2 T}{3} \frac{1}{\hbar^2} \frac{L_\lambda^2}{\pi^2} \sum_n \sum_{S_{\boldsymbol{k}}} \tau_n(\mu) (\epsilon_3^n(S_{\boldsymbol{k}}) - \epsilon_2^n(S_{\boldsymbol{k}}))^2 g_{S_{\boldsymbol{k}}}(\mu). \tag{F.7}$$

We now consider the longitudinal electric conductivity $\sigma_{yy}$ in Weyl semimet-

als. According to Eq. 2.25, Eq. F.4 can be rewritten as

$$\begin{aligned}\sigma_{yy}(b) &= \frac{1}{\frac{2\pi}{\hbar} n_{\text{imp}} C_{\text{imp}} g(\mu)} \frac{e^2}{\hbar^2} \frac{L_y^2}{\pi^2} \sum_n \sum_{S_{\boldsymbol{k}}} (\epsilon_3^n(S_{\boldsymbol{k}}) - \epsilon_2^n(S_{\boldsymbol{k}}))^2 g_{S_{\boldsymbol{k}}}(\mu) \\ &= \frac{e^2 (v_y^\eta)^2}{\frac{2\pi}{\hbar} n_{\text{imp}} C_{\text{imp}}} \frac{1}{\hbar^2 (v_y^\eta)^2} \frac{L_y^2}{4\pi^2} \frac{\sum_n \sum_{S_{\boldsymbol{k}}} (\epsilon_3^n(S_{\boldsymbol{k}}) - \epsilon_2^n(S_{\boldsymbol{k}}))^2 g_{S_{\boldsymbol{k}}}(\mu)}{\sum_n \sum_{S_{\boldsymbol{k}}} g_{S_{\boldsymbol{k}}}(\mu)} \\ &= \sigma_{yy}(0) \frac{\sum_n \sum_{S_{\boldsymbol{k}}} (\epsilon_3^n(S_{\boldsymbol{k}}) - \epsilon_2^n(S_{\boldsymbol{k}}))^2 g_{S_{\boldsymbol{k}}}(\mu)}{\left(\frac{2\pi\hbar v_y^\eta}{L_y}\right)^2 \sum_n \sum_{S_{\boldsymbol{k}}} g_{S_{\boldsymbol{k}}}(\mu)}, \end{aligned} \tag{F.8}$$

where $\epsilon_3^n(S_{\boldsymbol{k}})$ and $\epsilon_2^n(S_{\boldsymbol{k}})$ can be extracted by numerically diagonalizing Eq. 2.9. And $\sigma_{yy}(b)/\sigma_{yy}(0)$ is plotted in Fig. 2.5 for $\mu = 10$meV and in Fig. 2.6 for $\mu = 28$meV, both of which exhibit Shubnikov-de Haas oscillation.

For the thermal conductivity of Weyl superconductor, according to Eq. 3.80, we rewrite Eq. F.7 as

$$\begin{aligned}\kappa_{xx}(b) &= \frac{\pi^2 k_B^2 T}{3} \frac{1}{\hbar^2} \frac{L_x^2}{\pi^2} \sum_n \sum_{S_{\boldsymbol{k}}} \tau_n(0) (\epsilon_3^n(S_{\boldsymbol{k}}) - \epsilon_2^n(S_{\boldsymbol{k}}))^2 g_{S_{\boldsymbol{k}}}(0) \\ &= \frac{1}{\frac{2\pi}{\hbar} n_{\text{imp}} C_{\text{imp}}} \frac{\pi^2 k_B^2 T}{3} \frac{1}{\hbar^2} \frac{L_x^2}{4\pi^2} \frac{\sum_n \sum_{S_{\boldsymbol{k}}} (\epsilon_3^n(S_{\boldsymbol{k}}) - \epsilon_2^n(S_{\boldsymbol{k}}))^2 g_{S_{\boldsymbol{k}}}(0)}{\sum_n \sum_{S_{\boldsymbol{k}}} g_{S_{\boldsymbol{k}}}(0)} \\ &= \kappa_{xx}(0) \frac{\sum_n \sum_{S_{\boldsymbol{k}}} (\epsilon_3^n(S_{\boldsymbol{k}}) - \epsilon_2^n(S_{\boldsymbol{k}}))^2 g_{S_{\boldsymbol{k}}}(0)}{\left(\frac{2\pi\hbar v_x}{L_x}\right)^2 \sum_n \sum_{S_{\boldsymbol{k}}} g_{S_{\boldsymbol{k}}}(0)}. \end{aligned} \tag{F.9}$$

Again, $\epsilon_3^n(S_{\boldsymbol{k}})$ and $\epsilon_2^n(S_{\boldsymbol{k}})$ can be extracted by numerically diagonalizing Eq. 3.13. And $\kappa_{xx}(b)/\kappa_{xx}(0)$ is plotted in Fig. 3.7, exhibiting quantum oscillation.